

POLITECNICO DI TORINO

Master of Science in Nanotechnologies for ICTs

Master Thesis

Design and optimization of nanostructured flexible sensors



Supervisor

Prof. Marzia Quaglio

Co-supervisor

Prof. Giulia Massaglia

Candidate

Cristina Sbaraglia

A.Y. 2021/2022

Graduation session June 2022

To my parents

Abstract

Nowadays, there is a growing interest for flexible strain and pressure sensors due to the increasing demand in several applications fields like industrial, automotive, robotics, biomedical and many others. Conventional sensors have excellent sensitivities but show severe limitations due to their mechanical properties and poor flexibility, which can be overcome by using nanostructured materials. Nanostructured materials show unique and excellent properties with respect to their macroscopic counterparts. Their most important property is the high surface area to volume ratio, which offers interesting possibilities in several applications, as the improved sensitivity, electrical and mechanical performances in flexible sensors. Inside the nanoscale world, nanofibers by electrospinning are an emerging class in the sensing field, since they can be obtained by a simple, low cost and versatile process if compared to other types of nanostructures manufacturing methods. Especially, polymer-based nanofibers and composite nanomaterials, mostly based on carbon nanotubes (CNTs), have been largely employed as functional materials inside flexible piezoelectric and piezoresistive strain and pressure sensors, respectively. Poly(vinylidene fluoride) (PVDF) is, among all polymers, the most used one because of its piezoelectric properties that can be enhanced by nanoconfinement during the electrospinning nanofiber deposition. On the other hand, polymer/CNTs composite nanofibers exhibit a significant change in their resistivity with strain and therefore, provides a great potential to be used in various sensing applications.

The aim of this thesis is the fabrication and characterization of two types of electrospun nanofibers mats: a piezoresistive one, made of CNTs/polymer nanocomposite, and a piezoelectric one, made of PVDF. Moreover, this thesis investigates the role of electrospinning process parameters on the final properties of functional NFs. Along with conventional parameters, rotating drum collectors with different diameters are analyzed to determine their effect on the final morphology, electrical performance and piezoelectric or piezoresistive response of the resulting functional nanofibers. Finally, it is also introduced the possibility of combining both piezoelectric and piezoresistive mechanisms in one single flexible sensing platform in order to allow the detection of static and highly dynamic signals.

Contents

List of Figures	v
List of Tables	x
1 Introduction	1
2 The fundamental theoretical aspects	7
2.1 Transduction mechanisms of mechanical signals in electrical one	7
2.1.1 Triboelectric effect	8
2.1.2 Capacitive effect	8
2.1.3 Piezoresistive effect	9
2.1.4 Piezoelectric effect	10
2.1.5 Combination of piezoelectric and piezoresistive effect	11
2.2 Nanocomposite materials for flexible pressure sensors	11
2.2.1 Dispersion of CNTs in polymer matrices	13
2.2.2 Percolation model	14
2.2.3 Piezoresistive effect in CNTs/polymer composites	16
2.2.4 PEO and CARBON NANOTUBES arranged as polymer-based composite	18
2.3 Piezoelectric materials for flexible pressure sensors	20
2.3.1 PVDF	25
3 The electrospinning process	27
3.1 Electrospinning	27
3.2 Hystory of electrospinning	27
3.3 The electrospinning process	28
3.4 Effects of various parameters on electrospinning	31
3.4.1 Solution parameters	31
3.4.2 Processing parameters	34
3.4.3 Ambient parameters	37
3.5 Synthesis of polymer/CNTs nanocomposite fibers by electrospinning	37
3.6 Influence of electrospinning parameters on β -phase of PVDF	38
3.6.1 Influence of electrospinning parameters on PVDF piezoelectric behavior	39

4 Piezoresistive analysis	46
4.1 Materials and configurations used	46
4.2 The percolation curve	49
4.2.1 Choosing electrospinning parameters of deposition	50
4.2.2 Final implementation of the percolation curve	56
4.3 Piezoresistive analysis of composite nanofibers	59
4.3.1 Sensitivity curves	65
5 Piezoelectric effect	69
5.1 Materials and configurations used	69
5.2 Choosing electrospinning parameters for PVDF solution deposition	70
5.3 FT-IR characterization	71
5.4 Piezoelectric characterization	74
5.5 Repeatability	76
6 Fututure developments	78
7 Conclusions	82
A Instruments of analysis	84
A.1 Optical microscope	84
A.2 FESEM	85
A.3 FT-IR	86
B Deposition of PEO/MWCNT solutions at different CNTs weight percentages.	89
C Electrospinning parameters for PVDF deposition in literature	95
Bibliography	100

List of Figures

1.1	Schematic representation of the use of a sensor in a measurement chain [2].	1
1.2	Examples of applications of strain and pressure sensor: (a) wearables, (b)robotics, (c) industrial application [4].	3
1.3	The increasing number of published works in the field of electrospinning. The red part is related to the electrospinning of semiconductors. Reprinted from [21], Copyright (2018), with permission from Elsevier.	5
2.1	Schematic illustration of electromechanical sensors: (a) triboelectric, (b) piezoelectric, (c) capacitive and (d) piezoresistive [23].	7
2.2	Schematic representation of the piezoelectric effect in three cases: longitudinal deformation in the direct (a) and indirect (b) case, (c) shear deformation [37].	10
2.3	Schematic representation of nanocomposite materials.	12
2.4	Influence of filler type on composite material behavior: (a) Resistivity behavior of composite as a function of filler concentration for two types of filler (carbon nanotubes and carbon black), (b)critical filler gradient as a function of aspect ratio for CNTs and CB [4].	13
2.5	Process flow for the preparation of the MWCNT/PSS/PEO solution to be electrospun [46].	14
2.6	Change of the structure of the composite material increasing the filler concentration [52].	15
2.7	Typical percolation curve related to polymer nanocomposite structure with the increase of nanoparticle concentration, highlighting the critical path at the onset of percolation, denoted by red line. Reprinted by permission of Springer Nature Customer Service Centre GmbH [53], Copyright (2008).	15
2.8	Collection of values t and corresponding critical threshold concentration x_c for various disordered conductor-insulator composites. The dashed line highlights the universal value of t . Reprinted with permission from [55], Copyright (2005) by the America Physical Society.	17
2.9	Schematic representation of the tunneling between neighboring CNTs [57].	18
2.10	PEO polymeric chain (b) from synthesis of Ethylene oxide(a).	19
2.11	Crystal structure of different allotropes of carbon. Three-dimensional diamond and graphite (3D), two-dimensional graphene (2D), one dimensional nanotube (1D) and zero dimensional buckyballs (0D). Reprinted from [62], Copyright(2007), with permission from Elsevier.	19

2.12	(a) SWCNT and (b) MWCNT.	20
2.13	Conductive pathways increasing from below to above percolation threshold in electrospun NFs. Reprinted with permission from [70], Copyright (2021) American Chemical Society.	21
2.14	Perovskite general structure ABX ₃ [65].	21
2.15	Crystalline structure of ceramic PZT below and above Curie temperature [66].	22
2.16	Diagram of the division of piezoelectric materials [68].	23
2.17	Electric dipoles in Weiss domains: (1) unpoled ferroelectric ceramic, (2) during poling, (3) after poling (piezoelectric ceramic) [69].	23
2.18	Representation of the theoretical hysteresis loop [68].	24
2.19	Representation of the α , β , γ -phases of the PVDF polymer chain. Reprinted from [77], Copyright (2014), with permission from Elsevier.	25
2.20	β -PVDF induced by stretching pr high poling voltage [74].	26
3.1	Schematic representation of the planar vertical (a) and horizontal (b) electrospinning set up. Reprinted from [87], Copyright (2010), with permission from Elsevier.	29
3.2	Behavior of the jet during the electrospinning process [89].	30
3.3	Taylor cone formation with increasing applied voltages [90].	30
3.4	Instabilities of the jet with progressive reduction of diameter [21]. Reprinted from [108], Copyright (2008), with permission from Elsevier.	31
3.5	SEM image showing the morphology of fibers increasing the solution concentration. Electric field is 0.7 kV/cm. Reprinted from [93], Copyright (199), with permission from Elsevier.	32
3.6	SEM images and fiber size distribution of PVDF nanofibers with increasing tip to collector distance. Reprinted from [106], Copyright (2021), with permission from Elsevier.	35
3.7	Different types of collectors for electrospinning: (A) static plate, (B) parallel electrodes, (C) rotating disk, (D) rotating drum, (E) grid [98].	36
3.8	TEM image of CNTs oriented along the polymer composite nanofiber direction. Reprinted from [103], Copyright (2005), with permission from Elsevier.	37
3.9	Schematic representation of the flow of an electrospun solution in polar coordinates. Reprinted with permission from [72], Copyright (2003) American Chemical Society	38
3.10	Influence of the applied voltage on the β phase fraction of electrospun PVDF. (a) work of Shao, Hao, et al. Republished with permission of Royal Society of Chemistry, from[104]; permission conveyed through Copyright Clearance Center. (b) work of Singh. Reprinted from [105], Copyright (2021), with permission from Elsevier.	39
3.11	Influence of the spinning distance on the β phase fraction of electrospun PVDF. (a) work of Shao, Hao, et al. Republished with permission of Royal Society of Chemistry, from[104]; permission conveyed through Copyright Clearance Center. (b) work of Singh. Reprinted from [105], Copyright (2021), with permission from Elsevier.	40

3.12	Influence of flow rate on the β phase fraction of electrospun PVDF. (a)work of Gade, Harshal, et al. Reprinted from [106], Copyright (2021), with permission from Elsevier., (b) work of Singh. Reprinted from [105], Copyright (2021), with permission from Elsevier.	41
3.13	Influence of the PVDF concentration inside the polymeric solution on the β phase fraction of electrospun PVDF. (a) work of Shao, Hao, et al.Republished with permission of Royal Society of Chemistry, from[104]; permission conveyed through Copyright Clearance Center. (b) work of Gade, Harshal, et al. Reprinted from [106], Copyright (2021), with permission from Elsevier.	42
3.14	Influence of the drum rotation speed on the β phase fraction of electrospun PVDF. Reprinted from [105], Copyright (2021), with permission from Elsevier.	43
3.15	(a) FTIR plot and (b) β -phase fraction for PVDF nanofibers samples prepared with three different electrospinning time. Reprinted from [105], Copyright (2021), with permission from Elsevier.	44
3.16	Voltage and current outputs of PVDF nanofiber mats with different mat thicknesses obtained with different electrospinning time. Republished with permission of Royal Society of Chemistry, from[104]; permission conveyed through Copyright Clearance Center.	44
4.1	Branson ultrasonicator used to better disperse MWCNTs inside the solution.	47
4.2	Electrospinning system NANON 01A.	47
4.3	Electrospinning set up for the solution deposition on an insulating wire.	48
4.4	Nanofiber spider web formation between the wire and the aluminum tool.	49
4.5	MWCNTs/PEO nanocomposite deposition on the hollow wire. (a) Electrospinning setup used. (b) Photograph of an example of nanofiber deposition.	49
4.6	Experimental values of the electrical conductivity of composite nanofibers for different concentration of MWCNTs as reported by Massaglia et al. Three sets of samples are represented: PEO with molecular weight of 600kDa (green curve at 18 kV) and 1000KDa (red at 23kV and blue at 18kV curves); the corresponding percolation thresholds are reported and some FESEM images are proposed [46].	50
4.7	Set-up for the sample's electrical characterization.	52
4.8	Current values obtained setting a bias voltage equal to 1V for each sample.	52
4.9	I/V characteristic for each sample.	53
4.10	Two optical microscope pictures of the sample "BW1" for the diameter evaluation.	54
4.11	MATLAB plots of the electrical conductivity as a function of $R/\Delta l$ for each sample.	55
4.12	MATLAB plots of the electrical conductivity as a function of the radius of the cross section for each sample.	55
4.13	Fitting of experimental values of electrical conductivity of composite nanofibers for different MWCNTs concentrations.	57
4.14	FESEM pictures of nanofibers at different MWCNTs concentrations: (a) 0 wt%, (b) 1.5 wt%, (c) 2.2 wt%, (d) 2.5 wt%, (e) 3.5 wt%, (f) 5 wt%.	58
4.15	FESEM pictures obtained using 1.5 wt% MWCNTs using a working voltage of (a) 18 kV and 23 kV [4].	59

4.16	Preliminary piezoresistive analysis on samples containing MWCN with weight percentage of 6 wt%. (c) and (d) are the set-up of measurement while (a) and (b) are the corresponding characteristics obtained.	60
4.17	Electrical characterization of sample containing MWCNT with weight percentage of 6 wt%. (a) Current as a function of time (bias voltage equal to 1V), (b) I/V characteristic.	61
4.18	Piezoresistive characterization set-up.	62
4.19	Piezoresistive characterization set-up for a wire (left) and for an hollow wire (right).	62
4.20	Schematic representation of the hollow wire used as deposition substrate with the starting shape (left) and after pressure application (right).	63
4.21	I/V characteristic of sample containing MWCNT with weight percentage of 3.5 wt%.	63
4.22	Piezoresistive analysis on nanofiber mat deposited on a hollow wire from a solution containing MWCNT with weight percentage of 6 wt%.	64
4.23	Piezoresistive analysis on nanofiber mat deposited on a hollow wire from a solution containing MWCNT with weight percentage of 3.5 wt%.	65
4.24	Electrical resistance variations as a function of the applied pressure for the hollow wire at 3 wt% of MWCNT.	66
4.25	Electrical resistance variations as a function of the applied pressure for the hollow wire at 6 wt% of MWCNT.	66
4.26	Electrical resistance variations as a function of the applied pressure for the wire at 3.5 wt% of MWCNT.	67
5.1	Reference substrate and type of collectors used during the PVDF nanofibers deposition: (a) planar and (b) drum collector.	70
5.2	IR spectra of samples in planar (1a, 1b, 1c) and drum (2a) deposition configurations. The three different crystalline phases of PVDF nanofiber mat are highlighted in red for the β -phase, in green for the γ -phase and in black for the non-polar α -phase.	72
5.3	Comparison between IR spectra of samples 1a and 2a. The three different crystalline phases of PVDF nanofiber mat are highlighted in red for the β -phase, in green for the γ -phase and in black for the non-polar α -phase.	73
5.4	(Left)Kapton-copper sheet used as deposition substrate. (Right)Example of PVDF nanofiber deposition on a Kapton-copper sheet.	74
5.5	Ferroelectric hysteresis loop and the displacement loop of sample 1a.	75
5.6	Comparison between IR spectra of samples 1a and all the six replicas. The three different crystalline phases of PVDF nanofiber mat are highlighted in red for the β -phase, in green for the γ -phase and in black for the non-polar α -phase.	76
5.7	Comparison between IR spectra of samples realized with drum collector for 2h and 3h of deposition. The three different crystalline phases of PVDF nanofiber mat are highlighted in red for the β -phase, in green for the γ -phase and in black for the non-polar α -phase.	77
6.1	Schematic representation of the “layer-by-layer” deposition.	78

6.2	Schematic representation of the electrical characterization set-up.	79
6.3	Current values obtained setting a bias voltage equal to 1V for the “External part” (red curve) and the “Internal part” (blue curve).	80
6.4	I/V curves for the “External part” (red curve) and the “Internal part” (blue curve).	80
A.1	Scheme of an optical microscope operating in reflection (right) and transmission (left) [110].	84
A.2	a) FESEM of Polytechnic of Turin laboratory, (b) FESEM sample holder, (c) sample preparation before the FESEM analysis.	86
A.3	Schematic representation of the Michelson Interferometer. Reprinted from [111], Copyright (1993), with permission from Elsevier.	87
B.1	Schematic representation of the hollow wire division in segments for multi-meter data acquisition.	89
B.2	I/V curves of samples at different MWCNT weight percentages for different sample locations: (a) sample with 0 wt%, (b), (c), (d) samples with 1.5 wt%, (e) sample with 2.2 wt%, (f) sample with 2.5 wt%, (g) sample with 3.5 wt% and (h) sample with 5 wt%.	90
B.3	Set up for a more accurate electrical characterization of our samples. . . .	91
B.4	(Left) Set up used for nanofiber mat thickness. (Right) Schematic representation of a sample cross section.	92
B.5	(Left) FESEM image of sample $Dep_{1.5/3}$. (Right) FESEM image of sample $Dep_{3.5}$	93

List of Tables

3.1	Conversion from rotation speed to tangent velocities.	43
4.1	Electrospinning parameters used for the realization of four different samples at 3.5 wt% of MWCNT.	51
4.2	Electrical resistance values for each sample and for each Δl	53
4.3	Values of diameters obtained thanks to the use of an optical microscope.	54
4.4	Electrical conductivity values for different MWCNT weight percentages.	56
4.5	Electrical resistance values of a sample containing MWCNT weight percentages of 6 wt% before and after different time intervals from the stress applied on it.	61
4.6	Values of pressure applied on wire with MWCNT weight percentage of 6 wt%.	64
4.7	Values of pressure applied on wire with MWCNT weight percentage of 3.5 wt%.	65
4.8	Values of percentage resistance change obtained applying the same pressure value on the two samples with MWCNT weight percentage of 3 wt% and 6 wt%.	67
5.1	Electrospinning parameters used for PVDF deposition.	71
5.2	β and γ phases peaks position (wavenumber).	72
6.1	Electrospinning parameters used.	78
A.1	Advantages over optical microscopy [110]	85
B.1	Electrical resistance values for each sample with different MWCNT weight percentages and for each Δl	91
B.2	Evaluation of nanofiber mat cross section.	93
B.3	Electrical conductivity values for each sample with different MWCNT weight percentages and for each Δl	94
C.4	Wavenumbers of α , β , and γ peaks of infrared spectra from literature.	96
C.1	Electrospinning parameters used for PVDF deposition in literature.	97
C.2	Electrospinning parameters used for PVDF deposition in literature.	98
C.3	Electrospinning parameters used for PVDF deposition in literature.	99

Chapter 1

Introduction

Sensors deeply impact our lives and play an indispensable role in different fields of applications. With the development of consumer electronics, sensors are used in any technological field, just think of smartphones that are more and more plenty of sensors, typically accelerometers and magnetometers but also pressure sensors, pedometer, and light sensors. According to the technical standard UNI 4546 "Misure e misurazioni - Termini e definizioni fondamentali", a sensor is defined as "a device that is in direct interaction with the measured system". A sensor is a device able to detect a physical quantity of any type (thermal, luminous, magnetic, mechanical, chemical, etc.) and to transform it in another type of quantity, generally electrical (voltage or current). In this way the output signal is easy to manipulate thanks to electronic circuits. In figure 1.1 it is shown a schematic representation of a sensor measurement chain. Thus a sensor is a device able to detect changes or events in the environment and convert the acquired information to an electronic signal [1], [2], [3], [4].

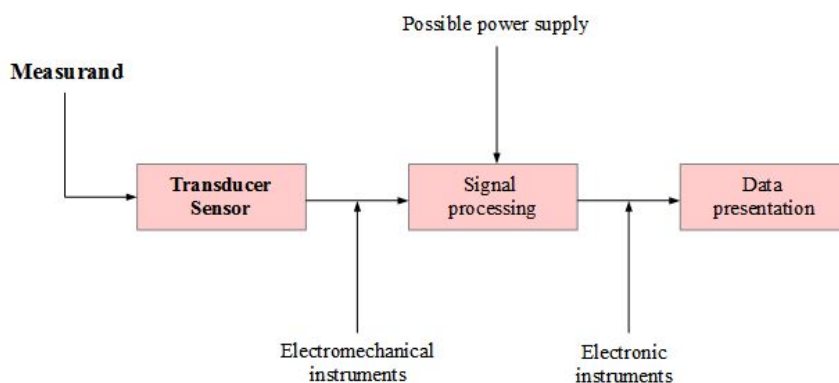


Figure 1.1: Schematic representation of the use of a sensor in a measurement chain [2].

Sensors can be classified according to their principle of operation or according to the type of output signal, but commonly are classified thanks to the type of quantity that

they measure: light sensors, sound sensors, temperature sensors, electrical resistance sensors, sensors of distance, pressure sensors, strain sensors, etc. Sensors are commonly also classified thanks to their energetic behavior [2].

- Active sensors: directly convert the input energy in the output energy, without having to be powered from the outside.
- Passive sensors: need external power supply (excitation) for the conversion.

Sensors are characterized by several important parameters that describe the performance of the sensor [2] [3].

- Accuracy: “maximum deviation between the measurement provided by the sensor and the true value of the measurand” [2].
- Precision or repeatability: “quantifies the ability of the sensor to provide values of the output magnitude little different from each other when the input is applied several times, consecutively, the same by measuring” [3].
- Sensitivity: “ratio between the variation of the output signal to the transducer and the corresponding variation of the input quantity” [2].
- Resolution: “the smallest amount that can be measured, the slightest variation of the input that causes an appreciable variation in output” [2].
- Calibration: “measurement of the output magnitude for known values of the input magnitude to the transducer itself” [2].
- Hysteresis: “quantifies the presence of a "memory" effect of the sensor whose output, at the same value of the measurand, could be influenced by the previous operating condition” [3].
- Linearity: “maximum deviation between calibration curve and a straight reference line” [2].
- Response time: “time taken to reach a predetermined percentage of the final value of the output signal” [2].
- Stability: “is the ability of the transducer to keep unchanged its operating characteristics for a period of time relatively long (months or years)” [3].

Nowadays, there is a growing interest for flexible and stretchable strain and pressure sensors due to the growing demand in several applications in a large variety of fields like industrial, automotive, robotics, sports, biomedical, medical and many others [4], as represented in figure 1.2. Since the scope of strain sensors is to transform a mechanical deformation into electrical signals, they attracted significant interest in recent years, in advanced applications especially to design body-integrated electronic systems able to allow real-time detection and analysis of human-body movements and gestures. The most advanced examples of these advanced systems can be attached directly to the skin (e.g., electronic tattoos) or to clothes (e.g., smart e-textiles) [5], [6], [7]. In this context, motion state sensors mainly focus on the motion of the human body in applications as sport, walk, sleep, rehabilitation

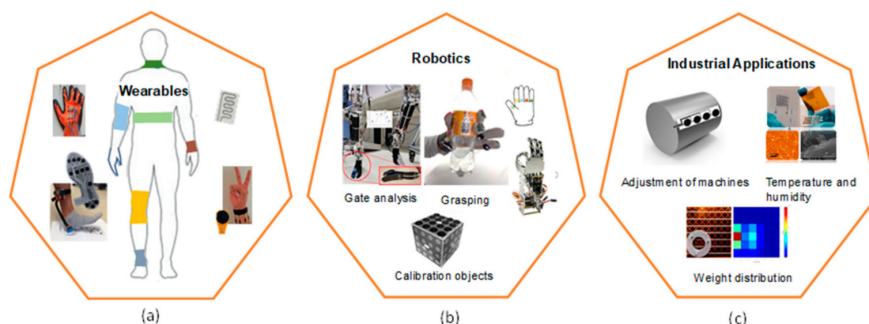


Figure 1.2: Examples of applications of strain and pressure sensor: (a) wearables, (b)robotics, (c) industrial application [4].

and to monitor diseases affecting the physiological movement. Materials selection plays a fundamental role in designing sensors of this kind to ensure a complex set of functional properties required by the final device such as high stretchability, excellent biocompatibility, great conformability, and low cost. To satisfy this complex set of requirements in the literature have been largely [7],[4],[8] investigated the role of nanostructured materials, demonstrating that nanomaterials are the most suitable and promising candidates. Conventional pressure sensors, mainly made of rigid semiconductors, have very high sensitivity and they can achieve good performances but unfortunately exhibit very poor mechanical properties, and the lack of flexibility and stretchability makes them inappropriate in a wide range of emerging applications.

Nanostructured materials are materials which have at least one dimension sized from 1 to 100 nanometers. Accordingly, nanotechnology is the term used to describe the areas of engineering or science in which phenomena occurring in the nanometric dimension are exploited in the design, characterization and realization of new innovative devices or systems. The term nanotechnology was firstly used in the 1960s after the talk of the physicist Richard Feynman “There’s plenty of room at the bottom”, in which he describes the possibility to manipulate objects atom by atom. This talk turned out to be fundamental and prophetic so that, during these years nanostructured materials have found wide use in different sectors precisely because of their excellent and unique properties. At nanoscale, materials properties are even size-dependent: surface effects become important and quantum effects may become dominant when one reaches the interatomic distance range. This brings to important changes in mechanical, fluidical, electromagnetic and thermodynamic laws with respect to the macroscopic world. For example, in the nanoscale world, for what concerns mechanical properties, surface and interface forces become dominant such as adhesion forces, capillary forces and strain forces. Moreover, for what concern electrical properties, a quantum mechanical effect known as tunneling become predominant changing completely the electronic properties of solids with respect to the macroscopic world. All the new properties that characterize materials at the nanometer scale enable new and innovative applications, like what happen in the field of flexible sensors where they play a crucial role. Nanostructured materials, thanks to their properties, especially high surface area to volume ratio, offer important strategies to design flexible sensors with superior

electrical and mechanical performances, overcoming many limitations of traditional flexible materials such as polymers [9].

In the nanoscale world, nanofibers (NFs), and especially electrospun NFs, received considerable attention from the field of soft electronics owing to their promising advantages and superior properties in flexibility and/or stretchability and conductivity, emerging as one of the most important class of nanomaterials in the sensing field [10]. NFs are one-dimensional nanostructures, with diameters less than 100 nm but with length variable from tens of micrometers to kilometers, offering the possibility to link the nano- with the macro-world. Several processing techniques exist to produce nanofibers such as mechanical drawing [11], template synthesis [12], phase separation [13], self-assembly [14] and electrospinning. Moreover, when fabricated by electrospinning [10] [15], NFs become even more attracting because the production process is simple, low cost, versatile, reliable and robust. This technique brings to a simple production of nanofibers with very interesting morphological characteristics, like high surface area to volume ratio or small size pores not achievable with other deposition techniques. Another great advantage of the electrospinning process is the possibility to obtain NFs of a wide range of materials starting from polymeric solutions. Although the greater part of the produced nanofibers is polymeric, ceramic and metal nanofibers can also be obtained through further post-treatments. A green process for the fabrication of the sensor can be ensured thanks to this huge variety of starting solutions suitable for electrospinning. Furthermore, the nanofiber mat obtained through electrospinning can be easily functionalized not only by traditional approaches based on functionalizing the surfaces after electrospinning, but also by blending the polymeric material with a functional one prior to spinning [16], or by the fabrication of specific nanostructures decorating the NFs [17]. The electrospinning process ensures indeed to obtain a high quantity of nanostructures: NFs, beaded NFs [18], core-shell NFs [19], hollow NFs [20]. Strictly correlated with the counter electrode, planar [120] or rotating drum [119], the nanofibers can be collected in a random mode distribution or in ordered, aligned one. They can be collected on a flat collector or on a cylindrical one bringing to the production of NFs with different morphological characteristics.

Features of nanofibers deposited by electrospinning are exceptional and unique, so that, as shown in figure 1.3 from the work of Quaglio M. and Massaglia G. published in 2017 [21], the interest of researchers grows day by day, as evidenced by the increase in publications year after year.

The purpose of this thesis is to develop flexible pressure sensors using polymer-based nanofibers as the functional nanomaterials. Polymer-based nanofibers are an emerging class of nanostructures, and they are composed by organic filaments with the transversal dimension less than 100 nm and length variable from tens of micrometers to vary large values such as kilometers. At molecular level, nanofibers are constituted by very long and linear polymeric chains, that are aligned in the fiber direction. Therefore, the resistance to stretching is given by the strength of the covalent bonds of the chain of the polymer and the stability of the structure depends on the intermolecular forces of attraction (bonds hydrogen, dipole-dipole forces, Van der Waals forces) that prevent extended chains from fold up. Moreover, using the electrospinning system, it is possible to use a large variety of polymers and, simply by changing some parameters, nanofibers with different shapes and properties can be obtained. In addition, using biocompatible polymers the electrospinning process results to be ideal to fabricate substrate NFs mats for flexible/stretchable electronic

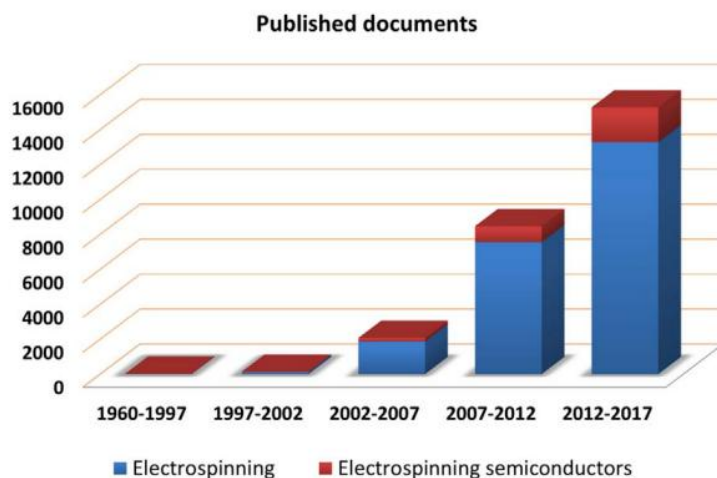


Figure 1.3: The increasing number of published works in the field of electrospinning. The red part is related to the electrospinning of semiconductors. Reprinted from [21], Copyright (2018), with permission from Elsevier.

devices that directly interface with tissues, organs, or cells [22].

The development of electrospun NFs enhance the stimuli response of flexible pressure sensors working according to different sensing mechanisms, such as piezoelectric, capacitive, triboelectric and piezoresistive. In this thesis the piezoresistive and the piezoelectric mechanisms are investigated, with the aim to demonstrate the possibility to optimize polymer-based NFs suitable to detect static and quasi-static mechanical signals as well as mechanical signals rapidly changing over time.

To this purpose, poly(vinylidene fluoride) (PVDF) has been selected because of its piezoelectric properties that can be further enhanced by nanoconfinement during the nanofiber deposition by electrospinning [15]. On the other hand, composite nanofibers, containing smart carbon nanomaterials as the conductive nanofillers, exhibit a significant change in their resistivity with strain and therefore they have been selected for the realization of piezoresistive pressure and strain flexible sensors, due to their superior performances. Among all the smart carbon materials, carbon nanotubes (CNTs) with their large aspect ratio (diameters ranging from 1 to 100 nm and lengths of up to mm) and conjugated structure, have been selected in this thesis, since they are the best choice for the realization of nanocomposite polymer NFs to enhance mechanical and electrical properties in comparison to other nanofillers.

This thesis especially offers a deep investigation of the role of electrospinning process parameters on the final properties of PVDF piezoelectric NFs and CNTs-based piezoresistive NFs. Along with conventional parameters such as the working distance and the applied voltage, particular attention is paid to analyze the role of rotating drum collectors (i.e. rotating collecting electrodes) with different diameters (from few millimeters up to ten centimeters) on the final morphology and properties of the resulting functional nanofibers.

The use of rotating drum collectors allows to collect nanofibers mats with different architectures, from the conventional planar one to wire shapes and tubular arrangements, moreover obtaining different degrees of alignment of the nanofibers inside them. In this thesis it is demonstrated that the use of rotating electrodes is an effective method to modify and thus tune the piezoelectric and piezoresistive response of the NFs-based flex-sensors.

In more details, the second chapter “The fundamental theoretical aspects” gives a brief and general introduction to the main transduction mechanisms of flexible mechanical pressure sensors, highlighting the piezoresistive and piezoelectric effects and the possibility of combining them in a single sensor. Significant importance has been given to nanocomposite materials for the realization of piezoresistive sensors and to polymeric materials, in particular PVDF, for the realization of piezoelectric sensors.

In the third chapter “The electrospinning process” is described the electrospinning process, the nanofiber production process used in this work and the core of this thesis. Particular attention was given to the parameters that influence the morphology and properties of the deposited nanofibers. Finally, there is a description of how electrospinning parameters influence the formation of the β crystalline phase in the electrospun PVDF, in order to enhance its piezoelectric properties.

In the fourth chapter “Piezoresistive analysis” are initially described materials and electrospinning configurations used for the deposition of composite nanofibers. Electrical and morphological characterization used to achieve the final implementation of the percolation curve, are after exposed. Subsequently, obtained results are shown, trying to critically comment them in comparison with results present in literature. Finally, the piezoresistive behavior of samples obtained by the electrospinning of solutions containing two different weight percentages of conductive filler inside the polymer matrix, is performed.

In the fifth chapter “Piezoelectric analysis” materials and electrospinning configurations used for the deposition of PVDF nanofibers, are described. After a section dedicated to the choice of the electrospinning parameters used for the deposition of the PVDF solution in order to enhance its piezoelectric properties, the FT-IR and piezoelectric characterization is illustrated. After that, it is done a brief discussion on the possibility to realize a layer-by-layer deposition of PVDF nanofibers on a conductive core made of PEO/MWCNT composite nanofibers.

Chapter 2

The fundamental theoretical aspects

2.1 Transduction mechanisms of mechanical signals in electrical one

In pressure sensors, the transduction of the imposed force/angle deformation into an electrical signal is mainly obtained thanks to triboelectric, capacitive, piezoresistive and piezoelectric mechanisms, as represented in figure 2.1 [23].

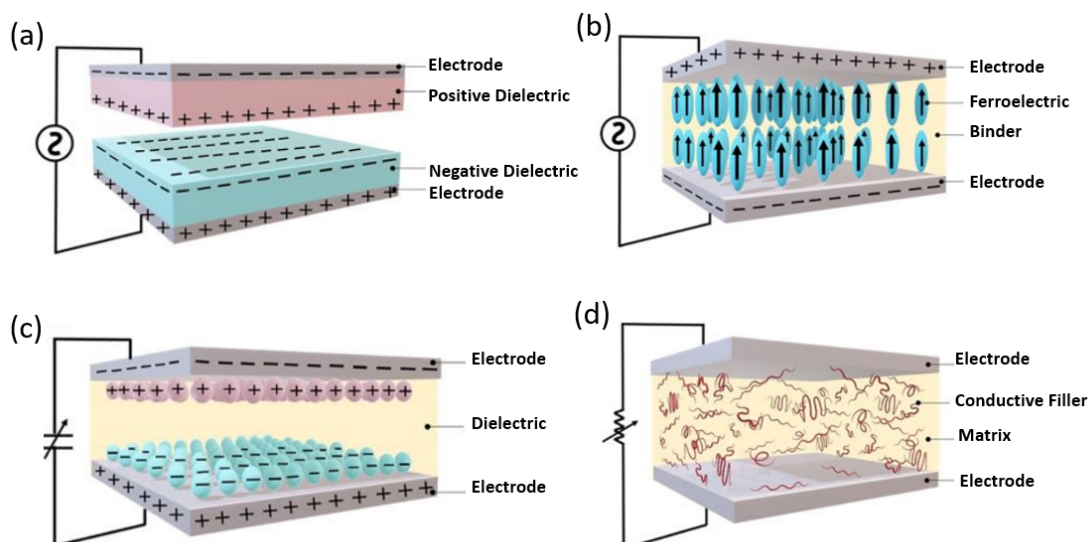


Figure 2.1: Schematic illustration of electromechanical sensors: (a) triboelectric, (b) piezoelectric, (c) capacitive and (d) piezoresistive [23].

2.1.1 Triboelectric effect

The triboelectric effect consists in a generation of triboelectric charges when two dissimilar materials are in contact. Triboelectric charges are generated because of the charge transfer from the material with lower surface electron affinity to the material with the higher one [23]. Recently, triboelectric nanogenerators (TENGs) have demonstrated excellent performances in the design of mechanical sensors because of their ability to transform different types of mechanical stimuli such as pressure, vibration or body motion, into electricity. Indeed, thanks to the mutual movement of two different materials, opposite static charges will be generated on the surfaces when they get in contact. Therefore, on the back side of these two materials the same amount of charge but with opposite polarity is generated. Finally, a potential difference is created bringing to an electron transfer through the external circuit until the two materials are again separated. Thanks to the choice of different materials, more or less charges are generated. Moreover, positive triboelectric materials refer to materials that tend to accumulate a positive charge, while negative ones tend to accumulate a negative charge. TENGs can be realized with four different operating modes: vertical contact separation, in-plane sliding, single electrode and freestanding triboelectric layer [23]. Sensors based on triboelectric effect become widely used in different kind of application such as wearable devices [24], human monitoring sensors [25] and energy harvesting systems [26].

2.1.2 Capacitive effect

Capacitive effect is one of the most widely used transduction mechanisms that transform the mechanical deformations caused by applied pressure or strain to electrical resistance variations. A capacitive sensor is a particular type of sensor that takes its name from the variation it measures, the "electrical capacitance". Capacitors are generally composed by a dielectric material of thickness d and with a relative permittivity equal to ϵ_r sandwiched between two electrodes, like represented in figure 2.1 (c). Capacitance is defined as the ratio between the amount of charge accumulated by the two electrodes and the potential difference between them and can be described by the equation $C = \epsilon_0 \epsilon_r A/d$, where ϵ_0 is the vacuum permittivity and A is the overlapped area of the two electrodes. This equation, so the capacitance value, under the application of a tensile or compression stress, can be changed because of the variation of all the parameters except for ϵ_0 .

The capacitance change induced by the application of an external pressure usually exhibits excellent linearly but low sensitivity [23]. In addition, conventional capacitive sensors based on semiconductors have poor mechanical properties, are hard and brittle, and so cannot be used for the realization of flexible sensors [27]. Therefore, to replace silicon-based materials various polymer-based materials, such as polydimethylsiloxane (PDMS) [28] and polyurethane (PU) [29] have been proposed in literature and widely used as flexible substrates for capacitive sensors. These polymers have an high degree of stretchability and have also desirable biocompatibility, often required in biomedical applications, but show low sensitivity and low response time [27]. An higher sensitivity can be achieved realizing sensors based on nanostructured material, especially composite nanofiber membrane [30]. For example, in the work of Xiaofeng Yang et al. [30], a highly sensitive flexible capacitive sensor based on the electrospun CNT/PVDF composite nanofiber membrane was

developed.

2.1.3 Piezoresistive effect

Piezoresistivity is the characteristic of materials able to vary their electrical resistance, if subjected to the action of an external force. If a piezoresistive material is strained or deflected, its internal resistance will change and stay changed until the material's original position is restored. So, the piezoresistive effect is a change in the electrical resistance of a material when a mechanical strain is applied and, in contrast to the piezoelectric effect, doesn't cause a change in the electric potential.

The piezoresistive effect was firstly discovered by Lord Kelvin in 1856, when he observed a change of electrical resistance in a metal device due to the application of a mechanical load. After that, in 1954, Smith was able to detect the large piezoresistive effect in silicon and germanium bringing to the development of piezoresistive sensors. After World War II, the adoption of these sensors began to open new scenarios in emerging fields such as robotics, with the first examples of tactile sensors, favoring the birth of new classes of materials that fit the various requirements. So, the investigation was starting on a new class of composites consisting of conducting particles dispersed in an insulating matrix. Especially, moving from the macro to the nano-world, nanocomposite piezoresistive material provide a good alternative to conventional materials used before due to their higher sensitivity, easy manufacturing [31]. Moreover, thanks to the use of material based on polymer nanocomposite containing smart carbon nanomaterials gained tremendous attractivity in the realization of flexible sensors due to their superior sensitivity, high flexibility and biocompatibility. Finally, composite electrospun nanofibers are a good candidate for the realization of piezoresistive sensors because of the possibility to link the superior properties of nanocomposites in the realization of flexible sensors with the advantages in the use of nanofiber production by electrospinning [32], [33], [34].

Among all the sensing mechanisms for the realization of pressure sensors, piezoresistive pressure sensors have been widely adopted because of their simple device structure and easy signal processing [35].

The sensitivity of a piezoresistive device is characterized by the gauge factor. The Gauge Factor (GF) or strain factor of a strain gauge is the ratio of relative change in electrical resistance to the mechanical strain, which is the relative change in length. This can be mathematically written as:

$$GF = (\Delta R/R)/(\Delta L/L) \quad (2.1)$$

where:

- $\Delta R/R$ is the unit change in resistance;
- $\Delta L/L$ is the unit change in length.

It is known that the strain of an elastic material is defined as:

$$\epsilon = \text{change in length}/\text{originallength} = \Delta L/L \quad (2.2)$$

So, the GF can be written as:

$$GF = \epsilon(\Delta L/L) \quad (2.3)$$

2.1.4 Piezoelectric effect

The word “piezoelectricity” is linked to the Greek word “piezo”, which means stress [36]. Indeed, when piezoelectric materials are subjected to a mechanical stress, they can create electrical charges between its two opposite sides. On the other hand, piezoelectric materials can generate a mechanical strain if subjected to an electrical field. Those two are the direct and reverse piezoelectric effects (figure 2.2). Devices based on the direct effect can be used to detect strain, movement, pressure, force, or vibration by developing appropriate electrical responses, as in the case of force and acoustic or ultrasonic sensors. On the contrary, the indirect effect can be used to generate strain, movement, pressure, force, or vibration through the application of suitable electric fields in actuators or energy converters.

The piezoelectric effect in inorganic crystals was firstly discovered in 1880 by Pierre and

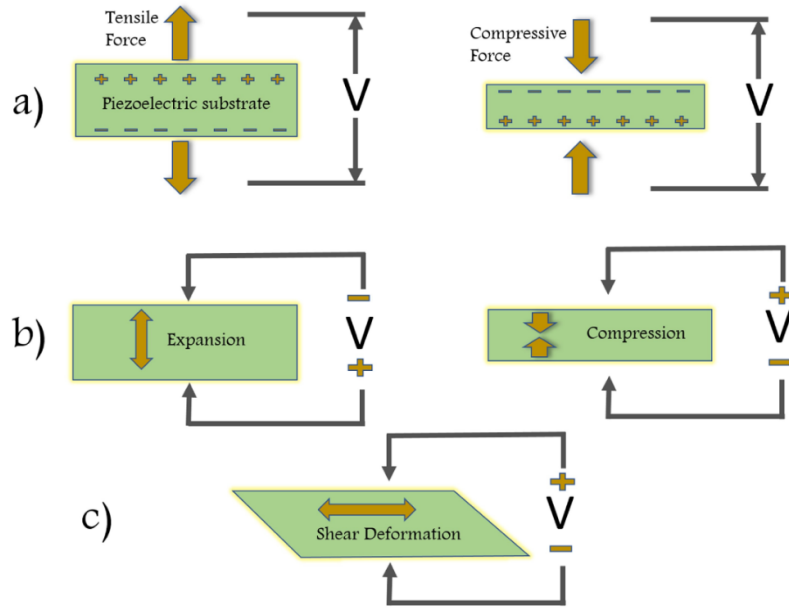


Figure 2.2: Schematic representation of the piezoelectric effect in three cases: longitudinal deformation in the direct (a) and indirect (b) case, (c) shear deformation [37].

Jacques Curie. They played a key role in the study of the direct piezoelectric effect in quartz and, successively, thanks to Gabriel Lippman, the discovery of the inverse piezoelectric effect. After that, no significant development was made until the discovery of new synthetic piezoelectric materials: lead zirconate titanate, known as PZT, and Barium titanate (BaTiO_3) in the 1950s. Interest in a new class of piezo-materials, piezoelectric polymers, began in 1969 when Heiji Kawai discovered piezoelectric effects in the synthetic polymer poly(vinylidene fluoride) (PVDF) [37]. Especially, in the literature it has been demonstrated that piezoelectric properties can be further enhanced by nanoconfinement during the nanofiber deposition by electrospinning [15], demonstrating that PVDF nanofibers are a good candidate for the realization of flexible pressure sensors based on piezoelectric effect. So, PVDF nanofibers due to its excellent piezoelectric properties can be used for different type of flexible sensors, like what is done by Khan et al. that have realized a smart glove

made of stretchable strain sensors assembled in each finger [38].

Two equations are used to describe the relation between electrical and mechanical properties in piezoelectric materials equation 2.4 and equation 2.5:

$$x_i = S_{ij}^D \sigma_j + d_{mj} E_m \quad (2.4)$$

$$D_m = d_{mj}^D \sigma_i + \epsilon_{ik}^{\sigma} E_k \quad (2.5)$$

where σ is the stress Vector (N/m^2), x is the strain vector (m/m), E is the applied electrical field in (V/m), ϵ is the permittivity in (F/m), d is the piezoelectric constant (m/V), S is the matrix of compliance coefficients (m^2/N), D is the electrical displacement (C/m^2) and $i, j = 1, 2, \dots, 6$ and $m, k = 1, 2, 3$ refer to different directions within the material coordinate system [37].

2.1.5 Combination of piezoelectric and piezoresistive effect

Traditional pressure or strain sensors commonly rely on one single mechanism among piezoelectric or piezoresistive effect. With the main aim to realize a sensor able to detect both static and highly dynamic signals, the combination/coupling of piezoelectric and piezoresistive mechanisms in one single flexible sensing unit can be a very effective strategy.

An example of a strain sensor, based on the combination of both piezoresistive and piezoelectric effects is reported in literature [39]. As it is known, flexible piezoelectric sensors can measure only high-frequency dynamic signals due to the characteristics of piezoelectric materials, but they can't be used for static detection because they show poor sensitivity and reliability at low frequency [39]. On contrary, flexible piezoresistive sensors are used for static and low frequency detection but they show poor highly dynamic responses. So, it can be useful to combine the two mechanisms to achieve simultaneously both highly dynamic and static detection capabilities from zero to high frequency. In line with this working principle, Lijun et al. [39] proposed a strain sensor where the piezoresistive layer was fabricated by anchoring highly conductive graphite sheets (GS) into a (PVDF) electrospun nanofibrous membrane for static and low frequency signal detection, while pure piezoelectric PVDF based piezoelectric sensor and array was selected for highly dynamic monitoring. Flexible and insulating polydimethylsiloxane was used to decouple the two sensing layers.

2.2 Nanocomposite materials for flexible pressure sensors

Nowadays, composite materials become widely used in different fields of application thanks to their extraordinary properties. Composite materials, i.e., materials born from the combination of two conventional materials, presents properties otherwise impossible to obtain. Generally, composite materials are obtained by the union of a principal phase, called matrix and which occupies most of the volume, and a secondary phase, called filler and which is dispersed in the matrix and gives it the desired properties. Matrices, in general, are classified into three main categories: metallic, ceramics and polymers. The category of fillers,

on the other hand, is much wider. These can in fact present themselves in different shapes and sizes, for each of which different effects are obtained once the filler has been dispersed in the matrix. Among all the possible matrices, polymeric materials received a considerable attention, especially when organized in nanostructures [40]. Polymer-based composite nanomaterials, based on smart carbon nanomaterials, like graphene or carbon-nanotubes, show optimal coupling of mechanical flexibility and electrical performance and have been widely employed as the functional material into flexible mechanical sensors.

Nanocomposites are a particular type of composite materials belonging to nanomaterials wherein one or more phases at nano-sized dimension (zero dimension, one dimension, and two dimensions) are embedded in a ceramic, metal, or polymer material (figure 2.3). These can be made by inorganic or organic components at the molecular level to obtain new properties [41].

The properties of a polymeric material change radically later to the addition of car-

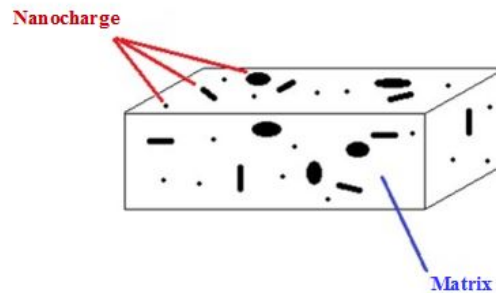


Figure 2.3: Schematic representation of nanocomposite materials.

bonaceous type fillers. Indeed, generally polymers are considered insulating materials, but, thanks to the addition of a conductive filler, the conductivity can change. In this way, the conductive filler is able to create a network inside the polymer matrix, thanks to which electrons can freely move, and so generate a current. To have the formation of such a network, however, the concentration of the filler must be higher than a certain value, called "percolation threshold". It has been observed that beyond a critical concentration of filler, the electrical conductivity of the material can increase up to 12 orders of magnitude, transforming the material from insulator to conductor. Below the percolation threshold, electrons are unable to move freely, and electrical properties are dominated by the matrix. For what concern the choice of the polymeric matrices, researchers investigate different type of electrically conducting and non-conducting polymers like PVDF [42], PANI/PDMS [43], TPU [4], etc. In the same way different nanofillers such as graphene [31], silver nanowire [44], metal oxide nanowires [45] and carbon nanotubes can be chosen. Among all the possible nanofiller types, CNTs have the capability to enhance mechanical and electrical properties in comparison to other nanofillers. Indeed, CNTs have a large aspect ratio (diameters ranging from 1 to 100 nm and lengths of up to mm) and a conjugated structure promoting a ballistic charge transport. Hence, electrical conductivity of composite is enhanced at a very low concentration in comparison to other conductive fillers (figure 2.4) [4].

Due to the sp² hybridized carbon-carbon bond structure of Carbon Nanotube (CNT),

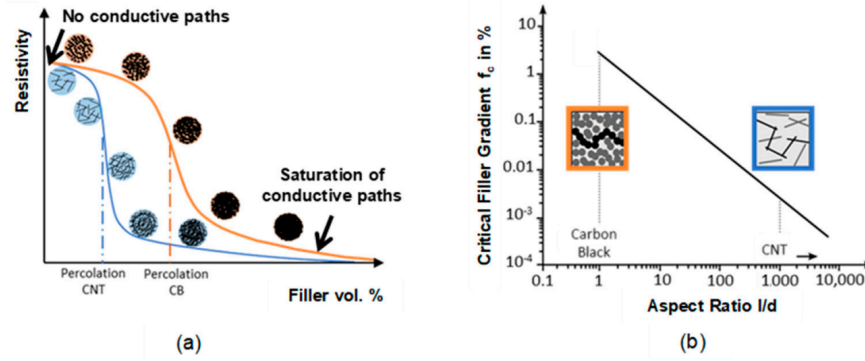


Figure 2.4: Influence of filler type on composite material behavior: (a) Resistivity behavior of composite as a function of filler concentration for two types of filler (carbon nanotubes and carbon black), (b) critical filler gradient as a function of aspect ratio for CNTs and CB [4].

it has intrinsically high electrical conductivity (10^3 – 10^5 Scm^{-1}), high electron mobility (10^4 – 10^5 $cm^2/(Vs)$) and high mechanical tensile strength (5-200 GPa), properties that they make it very interesting for different applications. Moreover, due to the Van der Waals force existing between the surface of the CNTs, it tends to agglomerate and hinders the formation of electrical conducting network in the polymer matrix [42].

Like previously said, during my thesis project, I optimized composite nanofibers by electrospinning made of Polyethylene oxide as the matrix and Multi Wall Carbon Nanotubes as the conductive filler obtaining PEO/MWCNTs NFs that are here investigated as the sensitive material for piezoresistive flexible sensor, taking finally all the advantages listed above of nanocomposite materials, because nanofibers show the same and sometimes improved properties of this type of material [46], for the realization of piezoresistive sensors together with the easy production of nanofibers by electrospinning.

Moreover, it is important to underline the role of the dispersion of CNTs inside the polymer matrix during the preparation of the solution to be electrospun. Indeed, a low electrical percolation threshold is supported by good dispersion of CNTs and the formation of a suitable network structure inside the polymer matrix. So, suitable dispersion and homogenous distribution of CNTs into polymer matrices is one of the major challenges.

2.2.1 Dispersion of CNTs in polymer matrices

Several methods are used to obtain successful dispersion of nanotubes in polymer matrices dry powder mixing, solution blending, melt blending and surfactant assisted mixing [47]. Among them, in this work, the surfactant-assisted dispersion with sonication and stirring is used, like will be explained next. Optimum physical blending is necessary to achieve a good dispersion of filler in the polymer matrix. To favor and improve the dispersion of CNTs in a polymer matrix, high power dispersion methods, such as ultrasound and high-speed

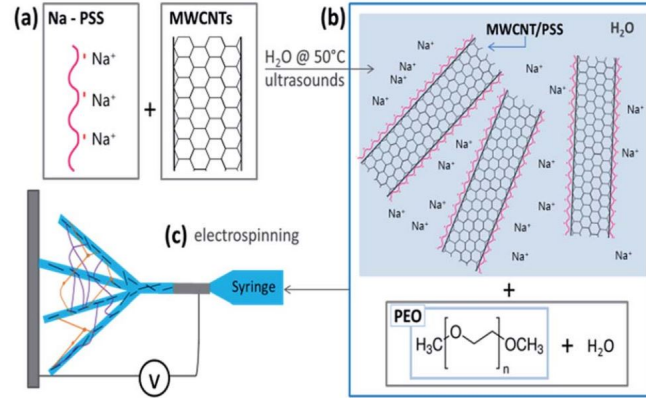


Figure 2.5: Process flow for the preparation of the MWCNT/PSS/PEO solution to be electrospun [46].

shearing can be used. It is possible to use two types of ultrasonication: one with a sonicator bath and one that involves a sonicator tip. It is important to pay attention during the sonication process because, if it is done for a too long period, can lead to a reduction of the length of carbon nanotubes, to ruining the polymer matrix and subsequently to decrease the nanocomposite properties.

Sandler et al [48] proved that thanks to the high-speed stirring, 2000 rpm for 1h, it is possible to improve the CNTs dispersion in an epoxy matrix. The addition of surfactants as a dispersing agent can improve the dispersion of CNTs in polymer/CNT composites. Surfactant molecules get randomly adsorbed on the nanotube surface and act as bridges between the nanotubes and polymer chains. For example, like exposed in figure 2.5, Tung, Tran Thanh, et al. [49] made use of the surfactant sodium polystyrene sulfonate (Na-PSS) to favor the dispersion of MWCNTs in the PEO polymer matrix.

2.2.2 Percolation model

The percolation model is introduced to explain the conductivity behavior of nanocomposite structures, and in particular of composite nanofibers. Thanks to the addition into polymeric materials of carbon fillers such as carbon fibers or synthetic graphite, the electrical conductivity of such materials can be changed drastically, obtaining nanocomposite materials.

Adding carbon fillers, with very high electrical conductivity, inside the polymeric matrix, electrical properties of the polymer can be improved. The improvement of electrical properties is linked to the formation of a continuous conductive network inside the polymer matrix when conductive particles are enough to be close to each other (figure 2.6). The conductive network formation is linked to the filler volume fraction and to the type, size, shape, and orientation of that conductive filler [50] [51].

When the conductive filler volume fraction is too low, the conductivity of the composite is still very similar to the one of the pure insulating polymers. Increasing the filler volume

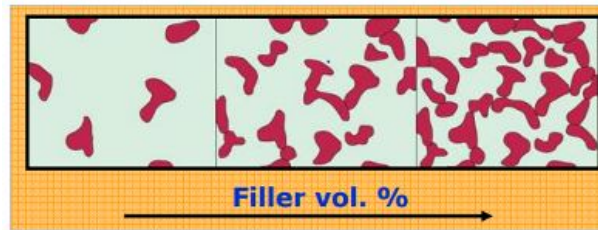


Figure 2.6: Change of the structure of the composite material increasing the filler concentration [52].

fraction, at some critical value, known as percolation threshold, the conductivity of the composite starts to increase many orders of magnitude with a very low increase of the filler fraction, because of the contact between filler particles.

Composite conductivity, after the region of its drastic increase, begins to stabilize to a

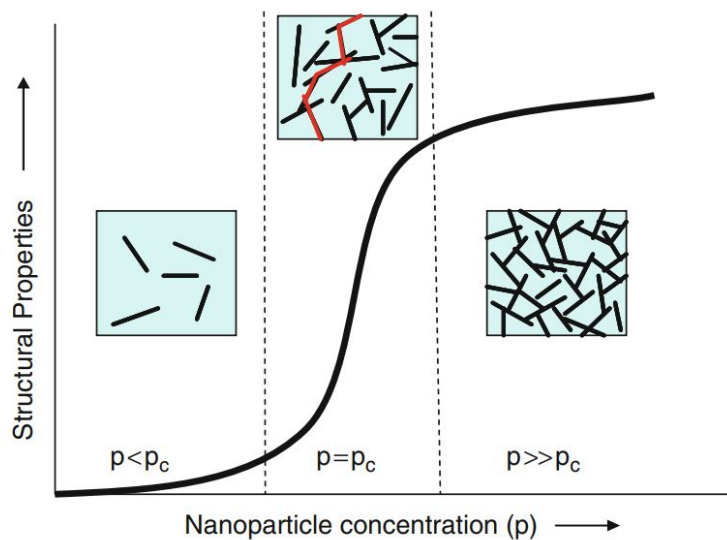


Figure 2.7: Typical percolation curve related to polymer nanocomposite structure with the increase of nanoparticle concentration, highlighting the critical path at the onset of percolation, denoted by red line. Reprinted by permission of Springer Nature Customer Service Centre GmbH [53], Copyright (2008).

certain value very similar to the one of the filler materials. Figure 2.7 shows the composite electrical conductivity curve with the three main regions that characterize the percolation theory.

Like previously said, researchers demonstrate that the shape of the filler strongly influence the conductivity of the nanocomposite and the percolation threshold. It is important to underline that, carbon nanotubes (CNTs), with their nanometer length scale (diameter)

and high aspect ratio (length/diameter), shows a lower percolation threshold with respect to spherical or smaller particles [4].

As said before, the continuous and homogeneous dispersion of the conductive filler inside the polymeric matrix is also responsible of the reduction of the percolation threshold. There are several dispersion techniques that can be used but one general rule helps the reduction of this percolation threshold. Small differences between the surface energy of the filler and polymer leads to a better and more uniform filler dispersion and so to the formation of a more uniform conductive network.

It is not necessary to have contact between filler particles to have conduction. Indeed, the conduction can be present also below the percolation threshold. Three different mechanisms are present [54]:

- Electron flow through the conductive network formed by the conductive filler inside the polymer matrix when the percolation threshold is achieved.
- Electron hopping mechanism, that consists in the jump of electrons between two adjacent conductive particles, when the distance between them is sufficiently small.
- Magnetic field radiation.

The percolation model can be mathematically described by the electrical conductivity as a function of the filler content above (equation 2.6) and below (equation 2.7) the percolation threshold respectively.

$$\sigma = \sigma_0 \cdot (p - p_c)^s \quad (2.6)$$

$$\sigma = \sigma_d \cdot (p_c - p)^t \quad (2.7)$$

In this model [46] are present various parameters:

- p_c is the percolation threshold;
- σ is the electrical conductivity of the nanocomposite material;
- p is the weight percentage of conductive filler;
- σ_0 , σ_d , t and s are fit parameters.

Specifically, t (or s) parameter can be chosen considering different values of the critical exponent t and the critical threshold p_c measured in various composites including carbon-black-polymer systems, oxide-based thick film resistors and other metal-inorganic and -organic insulator composites. In figure 2.8, is represented the collection of 99 different values of this parameter, used by different research groups, that help to understand the range in which t parameter has to be chosen.

2.2.3 Piezoresistive effect in CNTs/polymer composites

Strain or stress sensors based on CNT/polymer composites show an excellent piezoresistive behavior with respect to conventional strain sensors because of their much higher sensitivity [56]. The piezoresistivity in this excellent class of materials is defined as the ratio between the electrical resistance change due to the applied stress and the initial electrical

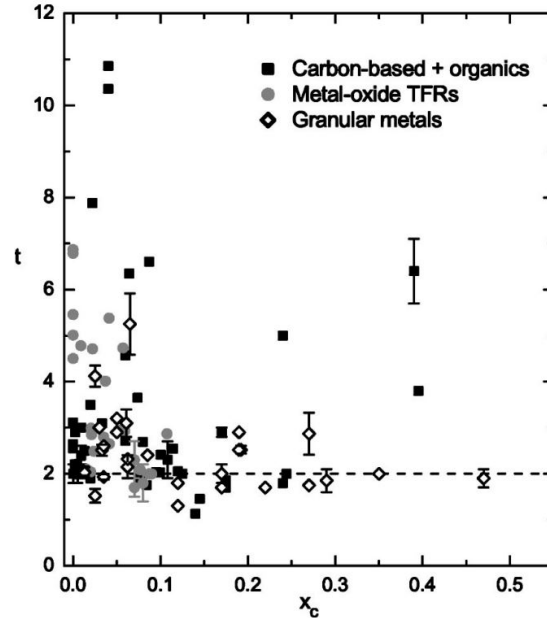


Figure 2.8: Collection of values t and corresponding critical threshold concentration x_c for various disordered conductor-insulator composites. The dashed line highlights the universal value of t . Reprinted with permission from [55], Copyright (2005) by the America Physical Society.

resistance.

Different groups of researchers try to explain the piezoresistive mechanism in nanocomposite materials. They found that the piezoresistive behavior of these materials is mainly due to three fundamental mechanisms:

- Under strain there is a change in the conductive network inside the polymer matrix. This happens because with the application of strain, existing conductive paths can be broken, or new ones can be formed because of the variation of the distance between two CNTs. This obviously can lead to a variation of the electron path and so, to a change in resistance.
- Under strain the tunneling distance between two neighboring CNTs can be varied, leading again to a possible resistance change. A lot of researchers have proposed a resistor network numerical model to predict the piezoresistive behavior of nanocomposite materials [56] [57]. In these models, the tunneling effects among neighboring CNTs play an important role (figure 2.9).
- The piezoresistive effect in CNTs themselves must be considered.

Different studies found that piezoresistivity in a composite material tends to be stronger when the conductive filler is at a volume fraction near the percolation threshold [58]. Since around the percolation threshold, the resistivity changes abruptly with the filler volume

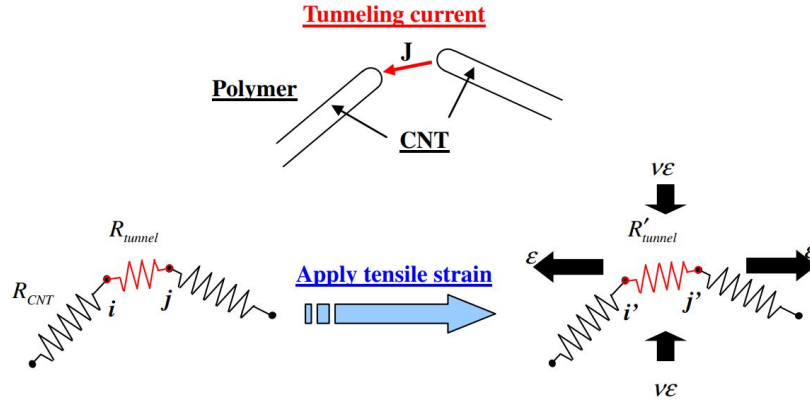


Figure 2.9: Schematic representation of the tunneling between neighboring CNTs [57].

fraction and this translates to a situation in which a small change in strain causes a relatively large change in the resistivity.

In the work of Myounggu Park et al [59], the deformation-dependent electrical resistance of MWCNT/PEO is studied. The pattern of electrical resistance change versus strain for the specimens of a certain volume of MWCNT consists of a linear region followed by nonlinear one. This is probably linked to the validity of the percolation theory in the two regions. In the linear region, the strain applied is not so high and the overlapping contact of MWCNTs inside the matrix is maintained. When the applied strain becomes too high that the overlapping contact of MWCNTs is lost, and thus the percolation-based theory is no more valid.

2.2.4 PEO and CARBON NANOTUBES arranged as polymer-based composite

Since in this thesis composite electrospun nanofibers made of PEO/MWCNT were studied, a brief review of the principal features of PEO and CNTs arranged as polymer-based composite is necessary. It is important to underline the fact that all the properties of nanocomposite materials previously described are valid and usually are also improved in composite nanofibers for example achieving very low percolation threshold [60] [61]. In addition, composite nanofibers made by electrospinning offer the unique possibility to tune their morphology and their electrical behavior simply by changing some electrospinning parameters [46].

Polyethylene oxide (PEO) is a polymer prepared by polymerization of ethylene oxide (figure 2.10). Like in most of polymers, the physical properties vary according to the average number of repeating units, while the chemical properties remain almost unchanged. PEO is soluble in water, methanol, benzene, dichloromethane, while it is insoluble in diethyl ether and hexane. Regarding electrospinning, due to the relatively high molecular weight, good solubility in many solvents and its viscosity, PEO is widely used for studying the electrospinning process and the morphology and structure of its electrospun nanofibers.

With the discovery of carbon nanotubes (CNTs) by Iijima, the electrospinning process was

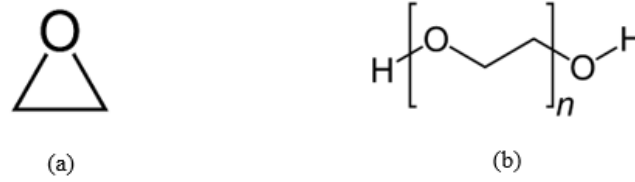


Figure 2.10: PEO polymeric chain (b) from synthesis of Ethylene oxide(a).

intensively used to fabricate nanofibers of PEO in which multiwalled carbon nanotubes (MWCNTs) are embedded. The mixture between the polymer matrix and a conductive charge is done to make a polymer electrically conductive so that the electrical properties of the compound are modified.

Carbon has many allotropic forms such as diamond, graphite, graphene, fullerenes, and carbon nanotubes belong to one of them (figure 2.11).



Figure 2.11: Crystal structure of different allotropes of carbon. Three-dimensional diamond and graphite (3D), two-dimensional graphene (2D), one dimensional nanotube (1D) and zero dimensional buckyballs (0D). Reprinted from [62], Copyright(2007), with permission from Elsevier.

Although the discovery of carbon nanotubes is attributed to Iijima, in 1953 some Russian researchers already published scientific articles where a graphite tube with a diameter of a few tens of nanometers is clearly shown. In 1985 the American chemist Richard E. Smalley discovered fullerenes. In particular, he observed that carbon atoms, under special conditions, can form stable molecules of spherical or ellipsoidal shape very similar to a soccer ball. C₆₀ is the most known fullerene, and it is composed by 60 carbon atoms arranged in hexagonal and pentagonal structures, that together form a sort of cage, a spherical fullerene. Cylindrical fullerenes are known as carbon nanotubes and their length is much greater than their diameter, they are hollow inside as pipes. They can be closed or not at the ends and, ideally, these ends are hemispheres. Iijima discovered a way to synthesize single-walled carbon nanotubes thanks to the arc-discharge technique. Nowadays, carbon nanotubes are mainly produced by three techniques: arc-discharge, laser ablation, and catalytic growth [63].

Carbon nanotubes can be classified into two categories:

- Single Walled Carbon Nanotubes (SWCNT) (figure 2.12 (a)): they are considered very interesting thanks to their extraordinary electronic properties. They are generated from a sheet of graphite rolled on itself to form a cylinder. SWCNT can be extremely long with a very small diameter (that can vary more or less from 1 to 10 nanometers).

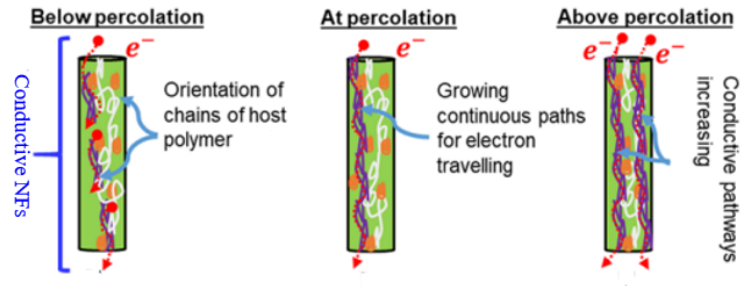


Figure 2.13: Conductive pathways increasing from below to above percolation threshold in electrospun NFs. Reprinted with permission from [70], Copyright (2021) American Chemical Society.

Like it was said before, piezoelectric materials can also exhibit the inverse piezoelectric effect. Indeed, with the application of an electric field, the piezoelectric material will undergo an elastic deformation that brings to an increase or decrease of its length, according to the electric field polarity.

Some piezoelectric crystals, like quartz, Rochelle salt and Topaz, occur in nature and they must be oriented and cut along specific crystallographic directions to obtain the best piezoelectric response. After the discovery of the first polycrystalline ferroelectric ceramic, Barium titanate, a new class of synthetic materials, piezoelectric ceramic with perovskite structure, shown in figure 2.14, started gaining popularity.

The general structure of perovskites is shown in the above figure, where A represents a

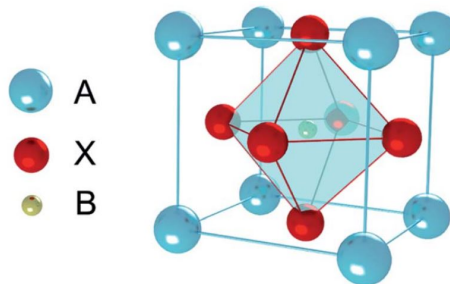


Figure 2.14: Perovskite general structure ABX_3 [65].

cation like Ba^{2+} or Pb^{2+} , B is a cation like Ti^{4+} or Zr^{4+} , X is an anion like oxygen.

Above a specific temperature, called Curie temperature, the lattice has a cubic structure. Below the Curie temperature, it is possible to have the piezoelectric effect (figure 2.15). Because of the application of a mechanical stress or an electric field, the central cation of the perovskite structure, e.g., Ti^{4+} or Zr^{4+} , can be moved from its central position and a separation of charges that produces an electric dipole with a single axis of symmetry occurs.

Nowadays ceramic piezoelectric materials are the most popular piezo-materials, produced

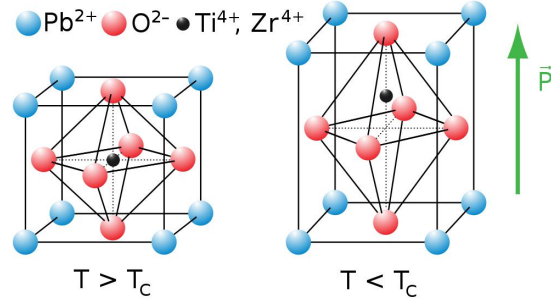


Figure 2.15: Crystalline structure of ceramic PZT below and above Curie temperature [66].

with well-established manufacturing methods and having high piezoelectric coefficients, even up to 500 P_c N-1 in the case of lead zirconium titanate (PZT) [67]. However, some limitations such as the toxicity of some constituent elements (e.g., lead), high production costs, mechanical fragility, and biocompatibility, occur in the use of this class of piezo materials.

Starting from 1969 with the discovery of piezoelectric effects in the synthetic polymer PVDF, different research groups began exploring organic piezoelectric materials, such as polymers, that would overcome some of the limitations of piezo ceramics. Even if the piezoelectric coefficients of polymers are smaller than the ceramic ones, they show high mechanical flexibility, have a relative low elastic modulus, polymer-based devices are less expensive both in terms of material cost that of fabrication technology, and in addition, they can be shaped and produced at lower temperatures and in customized shapes depending on the use. The piezoelectric behavior is not only observed in the well-known ferroelectric polymer PVDF, but also in some polyamides, polypeptides, polyesters and polyureas.

Despite the great number of advantages, polymers have a less pronounced piezoelectric response with respect to ceramic materials. Nanocomposite materials are introduced to overcome this limitation. By incorporating inorganic piezoelectric materials into a polymer matrix, the combination of the characteristic properties of ceramic and polymeric materials are obtained, i.e., a structure with a high piezoelectric coefficient, even if lower than those of ceramic materials, and intrinsically flexible.

As well as piezoelectricity, some piezoelectric materials like PVDF or PZT, can exhibit pyroelectricity or ferroelectricity or both simultaneously (figure 2.16).

Pyroelectricity is the electrical response of a material to a change in temperature (article pyroelectricity). Pyroelectric effect is present in all the materials that exhibit a net polarization or dipole moment per unit volume under non-distortion conditions. The pyroelectric coefficient p relates the change in the polarization state of the material (dP) to a change in temperature (dT), in absence of an external electric field. So, p is expressed as (equation 2.8):

$$p = dP/dT \quad (2.8)$$

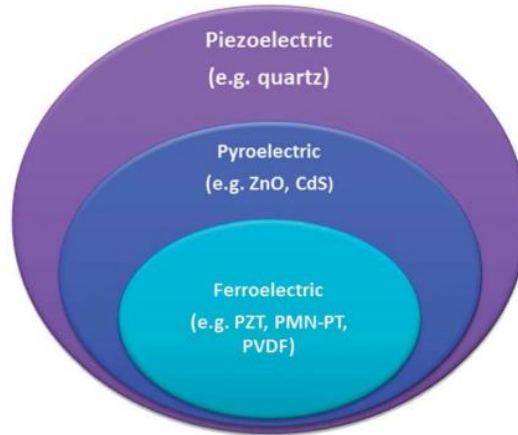


Figure 2.16: Diagram of the division of piezoelectric materials [68].

As said before, all non-centrosymmetric polar crystals are piezoelectric, but not all piezoelectric show a net dipole moment at rest. So, not all piezoelectric materials are also pyroelectric. Often, the pyroelectric effect is a disturb in piezoelectric applications that must be eliminated. It is possible to eliminate the pyroelectric response of the material with different strategies like using filtering of the electrical signal or by using an appropriate device design [67].

There is a class of materials among piezoelectric, which are characterized by the presence of spontaneous electrical polarization even in the absence of electric field applied. This property belongs to ferroelectric materials, among which there are also polymeric ones such as the PVDF. To be ferroelectric a material must have a spontaneous polarization and therefore, in the case of crystals, it must not have centers of symmetry. These materials are polarized with the application of an electric field and maintain polarization even after the field is switched off.

Ceramic polycrystalline materials are composed by different domains, called Weiss do-

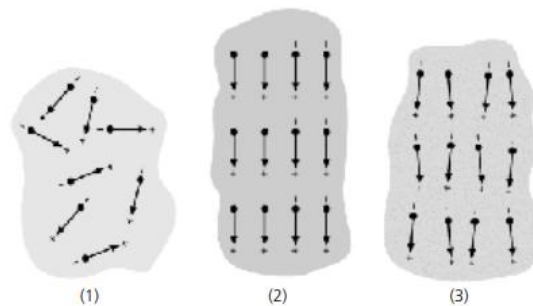


Figure 2.17: Electric dipoles in Weiss domains: (1) unpoled ferroelectric ceramic, (2) during poling, (3) after poling (piezoelectric ceramic) [69].

mains (figure 2.17). Randomly oriented micro domains cancel each other out resulting in a null net polarity. To obtain a piezoelectric response is necessary to align dipoles in a preferential direction to obtain a non-null net polarity. The dipole moments alignment is necessary to remove the center of symmetry, essential condition to obtain piezoelectric behavior. With the application of a strong electric field at temperatures above the Curie one, typical of each material, dipoles can be all oriented in a preferential direction. This is known as pooling process, only possible in ferroelectric materials, since only in these materials is there a spontaneous, remnant polarization which can be switched by a suitably large electric field. A typical ferroelectric sample response in the cyclic poling process is shown in figure 2.18 and known as hysteresis loop. One very important characteristic of ferroelectric materials is polarization reversal by an electric field. One consequence of the domain-wall switching in ferroelectric materials due to an applied electric field, is the occurrence of the ferroelectric hysteresis loop.

In figure 2.18, it is possible to see that as the field is increased from a zero value, all the

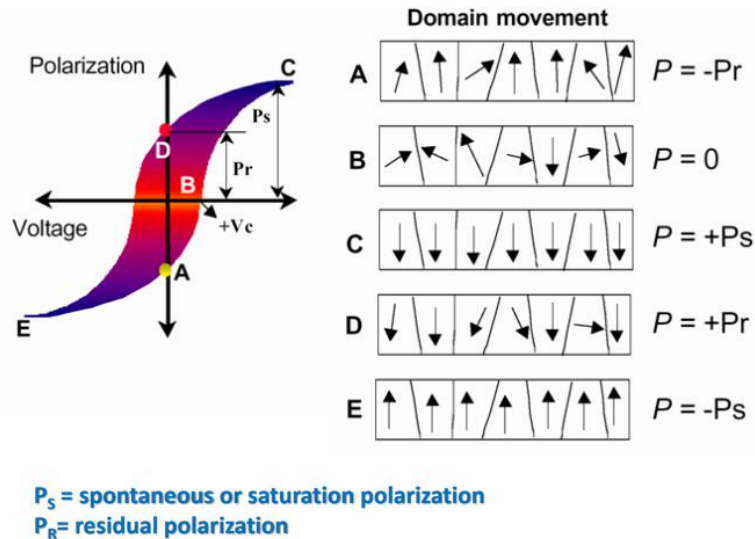


Figure 2.18: Representation of the theoretical hysteresis loop [68].

polarization domains in a random position start to switch in the field direction (BC region). The polarization response in the BC region is strongly nonlinear. When the domains are all aligned the ferroelectricity behaves again linearly. If the field strength starts to decrease from point C, some domains will back-switch, but at zero field the polarization is not equal to zero. This value of polarization at zero field is called the residual polarization, PR. If you want to reach again the condition of null polarization, the field must be reversed. This field, necessary to bring the polarization to zero, is called the coercive field, EC [68].

2.3.1 PVDF

Poly(vinylidene fluoride), known as PVDF is the first piezoelectric polymer discovered in 1969 and it is still used and studied today by numerous research groups for its excellent piezo-, pyro- and ferro-electric properties. PVDF is one of the most attractive piezo-polymer due to its flexibility, transparency, lightweight, high chemical resistance due to the presence of C-F bonds, good resistance to mechanical deformation, biocompatibility, high thermal stability, low cost, and durability in the human body. The use of PVDF in healthcare applications become very relevant since PVDF is stable under the gamma radiation and in the biomedical field, instruments are often sterilized through the use of this radiation [73]. PVDF exhibits five different polymorphs identified as α , β , γ , δ and ϵ . These five phases can be divided in polar and non-polar: α and ϵ are non-polar, while β , γ and δ are polar. To generate piezoelectric properties, PVDF must be in one of the polar phases.

As it is possible to notice, the high difference in the electronegativity of fluorine atoms

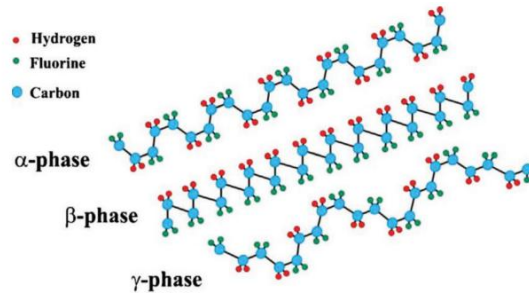


Figure 2.19: Representation of the α , β , γ -phases of the PVDF polymer chain. Reprinted from [77], Copyright (2014), with permission from Elsevier.

than carbon and hydrogen atoms bring to excellent piezoelectric properties. The crystalline phases differ depending on the type of trans (T) and gauche (G) connection in the various conformations of the polymer chain, the α and δ (TG \overline{T} G \overline{T}), the β (TTTT) and finally the γ (TTTGT \overline{T} TG \overline{T}). In particular, the α -phase is non-polar because chains are packed into the unit cell in such a way that the molecular dipoles are antiparallel. While the β -phase is the one that shows the best piezoelectric property, since dipoles are all parallel to each other, producing the highest dipole moment per unit cell.

So, the piezoelectric response of PVDF is enhanced only increasing the content of the β crystalline phase inside the piezoelectric material. To do that, it is necessary to re-orient monomers, in order to rotate molecular dipoles in the same direction. This operation of ‘polarization’ is costly and requires either mechanical stretching or high voltage application, as shown in figure 2.20. Electrospinning is an excellent technique that produces PVDF nanofibers with a high β phase fraction due to the simultaneous effect of high voltage poling and mechanical stretching during the PVDF nanofiber deposition. Electrospinning is a very simple deposition method and economically viable, with optimal electrospinning parameters a high β -phase content can be obtained.

PVDF can exist under different forms and its piezoelectric property related to its β phase

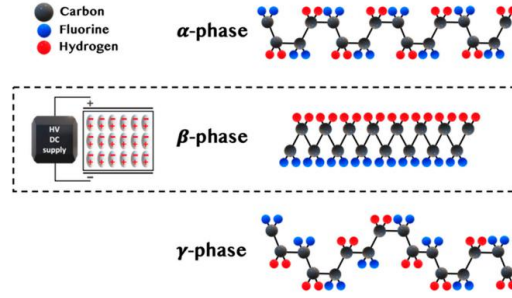


Figure 2.20: β -PVDF induced by stretching pr high poling voltage [74].

content makes it interesting for energy harvesters [75] and wearable applications[78]. In the next section of this work, the influence of the electrospinning parameters to enhance the piezoelectric properties of PVDF nanofibers are described. The piezoelectric response of PVDF is related the β phase content or fraction of β phase inside the material, and can be measured by equation 2.9:

$$F(\beta) = \frac{X_{\beta}}{X_{\beta} + X_{\alpha}} \cdot 100\% \quad (2.9)$$

where X_{α} and X_{β} are the degrees of the PVDF α and β phases. However, the content of the β phase in PVDF is also related to the degree of crystallization (X_c). The crystallinity is expressed by equation 2.10:

$$X_c = \frac{\Delta H}{\Delta H_m \phi} \cdot 100\% \quad (2.10)$$

where ΔH is the fusion enthalpy of the PVDF samples, ΔH_m is the fusion enthalpy of PVDF with 100% crystallinity, ϕ is the PVDF weight fraction in PVDF nanofibers or membranes[79].

Chapter 3

The electrospinning process

3.1 Electrospinning

Electrospinning, electrostatic spinning, is an electrostatic fiber fabrication technique that gains very high attention in recent years due to its versatility in spinning a large variety of polymeric fibers but also since can produce fibers with diameters ranging from 2nm to several micrometers. Electrospun nanofibers start to be applied successfully in various fields, such as, biotechnology and biomedical [80], environmental engineering [81], optical electronics [82], protective clothing [83], tissue engineering scaffolds [84] and many others. Electrospinning is a very efficient and simple technique to produce nanofibers. It simply consists of using a high voltage electric field to produce electrically charged jets from polymer solution or melts, that thanks to the solvent evaporation produces nanofibers. The very high charged nanofibers are directed from the spinneret towards the oppositely charged collector, which can be of different types, the simplest one is the flat surface, but it can be for example also a rotating drum, to collect the fibers. In electrospinning, the spinning of fibers is particularly due to tensile forces in the axial direction of the flow of the polymer solution thanks to the induced charges in the presence of the electric field.

3.2 Hystory of electrospinning

Electrospinning is an old technique. The first studies about electrospinning date back to 1914, when Zeleny, a physicist working at the University of Minnesota, describes this process in the literature.

After that, Anton Formhals made significant contributions to the development of the electrospinning process [85]. In 1934, Formhals patented his first apparatus to produce fibers, but this first method had some difficulties in drying completely the fibers after the spinning due to the short distance between the spinning and the collection zone. Subsequently in 1940, Formhals patented another method to overcome previous problems and produces composite fiber webs from multiple polymer and fiber substrate by electrostatically spinning polymer fibers on a moving base substrate [86].

From 1964 to 1969, Sir Geoffrey Ingram Taylor, made another contribution to this process,

he tried to explain with a mathematical model, the shape of the cone formed by the electrospun fluid under the influence of an electric field. Thanks to him, it is possible to talk about the “Taylor cone”, the characteristic fluid droplet shape. Thanks to the examination of different viscous fluids, Taylor was able to determine the angle necessary for the polymer to balance the surface tension with the electrostatic forces.

After the Taylor contribution, a great number of different physicians have tried to gain more and more insight into the spinning process. Among these researchers the Baumgarten contribution in 1971 is noteworthy, because he was able to build a method of photographing electrospun fibers in flight and thanks to it, he investigated the effects of the viscosity of the solution, of the voltage, of the surrounding gas, obtaining at the end fibers with diameters less than one micrometer.

Over the past 20 years, it has been possible to acquire a very detailed understanding of this technique thanks to the studies about the influence of solution parameters, like viscosity and conductivity, process parameters like distance between the two electrodes, voltage and feed rate and external parameters like humidity and temperature of deposition.

3.3 The electrospinning process

The process consists in the application of a huge electric field on a polymeric fluid. The simplest and more typical setup is shown in figure 3.1, where it is possible to see both the horizontal and the vertical one.

As it is possible to see in figure 3.1, an electrospinning system is composed by a capillary tube, a needle attached to a syringe filled with polymer solution, a grounded collector screen, and a high voltage power supply connected between the capillary and the collector. Nanofibers can be collected directly on the grounded electrode or on a specific substrate, depending on the specific application. The high voltage source is needed in order to inject charge of a certain polarity in the polymer solution in order to be accelerated from the spinneret towards the collector of opposite polarity. So, the electric field is simply given by the ratio between the applied voltage (typically from 1 to 30 kV) and the working distance. Most of the polymers are dissolved in some solvents, like PEO in H₂O [88], and when the solution is ready, it’s introduced into the capillary tube connected to the syringe. When the solution is expelled from the spinneret, the solvents evaporate and this can produce unpleasant or even harmful smells, so the process is driven inside a chamber with a ventilation system.

As said before, the strong electrostatic field brings to the formation of the droplet from the capillary end to undergo deformation into the shape known as “Taylor cone”[89].

As showed in figure 3.2, the behavior of the jet can be divided into three regions: the formation of the Taylor cone, the straight jet region, and the unstable whipping jet region. The conical shape assumed in the first region by the jet is due to the interaction of the surface tension of the solution, the electric charges developed in the solution and the electrostatic forces acting on it [90]. By increasing the applied potential, a charged jet starts to come out of the tip of the cone when the electrostatic force has overcome the surface tension of the solution (figure 3.3). The jet, after a straight path, becomes unstable. This instability is known as “whipping instability” that produces a “whipping motion” of the jet due to the charge repulsion that occurs between the excess charges present in the jet. The

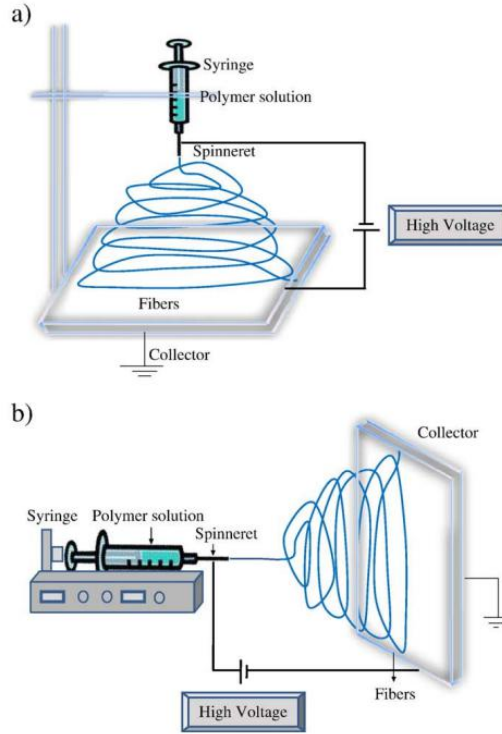


Figure 3.1: Schematic representation of the planar vertical (a) and horizontal (b) electrospinning set up. Reprinted from [87], Copyright (2010), with permission from Elsevier.

primary jet is divided in multiple sub jets with smaller and smaller diameters as shown in figure 3.4. In literature this progressive reduction of the fiber diameter is defined by the following equation [21]:

$$r_0^3 = \frac{4\epsilon m_0}{k\pi\sigma\rho} \quad (3.1)$$

Where m_0 is the mass flow rate (g/s) when r_0 (cm) is calculated, ϵ is the fluid permittivity (C/V cm), k is a dimensionless parameter related with the electric currents, σ is the electric conductivity (A/V cm) and ρ is the electrospun material density (g/cm^3).

If the fluid has a low molecular weight the jet becomes unstable before reaching the collector and turns into a spray of small electrostatically charged drops. This process is called electrospaying [91]. Using fluid polymers instead, viscoelastic forces stabilize the jet allowing the formation of very fine loaded filaments.

During the path of the jet from the spinneret to the collector, the solvents evaporate, and the network of nanofibers deposited on the collector is composed of a single nanofiber that is arranged on it in a completely random way. Any residual charges present on the nanofiber are discharged upon contact with the collector (connected to the grounding) and the nanofiber membrane can be detached from the collector. Ideally, no trace of solvent should remain when the jet touches the collector, otherwise the newly formed polymer

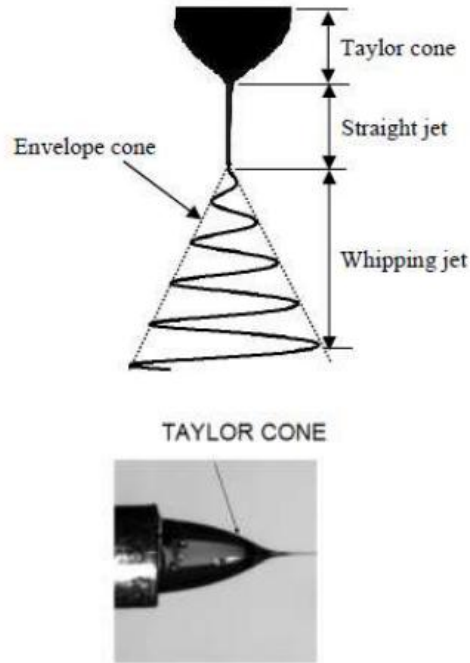


Figure 3.2: Behavior of the jet during the electrospinning process [89].

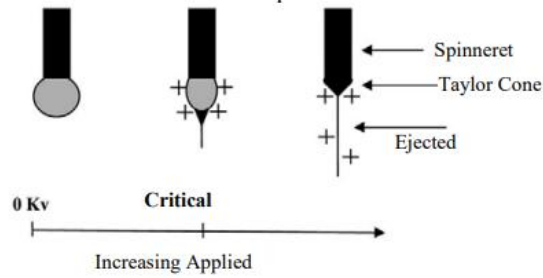


Figure 3.3: Taylor cone formation with increasing applied voltages [90].

nanofibers are dissolved again in the residual solvent. The evaporation rate of the solvent depends on several factors, including for example the distance from the collector and the vapor pressure of the solvent. Usually, even if all the spinning values are kept constant, in the deposited nanofibers the diameters distribution is not homogeneous during the electrospinning process.

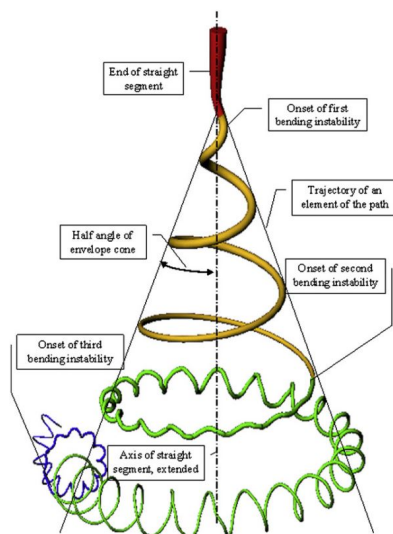


Figure 3.4: Instabilities of the jet with progressive reduction of diameter [21]. Reprinted from [108], Copyright (2008), with permission from Elsevier.

3.4 Effects of various parameters on electrospinning

To better understand the electrospinning process, it is fundamental the analysis of all the process parameters which influences the properties of the deposited fibers. These parameters are divided in three large families: solution parameters, processing parameters, and ambient parameters.

3.4.1 Solution parameters

Concentration

Solution concentration is an important parameter that establishes the limiting boundaries for the formation of electrospun fibers due to the variation in the surface tension and viscosity [92]. When a solid polymer is dissolved in a solvent, like what happens in the preparation of the electrospun solution, the solution viscosity is directly proportional to the polymer concentration.

Solution surface tension and viscosity are two important parameters in determining a sort of window of spinnability, a range of concentrations in which continuous fibers can be obtained in the process. At low concentration, so low viscosities, the surface tension is dominant, so instead of fibers the formation of drops will occur, electrospray instead of electrospinning. At high concentrations, the viscosity is so high that the fiber formation is not allowed by an inability to control and maintain the flow of the polymer between the spinneret and the collector. So finally, only a range of concentrations can produce fibers and this range is dependent on the polymer/solvent system used. At low solution concentrations, a mixture of fibers and beads are obtained. As the concentration increases, the shape of the bead

changes from spherical to spindle-like. This variation in the morphology is studied by Fong in his work [93] and figure 3.5 shows the structure of PEO nanofibers obtained by the variation of the solution concentration between 1wt.% and 4wt.% PEO concentration. Even if concentrations are inside the processing window, varying solution concentration an alteration of the morphology and of the diameter of the nanofibers occurs. Higher viscosity, so a higher polymer concentration will result in larger nanofiber diameters.

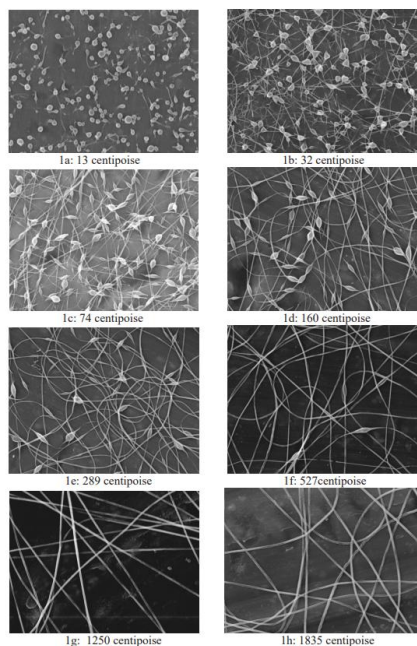


Figure 3.5: SEM image showing the morphology of fibers increasing the solution concentration. Electric field is 0.7 kV/cm. Reprinted from [93], Copyright (199), with permission from Elsevier.

Molecular weight

Molecular weight is another important parameter that influence the electrospun nanofibers properties such as viscosity, surface tension, conductivity, and dielectric strength. Molecular weight is linked to the entanglement of polymer chains in solutions, thus the solution viscosity, the higher the molecular weight of the polymer, the greater the viscosity of the solution [94]. A condition necessary for the fiber formation and deposition is that the solution has a sufficient viscosity to avoid the formation of drops. Entanglements between polymeric chains are fundamental to keep the jet cohesive and to prevent it from breaking giving rise to the formation of drops of solution. The number of entanglements is closely related to the length of polymer chains, which is directly proportional to the molecular weight of the polymer in solution. Obviously not only the high molecular weight helps to obtain a sufficiently viscous solution, because as said before, also the concentration plays an

important role. So, if the concentration is fixed, a polymer with too low molecular weight leads to the formation of beads rather than fibers.

It has been observed by McKee et al. [95] that high molecular weights are not always necessary to produce nanofiber with the electrospinning process. It was seen that sufficient intermolecular interactions can provide a substitute for the interchain connectivity obtained through chain entanglements, and using this principle, researchers have prepared oligomer-sized phospholipids from lecithin solutions into nonwoven membranes through electrospinning.

Solution viscosity

Solution viscosity is very important in determining the fiber size and morphology. As said before, viscosity, polymer concentration and polymeric molecular weight are related to each other and in general different polymers brings to different ranges of values of these three parameters to have a good fiber deposition.

To have good electrospun fibers, optimal solution viscosity is required because very low viscosity leads to no fiber formation and very high viscosity results in a difficult ejection of jets from polymer solution. The formation mat of nanofibers mat starting from an electrospun polymeric solution is possible only if the viscosity of the solution is into the following range [21]:

$$(0.02 \leq \eta \leq 300)Pas \tag{3.2}$$

Inside the range of viscosity values that allows a good fiber deposition, an increase in solution viscosity or concentration brings to a larger and more uniform fiber diameter. Indeed, if the solution viscosity is too low the surface tension is greater than the viscoelastic forces and instead of having the fiber formation, the ejection of droplets occurs (electrospray). While, if the solution viscosity is too high and the solution will be harder to stretch due to the more robust macromolecular chain entanglement at the same voltage.

Surface tension

Surface tension is function of the solution composition and plays a very important role in the electrospinning process [96]. When the polymeric solution is charged under the effect of the electric field, to start the electrospinning process and the deposition of the fiber, is necessary that the charged solution wins its surface tension.

If the solution is slightly viscous, they are few interactions between solvents molecules and polymeric chains; so, a great number of solvent molecules are free, and they agglomerate under the effect of the surface tension. Obviously, for more viscous solutions is not the same because interactions between solvents and polymer are strong. During the electrospinning process a strong electric field is applied, the solution is stretched, and solvent molecules are distributed along the polymeric chains. This effect reduces the tendency of solvent molecule to agglomerate under the effect of the surface tension.

So, a lower surface tension of the electrospinned solution helps electrospinning to occur at a lower electric field. On the contrary, if the surface tension of the solution is high the electrospinning process is inhibited because of the jet instability and the generation of

droplets. To reduce surface tension, one possibility is to choose solvents with a low surface tension.

Conductivity

As it is said before, during the electrospinning process a strong electric field is applied to the solution to stretch it under the repulsion between charges on its surface. A greater conductivity corresponds to a greater amount of charge in the jet and so, the solution stretching is more evident and there is a significant decrease in the diameter of the electrospun nanofibers. On the contrary, if the solution conductivity is reduced there will be an insufficient elongation of the jet to produce uniform fiber and beads may be observed [96]. So, higher conductivity of the solution results in the formation of thinner and more uniform fibers even if a too strong electric field can bring to a strong instability of the jet. Solution conductivity is mainly determined by the polymer type, solvent used, and the availability of ionizable salts. So, one possibility to increase the conductivity is to add a small amount of salt, that increases the uniformity of fibers and a decrease in beads generation.

3.4.2 Processing parameters

Applied voltage

The applied voltage is an important parameter in the electrospinning process. There is a threshold voltage that must be exceeded in order to have the ejection of the jet from the Taylor cone. So, when the threshold voltage is reached, the fiber formation occurs and so the electrospinning deposition can start. Obviously, this threshold voltage depends on the polymer solution used in the electrospinning process. With the increase of the applied voltage, the solvent evaporation is enhanced and the diameter of the deposited nanofibers is strongly reduced, due to the increasing stretching of the nanofiber thanks to the greater coulombic forces in the jet as well as a stronger electric field.

If the applied voltage is increased beyond a critical value, the formation of beads or beaded nanofibers occurs. This is attributed to the reduction of the size of the Taylor cone and to an increase of the jet velocity, and so instabilities, for the same flow rate.

For example, in the work of Sener et al. [97] electrospinning of a solution containing PVA (Polyvinylalcohol) and SA (sodium alginate) was performed by applying variable voltages at 28, 35, 40 and 45 kV. In this work it's showed that fibers obtained at 45 kV had bigger beads comparing to the other fibers and fibers obtained at 28 kV are broken. Only fibers obtained at 35, 40 and 45 kV are continuous.

Tip to collector distance

Tip to collector distance is a crucial parameter that determines the morphology of the deposited nanofibers. Specifically, it exists an optimum distance that favors the formation of uniform and not beaded nanofiber. Indeed, increasing the tip to collector distance, nanofibers have enough time to stretch and solvents enough time to evaporate bringing to the deposition of more uniform nanofibers. Various researchers show that large-diameter nanofibers with a huge number of defects are formed when the distance is kept small,

whereas the diameter of the nanofiber decreased as the distance was increased.

In the work of Gade, Harshal, et al. [106] it is studied the effect of the variation of the

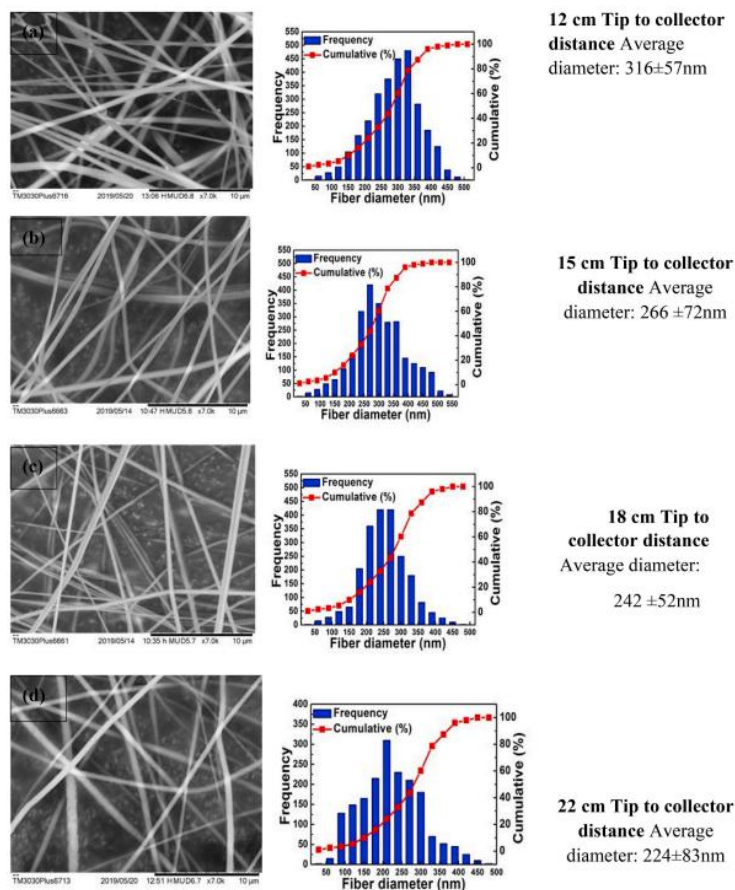


Figure 3.6: SEM images and fiber size distribution of PVDF nanofibers with increasing tip to collector distance. Reprinted from [106], Copyright (2021), with permission from Elsevier.

spinning distance on the morphology and fiber size of a solution of acetone:DMF (1:1 by weight) with PVDF, with concentration of 10% by weight. The electrospinning process is performed with the deposition of the solution on a cylindrical drum collector with a rotation speed of 30 rpm, applying a voltage of 27 kV, flow rate of 5ml/h and varying the tip to collector distance from 12 to 22 cm. From this work (figure 3.6) it is possible to see that shorter distances result in larger fiber diameters and due to surface tension forces, larger fibers tend to attenuate bead formation. If the distance is increased, the stretching of the fiber is increased too, bringing to a reduction of their diameter.

Types of collectors

Using a simple planar plate as collector, nanofibers are deposited as a random mass due to the bending instability of the highly charged jet. They exist also other types of collectors such as cylinders or discs, tips, counter electrodes composed by two bars and many others [98].

Many research groups demonstrate the possibility to have an increase in the alignment

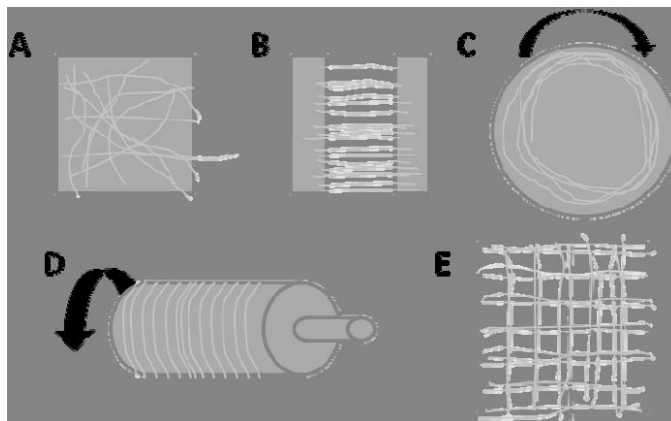


Figure 3.7: Different types of collectors for electrospinning: (A) static plate, (B) parallel electrodes, (C) rotating disk, (D) rotating drum, (E) grid [98].

of nanofibers because of the use of a rotating drum collector. Using this type of collector electrospun nanofibers are deposited more or less parallel to each other. In addition, it is possible to vary the rotation speed of the drum collector and increasing this speed the fiber alignment is increased and the fiber diameter is slightly decreased. So, the rotation is an important parameter that influence the alignment and the stretching of nanofibers, that for example can influence the presence of β -phase [99], linked to the piezoelectricity of PVDF, in the electrospun PVDF solution.

Flow rate

The flow rate of the polymeric solution has a great influence on the morphology of the deposited nanofibers [100]. A critical value of the flow rate, varying from polymer-to-polymer solution, is observed in order to have uniform and beadless electrospun nanofibers. Increasing the flow rate results in an increase in the average fiber diameter, due to a decrease in the stretch of an electrospinning jet in the flight between the needle and the metallic collector. Beads are observed at either low or higher flow rates, inducing a loss of fiber uniformity. This happens because, when the flow rate is too high, the solvent is not able to evaporate before fiber deposition and this causes a reduction of fiber stretching and beads formation.

3.4.3 Ambient parameters

It is demonstrated that apart from solution and processing parameters, also ambient parameters, like temperature and humidity [101] [102], play a crucial role in the properties of the deposited nanofibers. Indeed, there is an inverse relationship between the solution viscosity and temperature. Increasing temperature, the fiber diameter is reduced probably due to a decrease in the solution viscosity with the increase of temperature, so, the solution will be harder to stretch. On the other hand, at very low humidity conditions the evaporation of the solvent is faster, and a volatile solvent can dry rapidly. In some cases when the RH reaches a critical value, the water in the environment completely inhibits the evaporation of the solvent, which makes the electrospinning process difficult.

3.5 Synthesis of polymer/CNTs nanocomposite fibers by electrospinning

Polymer/CNTs nanocomposite fibers synthesized by electrospinning, offers the possibility to simultaneously align CNTs along a single axis without affecting the structural integrity of the individual CNTs [71]. Like previously said (section 3.3), during the electrospinning process the behavior of the jet expelled from the spinneret can be divided in three regions, where the first one as a conical shape known as Taylor cone. This cone gives rise to a converging flow and therefore, the jet and hence fibers emanate from an extremely narrow region. This concentration of streamlines in an extremely narrow region brings CNTs to align along the fiber axis and the large longitudinal strain rate due to the application of a certain voltage between the spinneret and the counter electrode ensues in the CNT alignment within the fiber direction. From the work of Kim, G-M., G. H. Michler, and P. Pötschke [103], figure 3.8 shows a TEM (Transmission Electron Microscopy) image of MWCNT embedded in a PEO matrix, demonstrating the orientation of CNTs along the fiber axis.

Some researchers have tried to explain in a mathematical way the behavior of composite

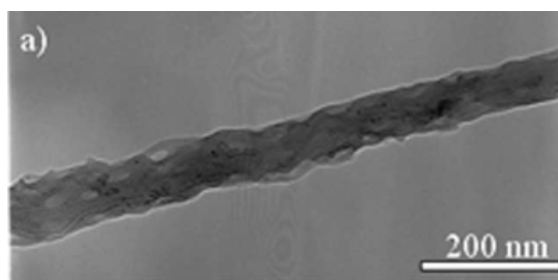


Figure 3.8: TEM image of CNTs oriented along the polymer composite nanofiber direction. Reprinted from [103], Copyright (2005), with permission from Elsevier.

nanofibers. Dror et al. [72] suggest that the convergence of the polymeric jet flow is the

reason of CNTs alignment into the fiber direction and were able to demonstrate it mathematically representing the converging liquid flow of an electrospinning solution toward the vertex of the Taylor cone in polar coordinates (figure 3.9).

Moreover, the alignment of CNTs within the fiber direction enhance the dispersion of

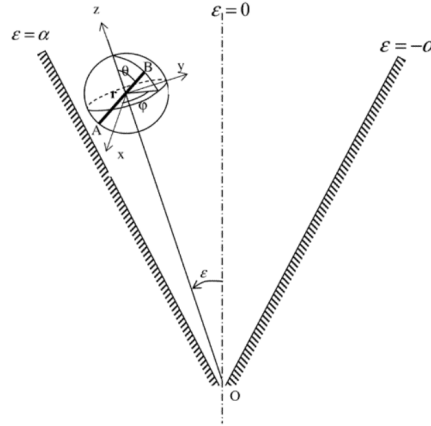


Figure 3.9: Schematic representation of the flow of an electrospinned solution in polar coordinates. Reprinted with permission from [72], Copyright (2003) American Chemical Society

CNTs facilitating the formation of suitable networks and this bring to the establishment of percolation for lower filler concentrations inside the polymer matrix. This is a big advantage in the realization of piezoresistive sensors because by using a very little weight percentage of conductive filler inside the polymer matrix, the composite nanofiber mat by electrospinning bring to a strong electrical resistance variation if a stress is applied on it. In addition, in the work of Massaglia Giulia et al. [46], a significant increase of the electrical conductivity was observed when the electrospinning working voltage during PEO/MWCNT nanofiber deposition was increased. Thanks to a FESEM analysis, it was demonstrated that this behavior is due to a denser nanofiber/nets structure, demonstrating the possibility to tune the electrical behavior of conductive composite nanofibers simply by changing the applied voltage. This is evidence of the fact that electrospinning parameters used for the composite nanofiber deposition influence also its the electrical behavior.

For all these reasons together with the low cost and relatively simple process involved, electrospinning is becoming an excellent technique to embed CNTs within nanometer sized polymer fibers also for the realization of piezoresistive flexible sensors.

3.6 Influence of electrospinning parameters on β -phase of PVDF

The electrospinning process description is well presented in the second chapter of this thesis. However, now a brief description of how electrospinning parameters influence the

formation of the β -phase during the PVDF deposition, is shown. This is important to understand how it is possible to enhance piezoelectric properties of the PVDF nanofiber mat deposited, linked to the presence of the β -phase inside the sample.

The β -phase formation in the electrospun PVDF nanofibers is principally influenced by:

- The nanofiber stretching, so the reduction of the nanofiber diameter.
- The ease with which the solvent evaporates.
- The increase of the nanofiber alignment.

Nanofiber stretching and solvent evaporation depends on different electrospinning parameters like applied voltage, spin distance, flow rate, PVDF concentration in the solution, rate of humidity, electrospinning time and DMF/acetone ratio.

3.6.1 Influence of electrospinning parameters on PVDF piezoelectric behavior

Effect of applied voltage on PVDF β -phase

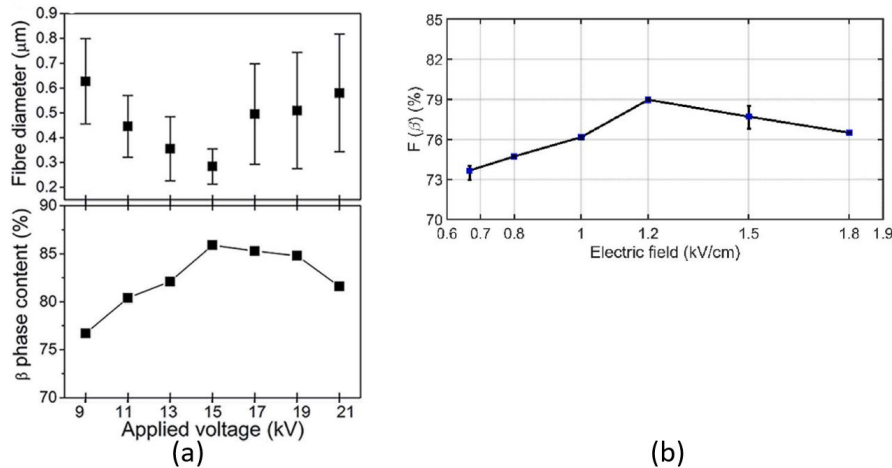


Figure 3.10: Influence of the applied voltage on the β phase fraction of electrospun PVDF. (a) work of Shao, Hao, et al. Republished with permission of Royal Society of Chemistry, from[104]; permission conveyed through Copyright Clearance Center. (b) work of Singh. Reprinted from [105], Copyright (2021), with permission from Elsevier.

The average fiber diameter decreases with increasing applied voltage. This is due to the stretching of the polymer jet under high applied voltages, that orients the PVDF molecular chains dipoles, allowing the α -to- β crystalline phase changes. However, if the spin distance is maintained constant and the voltage is increased too much, so the electric field is too high, the jet takes less time to get the collector. So, fibers are deposited before polymer

molecules can be aligned and solvent completely evaporates. As a result, the reduction of β -phase fraction occurs.

In the work of Shao, Hao, et al. [104] a PVDF solution was electrospun with an applied voltage set in the range 9-21 kV. What it is obtained is shown in figure 3.10(a), demonstrating that it exists an optimal value of voltage to obtain the maximum fiber stretching and so the maximum β -phase fraction. Moreover, it is evident that increasing the applied voltage below a certain value, the fiber diameter is reduced but the fraction of β -phase is increased. However, if the applied voltage becomes too high, the diameter of nanofibers is increased bringing to a reduction of the β -phase fraction. The same concept is shown in the work of Singh [105], where the electric voltage is made to vary between 10 kV and 27 kV with the spin distance set at 15 cm. So, the electric field is computed to be between 0.67 kV/cm and 1.8 kV/cm (3.10(b)).

Influence of spin distance on PVDF β -phase

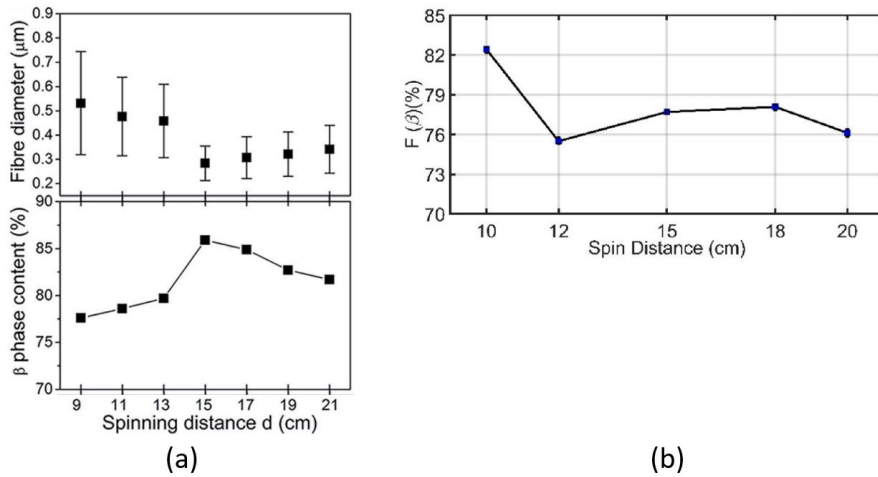


Figure 3.11: Influence of the spinning distance on the β phase fraction of electrospun PVDF. (a) work of Shao, Hao, et al. Republished with permission of Royal Society of Chemistry, from [104]; permission conveyed through Copyright Clearance Center. (b) work of Singh. Reprinted from [105], Copyright (2021), with permission from Elsevier.

With the increase of the spin distance, nanofibers have enough time to stretch, and solvents have enough time to evaporate, which bring to the reduction of the deposited fibers diameter and so, to the formation of the β -phase. On the other hand, with the increase of the spin distance, the electric field intensity decreases at the same voltage, and the jet instabilities increases, which is harmful for the formation of β -phase.

In the work of Shao, Hao, et al. [104] the PVDF electrospinning was conducted at constant applied voltage of 15 kV, while the spinning distance is changed from 9 cm to 21 cm (figure 3.11(a)). While in the work of Singh [105], the spin distance is made to vary between 10 cm and 20 cm at fixed value of the voltage applied (figure 3.11(b)). As it was expected, in both

cases it exists an optimal spinning distance value at fixed applied voltage, to maximize the β -phase fraction.

Influence of flow rate on PVDF β -phase

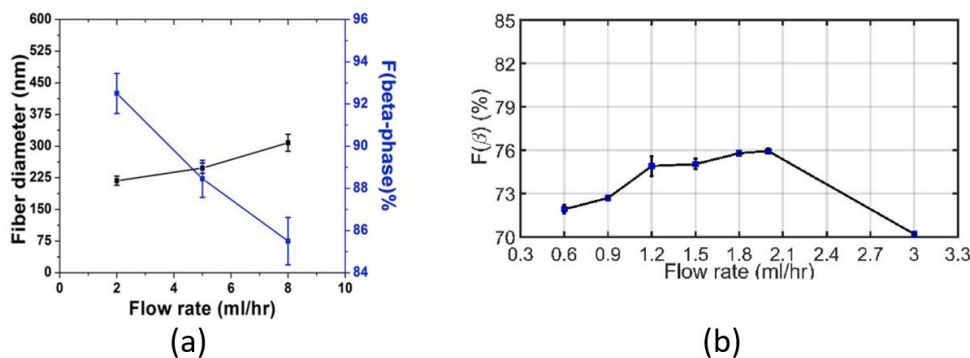


Figure 3.12: Influence of flow rate on the β phase fraction of electrospun PVDF. (a) work of Gade, Harshal, et al. Reprinted from [106], Copyright (2021), with permission from Elsevier., (b) work of Singh. Reprinted from [105], Copyright (2021), with permission from Elsevier.

Increasing the flow rate results in an increase in the average fiber diameter, due to a decrease in the stretch of the electrospinning jet. Initially increasing the flow rate brings to an increase of the β -phase fraction, but if it is too high the solvent does not evaporate before fiber deposition and this causes a reduction of fiber stretching, so a reduction of the β -phase content. In different publications, researchers have denoted that the fraction of β -phase increases until a critical value of the flow rate and then decreases.

In the work of Gade, Harshal, et al. [106] the PVDF electrospinning was conducted varying the flow rate from 2 to 8 ml/hr (figure 3.12 (a)). It is possible to notice that the flow rate increase corresponds to an increase of the fiber diameter but to a decrease of the fraction of β -phase. While in the work of Singh [105], the flow rate is varied from 0.6 to 3 ml/hr (figure 3.12(b)). In this case, it was found an optimal value of the flow rate to obtain a maximum β -phase content.

Influence of DMF/ACETONE ratio on PVDF β -phase

Usually the electrospinning solution used in different works and also in this thesis, utilizes PVDF mixed in acetone and DMF (N,N-Dimethylformamide) solvents in different ratios. If the acetone concentration is too low with respect to DMF concentration, the vapor pressure of the solution decreases because vapor pressure of acetone is greater than the DMF one. This increases interactions between polymer and solvent mixture and limits the solvent evaporation and so the nanofiber stretching during the deposition. Consequently, the fraction of β -phase is reduced. On the other hand, if the acetone concentration is too high, the solution become too dry and cannot come out from the needle [107].

Influence of polymer concentration on PVDF β -phase

The PVDF concentration in the solution influences the solution viscosity. Viscosity, in turn, influences the nanofiber stretching and so the β -phase fraction. Indeed, when the concentration of PVDF in the solution increases, the solution viscosity increases, therefore resulting in more uniform nanofibers with a higher β -phase content. Further increase of the PVDF concentration will increase the solution viscosity too much, and the solution will be harder to stretch due to the more robust macromolecular chain entanglement at the same voltage. So, this brings to a β -phase fraction reduction.

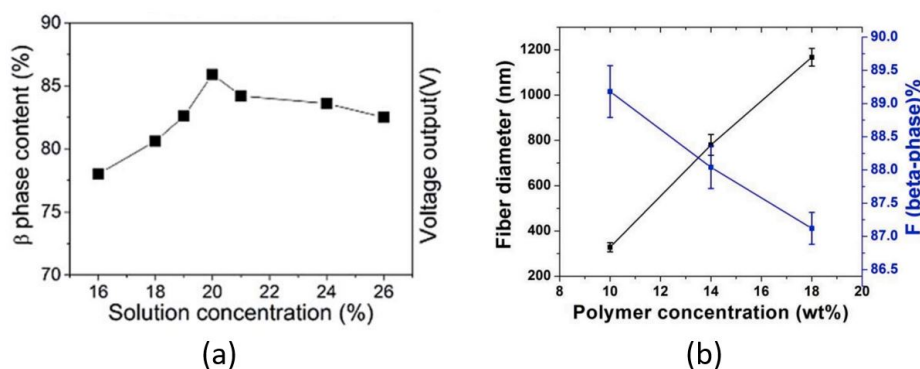


Figure 3.13: Influence of the PVDF concentration inside the polymeric solution on the β phase fraction of electrospun PVDF. (a) work of Shao, Hao, et al. Republished with permission of Royal Society of Chemistry, from [104]; permission conveyed through Copyright Clearance Center. (b) work of Gade, Harshal, et al. Reprinted from [106], Copyright (2021), with permission from Elsevier.

In the work of Shao, Hao, et al. [104], the PVDF electrospinning was conducted varying the polymer concentration from 16 to 26 wt% (figure 3.13(a)) with applied voltage 15 kV, spinning distance 15 cm and a nanofiber mat thickness of 70 μ m. It is possible to notice that the optimal value of the polymer concentration to obtain the higher maximum β -phase fraction is 20 wt%. While in the work Gade, Harshal, et al. [106], the polymer concentration was varied from 10 to 18 wt% (figure 3.13(b)). In this case it is underlined the opposite trend of fiber diameter and fraction of β -phase increasing the concentration of PVDF inside the solution.

Influence of RH concentration on PVDF β -phase

Compared to dry environments, the PVDF nanofiber deposited in a more humid environment have a higher β -phase fraction [107]. To obtain a higher β -phase content, the electrospinning is usually carried out under high RH. However, it should be considered that when RH is too high and reaches a critical value, water in the environment completely inhibits the evaporation of the solvent, which makes the electrospinning process difficult.

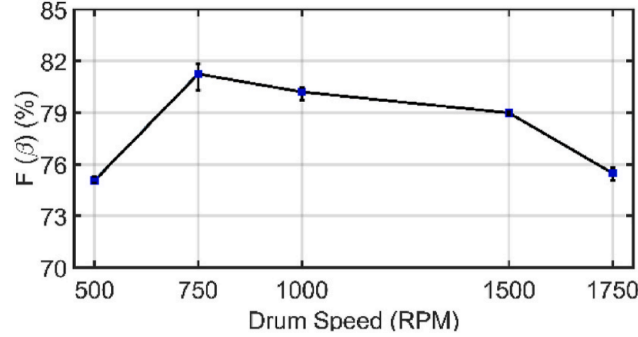
Influence of drum rotation speed on PVDF β -phase

Figure 3.14: Influence of the drum rotation speed on the β phase fraction of electrospun PVDF. Reprinted from [105], Copyright (2021), with permission from Elsevier.

As said before, the orientation of electrospun fibers using a rotating collector favors crystallization of β polymorphism. Increasing the speed of the drum collector is said to increase the fiber alignment and slightly decreases the fiber diameter. If the rotation speed is too small, the mechanical stretch is too low to favor the conversion to the β -phase. On contrary, if the velocity is too high, air disturbances are present near the drum collector and this influence the fiber stretching, reducing the fraction of β -phase.

In the work of Singh [105], it is studied the influence of the drum rotation speed on the fraction of β -phase of a PVDF electrospinning deposition. In this work a drum with a diameter of 12 cm is used as a collector. The drum speed is varied from 500 to 1750 rpm (figure 3.14). Thanks to the following formula:

$$V_{tangential} = \frac{n_{rotations} \cdot 2\pi r}{60s} \quad (3.3)$$

It is possible to find the corresponding tangential velocity (table 3.1).

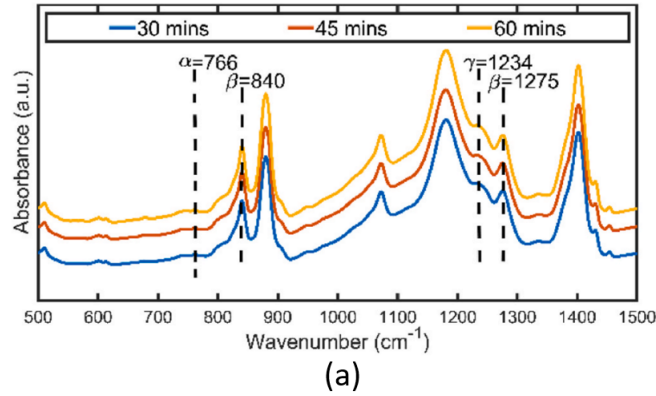
$V_{rotation}$ [rpm]	$V_{tangential}$ [m/s]
500	3.14
750	4.71
1750	10.9

Table 3.1: Conversion from rotation speed to tangent velocities.

From figure 3.14 it is possible to notice that the rotation speed of 750 rpm, that corresponds to a tangential velocity of 4.71 m/s is the one that allow to deposit the PVDF nanofibers with the highest β -phase fraction.

Influence of electrospinning time on PVDF β -phase

Different researchers demonstrate that the percentage of β -phase remains almost constant with the variation of the time of electrospinning nanofiber deposition. Singh et al. [105] in its work collects PVDF nanofibers on a drum collector for three different values of electrospinning time 30, 45 and 60 min but under the same electrospinning condition.



Electro-spinning Time	30 min	45 min	1 h	Avg
β -phase (%)	76.1	75.1	75.8	75.7 ± 0.6

(b)

Figure 3.15: (a) FTIR plot and (b) β -phase fraction for PVDF nanofibers samples prepared with three different electrospinning time. Reprinted from [105], Copyright (2021), with permission from Elsevier.

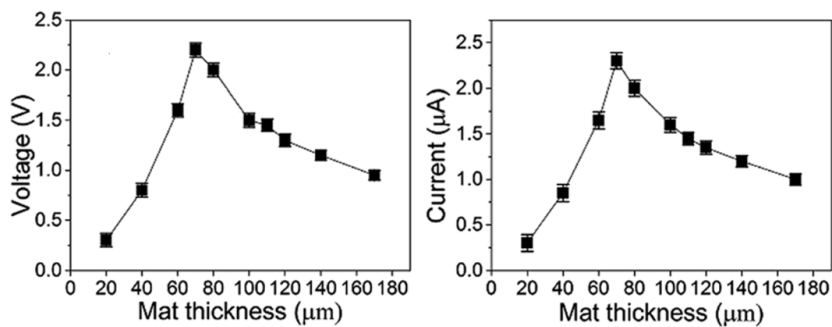


Figure 3.16: Voltage and current outputs of PVDF nanofiber mats with different mat thicknesses obtained with different electrospinning time. Republished with permission of Royal Society of Chemistry, from [104]; permission conveyed through Copyright Clearance Center.

Even if the electrospinning time doesn't influence the fraction of β -phase (figure 3.15(b)) and the FTIR spectra (figure 3.15(a)), it has an effect on the output voltage of the PVDF nanofiber sample due to a change in resistivity. Shao, Hao, et al [104] prepared electrospun PVDF nanofiber samples of different thickness under the same electrospinning condition but varying the electrospinning time to control the mat thickness.

Figure 3.16 shows the effect of PVDF nanofiber mat thickness on the energy conversion performances of the PVDF nanofiber-based device. If the thickness is very low, the voltage and current output are low because short circuit can be created during the compressing process. When the electrospinning time, so the mat thickness, is sufficiently increased both voltage and current output increase, probably due to an improvement of the charge generation consequently to the increase in active material. However, increasing too much the math thickness, also increases the resistance for charge transfer across the mat resulting in a reduction of the voltage and current output.

Chapter 4

Piezoresistive analysis

4.1 Materials and configurations used

The piezoresistive analysis was conducted on nanocomposite obtained by electrospinning process, starting from a water-based polymeric solutions, employed/achieved by adding multiwall carbon nanotubes (MWCNTs) to a certain amount of polyethylene oxide (PEO). The final electrospinning solution was prepared by using PEO with average molecular weight of 600kDa. Conductive composite nanofibers were then obtained by adding different mass fraction of MWCNTs to the prepared PEO solutions.

To reach a final homogeneous polymeric solution for electrospinning, what is named mother solution, was prepared. The mother solution contained 0.4 wt% of MWCNTs (NC3100 by Nanocyl) and 0.4wt% of polystyrene sulfonate Na-PSS, (purchased from Sigma Aldrich), dispersed in DI water. Na-PSS was used as surfactant agent, like said in 2 section 2.2.1, to ensure the dispersion of MWCNTs in deionized water used as solvent. MWCNTs used were in powder form, had a purity higher than 90% and were produced via the Catalytic Chemical Vapor Deposition process [109]. To ensure a good dispersion of MWCNTs, the mother solution was then sonicated by a Digital Sonifier (Branson), composed by a sonicator tip putted inside the prepared solution. The ultrasonication was performed in “pulse” mode (5 s “ON”, 5 s “OFF”) with a power of 30%, for 5 min (figure 4.1).

After the mother solution preparation, solutions with different weight percentage of MWCNTs, from 0 wt% to 6 wt%, were prepared. Water-based solutions of PEO were mixed with water-based MWCNT/PSS solutions under a continuous stirring at room temperature for about 2/3 hours. To obtain the final polymeric solution, an ultrasonication in “pulse” mode was implemented (5 s “ON”, 5 s “OFF”) with a power of 30%, for about 30 min.

The electrospinning equipment used was NANON 01A by MECC (figure 4.2), that allows changing different parameters like voltage output, flow rate during the operation mode of the process. Moreover, it is also possible to define range values for collector rotation speed, frequency and interval of cleaning, moving distance and moving speed of the spinneret, leading thus to collect final nanofiber mats starting from several polymeric solutions.

The operating voltage of this electrospinner can be tuned from 0.5 kV to 30 kV, while the flow rate can be tuned from 0.1 mlh^{-1} to 99.9 mlh^{-1} . Different collectors are available (see section 3.4.2), the planar one that ensure a random deposition of electrospun nanofibers, and the rotating ones, such as drum and mandrel with a tunable rotation speed from 50



Figure 4.1: Branson ultrasonicator used to better disperse MWCNTs inside the solution.



Figure 4.2: Electrospinning system NANON 01A.

to 300 rpm, affecting thus the distribution of nanofibers inside the mat. The obtained polymeric solutions were loaded in a syringe of 6 ml, connected to a needle that can achieve a maximum distance from the planar collector of 150 mm. During my project thesis, two different substrates for the nanofibers' collection were studied. The first one was a non-conductive wire, based on PE, while the second one was a non-conductive hollow wire of a heat shrinkable material. Both of these two substrates

were placed onto rotating mandrel with the main aim to evaluate how the nanofibers' collection can affect the percolation curve of final nanofiber' mats, if compared with the planar deposition.

In this context, indeed, these substrates, with a geometrical structure very different from the commonly planar one, have been chosen to realize new piezoresistive structures, able to be integrated in flexible sensors, optimizing then their performance.

Since these two substrates were both made of an insulating material, characterizing thus by a non-electrical conductive properties that prevent the establishment of an electric field able to expel and accelerate the solution from the spinneret toward the grounded collector, the electrospinning collector were modified as represented in figure 4.3. In particular, with the main purpose to overcome the limit of non-conductivity of insulating substrate, an aluminum foil was folded to produce a quite rigid and stable counter electrode. Subsequently two pieces of copper tape were placed at the extremities of aluminum foil, providing it a grounded potential.

The shape of aluminum foil was adjusted to change the configuration of the electric field

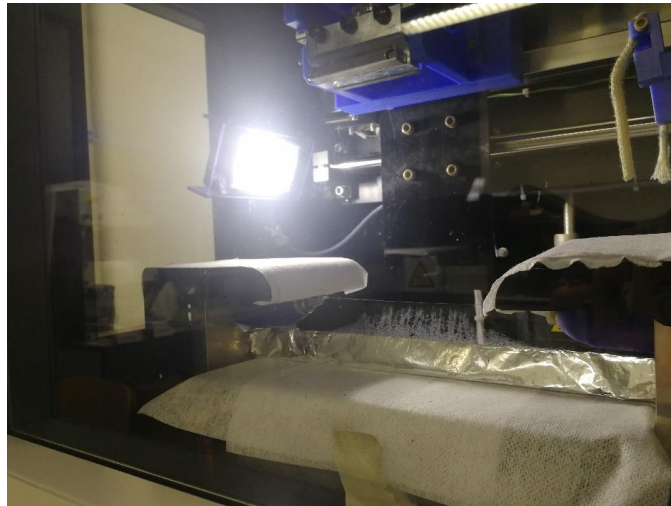


Figure 4.3: Electrospinning set up for the solution deposition on an insulating wire.

lines to enhance the nanofiber deposition onto non-conductive wire used as substrate. Finally, the prepared wire could be connected to the clamps of the collector to rotate in a synchronous way together with them at a rotation velocity. It was important that the wire was well stretched between the clamps in order to have the formation of a sort of nanofiber “spider web” in the vertical direction between the wire and the aluminum tool, like shown in figure 4.4. This “spider web” of composite nanofibers, thanks to the wire rotation, could be rolled on the wire for the deposition. It could often happen that this nanofiber “spider web” become so strong to bring to the rupture of the aluminum tool with the consequent stop of the deposition process. So, it was fundamental to take all the process under control and if necessary, break the nanofiber “spider web”.

Using instead of a insulating wire, an hollow wire of a heat shrinkable material, the electrospinning set up remains almost the same. The only difference is that a piece of aluminum

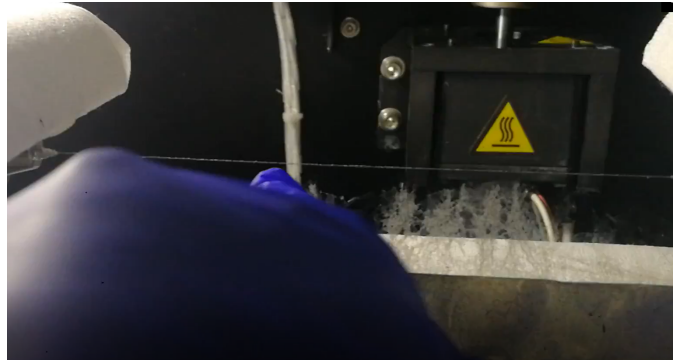


Figure 4.4: Nanofiber spider web formation between the wire and the aluminum tool.

rigid wire was inserted into the hole of the heat shrinkable wire. In this way (figure 4.5) a rigid support for the hollow wire, directly inserted inside the electrospinner collector clamps, was created.

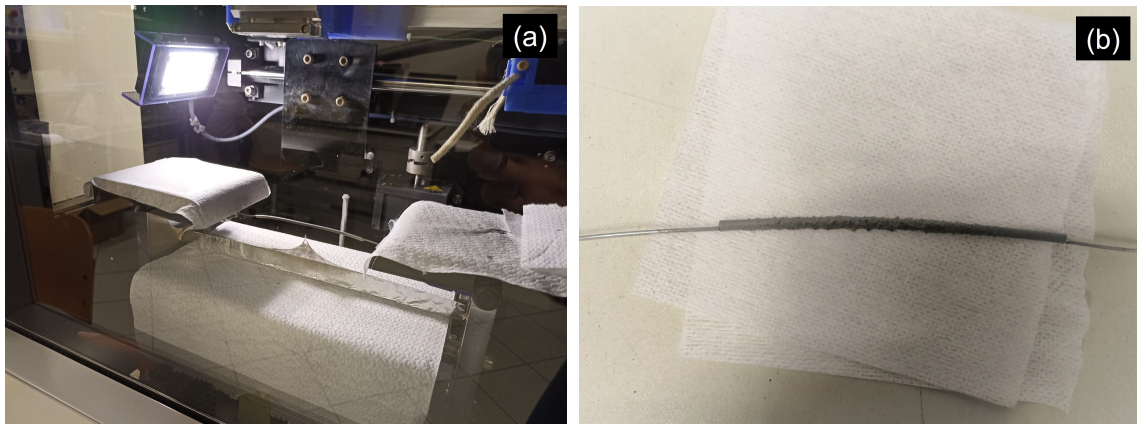


Figure 4.5: MWCNTs/PEO nanocomposite deposition on the hollow wire. (a) Electrospinning setup used. (b) Photograph of an example of nanofiber deposition.

4.2 The percolation curve

A percolative behavior for the electrospun polymer/MWCNT nanofiber composite has been demonstrated by different researchers [113] [114] [115]. This work investigates if the change of the substrate over which composite nanofibers of PEO/MWCNT are deposited, can influence or not the percolative behavior. The work of G. Massaglia, et al. [46] was used as the reference one for this thesis. Indeed, they have investigated the effect of nanofiber/nets on the electrical behaviour of conductive composite nanofibers using PEO and MWCNT. In

this work, the electrospinning process was performed in the planar configuration, using aluminum foils as reference substrates. The experimental values of the electrical conductivity as a function of the MWCNT weight percentages were fitted with the percolation model demonstrating a close correlation between the morphology properties of final nanofiber mats and their electrical behavior. In particular, they demonstrated a significant increase of the electrical conductivity when a dense nano-netting was present in the material as shown in figure 4.6.

In line with the abovementioned results, since during my project thesis one of the main

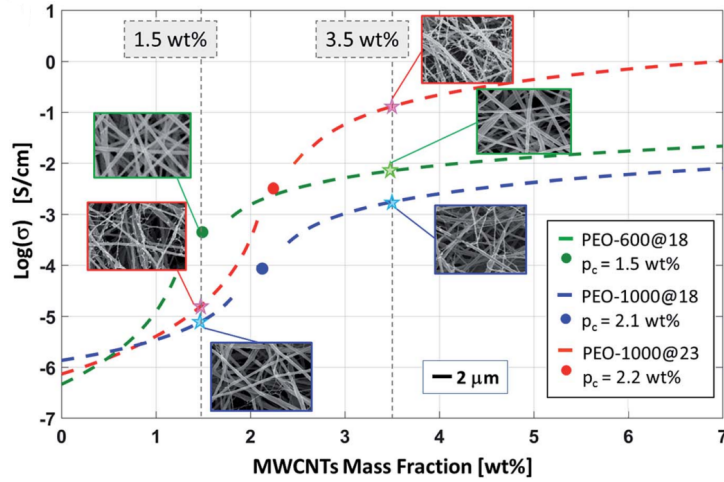


Figure 4.6: Experimental values of the electrical conductivity of composite nanofibers for different concentration of MWCNTs as reported by Massaglia et al. Three sets of samples are represented: PEO with molecular weight of 600kDa (green curve at 18 kV) and 1000KDa (red at 23kV and blue at 18kV curves); the corresponding percolation thresholds are reported and some FESEM images are proposed [46].

target is to verify how the substrates' shape, on which nanofibers were collected, can affect the morphological properties of nanofiber mats and then their percolation behavior different samples at different MWCNT weight percentages has been prepared: 5 wt%, 3.5 wt%, 2.5 wt%, 2.2 wt%, 1.5 wt%, 0 wt%.

4.2.1 Choosing electrospinning parameters of deposition

As it was extensively discussed in the chapter 3, the properties of the final nanofibers by electrospinning depends on several parameters, which can be easily tuned during the whole process Moreover, as deeply explained in chapter 3, several process parameters affect morphological properties of final nanofiber' mats:

- Flow rate that directly modulate the diameter distribution of nanofibers, the higher is the flow rate, the higher is the diameters' distribution of nanofibers.
- Working distance between tip and collector that ensure a uniform distribution of nanofibers without some defect such as beads.

- Rotation speed that can tune the ordered distribution of nanofibers.
- Deposition time influence the thickness of final nanofiber mats.

The solution containing PEO and MWCNT with a weight percentage of 3.5 wt% was electrospun changing those parameters, like reported in table 4.1. The experiment was implemented to define the correct electrospinning parameters able to guarantee a uniform distribution of nanofibers', correlating also the morphological properties with rotation speed values. The whole experiment was conducted by using insulating wire as substrate.

In order to demonstrate that the thickness of the wire doesn't influence the sample Ohmic behavior of the electrospun nanofibers, four different samples were fabricated using two wires of different thickness. Results are reported in table 4.1, where the samples named "SW", which stays for "Small Wire", refers to the wire substrate of smaller diameter and "BW", which stays for "Big Wire", refers to the wire substrate of bigger diameter (see table 4.3). As it is possible to see the same electrospinning parameters values were tested on both the substrates for samples SW1 and BW1.

Sample	Applied voltage [kV]	Tip to collector distance [mm]	Feed rate [ml/h]	Rotation speed [rpm]	Spinneret width [mm]	Deposition time [min]
SW1	29.5	145	0.6	100	70	20
BW1	29.5	145	0.6	100	70	20
SW2	23.5	145	0.5	100	70	20
BW2	29.5	145	0.6	100	85	20

Table 4.1: Electrospinning parameters used for the realization of four different samples at 3.5 wt% of MWCNT.

The investigation of the electrical performance of the samples help to understand which set of electrospinning parameters is the best one for the nanofiber's deposition. To do that a benchtop digital multimeter KEITHLEY 6430 was used like in figure 4.7.

Firstly, a bias voltage of 1V was applied at the extremities of each of the sample wires and current as a function of time was plotted for a number of points equal to 100. Ideally graphs of current with time applying a constant voltage on samples should be a straight horizontal line, that is, the same current value should be obtained each time. Graphs in figure 4.8 detect a trend of current with time that is a straight horizontal line.

Then, it was important to understand which of these samples respect in a better way the Ohm's laws.

The first Ohm's law establishes that the potential difference at the ends of a resistor is equal to the product of the resistance for the intensity of the current passing through it (equation 4.1):

$$\Delta V = R \cdot I \quad (4.1)$$

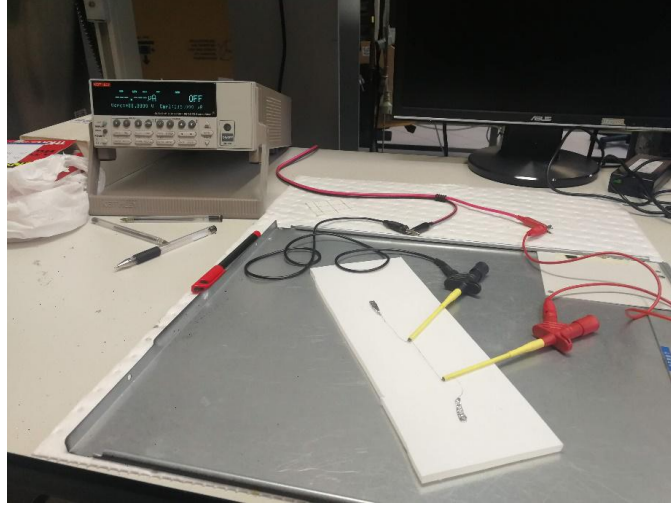


Figure 4.7: Set-up for the sample's electrical characterization.

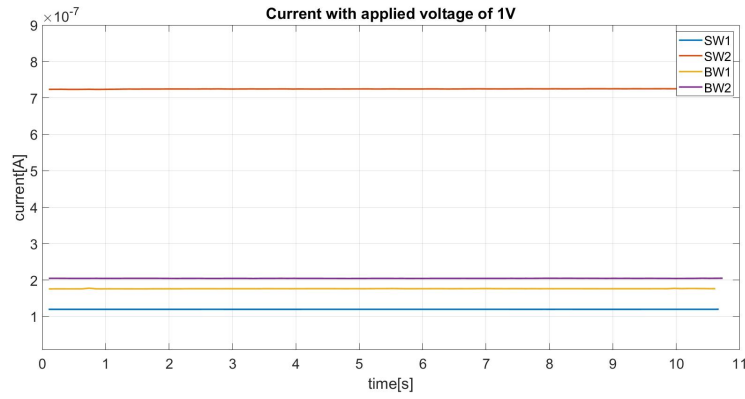


Figure 4.8: Current values obtained setting a bias voltage equal to 1V for each sample.

While the second Ohm's law describes the relationship between the electrical resistance and the resistivity (equation 4.2):

$$R = \rho \frac{\Delta l}{S} \quad (4.2)$$

where Δl is the resistor length and S is the area of the cross-section. Electrical resistivity represents the ability of a material to resist the passage of electric charges and, differently from the electrical resistance, it's a specific property of the material and depends mainly on the microscopic structure of the medium. So, all the materials are characterized by a specific resistivity value that are only temperature dependent.

For each of the samples the I/V characteristic was made for two different length values Δl , setting a voltage varying from -10V to 10V and measuring the corresponding output current, in a number of points which have been set to 6000. The two Δl values were defined

by putting two opposite polarity tips of the multimeter at two different distances on the sample under test. Experimental data analysis was performed by implementing MATLAB as program language. Toward Matlab tool, the resistance value was calculated as the slope of IV curves.

Figure 4.9 analyzes IV graphs obtained for each sample, leading thus to establish the

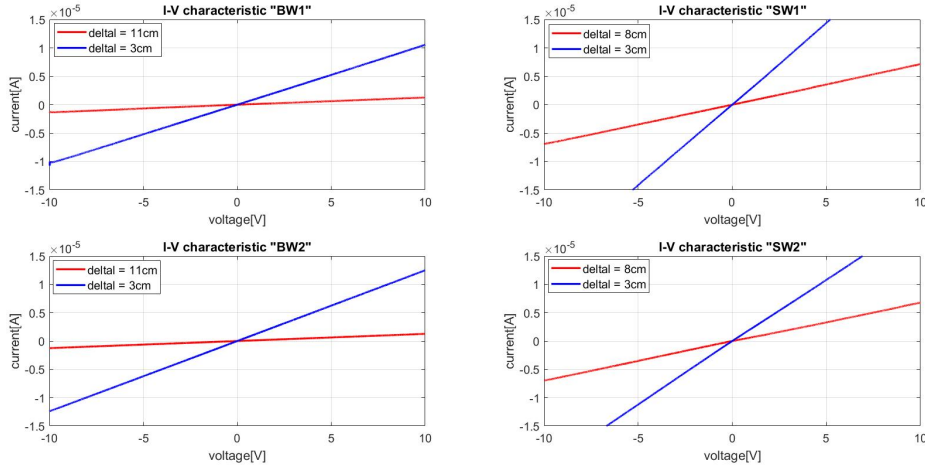


Figure 4.9: I/V characteristic for each sample.

presence or not of the linear Ohmic trend. All results allowed confirming how/that linear Ohmic trend was present for all four samples. Moreover, it was also verified that increasing Δl , the electrical resistance increases, and so the slope of the I/V characteristic decreases. In detail, in table 4.2 all resistance values for each sample is reported.

Sample	Δl [cm]	Resistance [Ω]
BW1	11	$7.66 \cdot 10^6$
BW1	3	$9.57 \cdot 10^5$
BW2	11	$7.93 \cdot 10^6$
BW2	3	$8.02 \cdot 10^5$
SW1	8	$1.42 \cdot 10^6$
SW1	3	$3.49 \cdot 10^5$
SW2	8	$1.46 \cdot 10^6$
SW2	3	$4.54 \cdot 10^5$

Table 4.2: Electrical resistance values for each sample and for each Δl .

Another test to verify the validity in each sample of the Ohm's laws, was performed. With the main aim to evaluate the electrospinning parameters, able to obtain a final

nanofiber mats, characterizing by optimized functional properties, the electrical conductivity was calculated as the reverse of resistivity, defined by equation 4.3:

$$\sigma = \frac{\Delta l}{R} \cdot \frac{1}{S} \quad (4.3)$$

where Δl refers to different length values, R is the bulk resistance, defined as the slope of IV curves and S is the cross-section of each sample, evaluated by analyzing the optical microscope images, as reported in figure 4.11. Indeed, thanks to optical microscope (LEICA VZ80 C) (Appendix A.1) (figure 4.10), it was possible to calculate the cross section of the cylindrical wire ($S = \pi \cdot r^2$) by measuring the diameter of all samples.

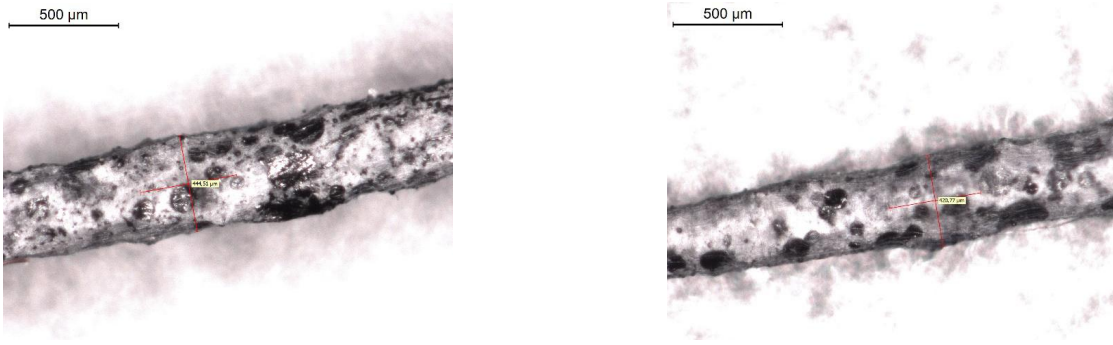


Figure 4.10: Two optical microscope pictures of the sample “BW1” for the diameter evaluation.

Table 4.3 reported for each sample, 4 different values of the diameter measured in different regions of the wire, allowing the definition of an average diameter, representative of each sample, which is able to take in account a non-perfect uniformity of the nanofiber mat onto the substrate.

Sample	$d_1[\mu\text{m}]$	$d_2[\mu\text{m}]$	$d_3[\mu\text{m}]$	$d_4[\mu\text{m}]$	$d_{av}[\mu\text{m}]$
BW1	444	445	435	431	439 ± 7
SW1	289	150	145	169	188 ± 72
BW2	471	437	485	450	461 ± 24
SW2	232	210	187	513	286 ± 163

Table 4.3: Values of diameters obtained thanks to the use of an optical microscope.

Since equation 4.3 highlights that electrical conductivity results to be inversely proportional to the parameter defined as ratio between R and Δl , it is important to report the trend of electrical conductivity vs the parameters $R/\Delta l$, as represented in figure 4.11. It is possible to see the presence of two dots of two different colors. For each plot and wire, green dot refers to electrical conductivity value related to longer Δl , while cyan dot refers to electrical conductivity value related to shorter Δl .

It is interesting to note that these points related to experimental electrical conductivity values can completely overlap onto the theoretical curve, defining the electrical conductivity as a function of $R/\Delta l$.

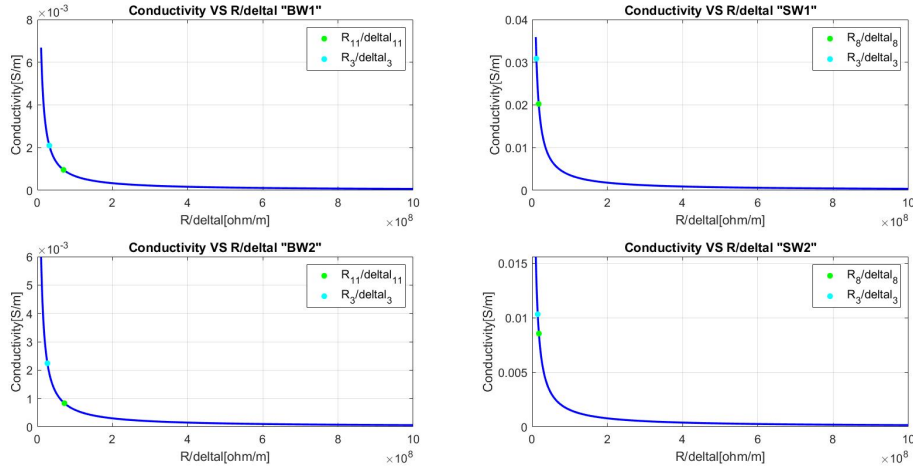


Figure 4.11: MATLAB plots of the electrical conductivity as a function of $R/\Delta l$ for each sample.

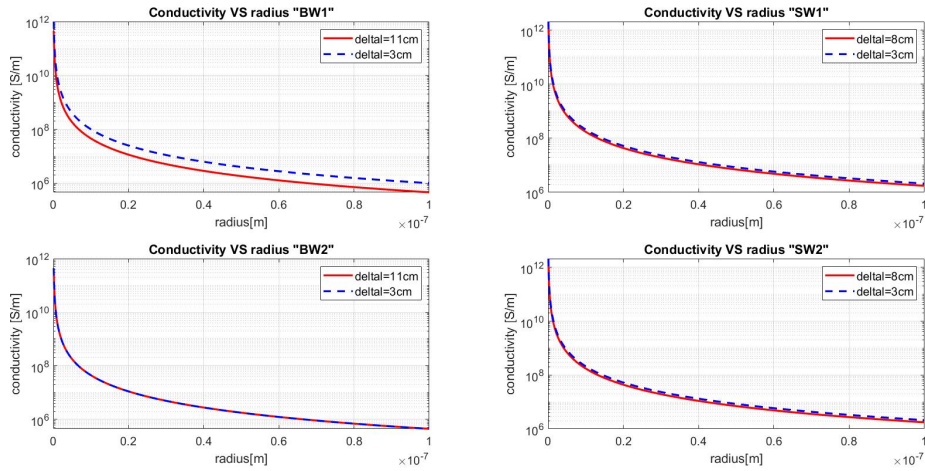


Figure 4.12: MATLAB plots of the electrical conductivity as a function of the radius of the cross section for each sample.

For each sample remembering that resistivity (and so electrical conductivity) is only material and temperature dependent, from Ohm's laws, we expected the curves of electrical conductivity as a function of the radius of the cross section relative to each $R/\Delta l$ to

be as overlapping as possible. From results reported in figure 4.12, it is evident that the perfect overlapping of the two curves relative to the two different $R/\Delta l$ values is present only for sample “BW2”. Therefore, electrospinning parameters used for the deposition of MWCNT/PEO nanofibers at 3.5 wt% used to obtain the sample “BW2” were chosen also for the deposition of the solutions with all the other MWCNT weight percentages.

4.2.2 Final implementation of the percolation curve

To obtain the final implementation of the percolation curve, conductivity values were calculated for each MWCNT weight percentage as reported in table 4.4. More information about the evaluation of electrical conductivities is summarized in Appendix B.

wt%	σ_{final} [S/cm]
0	$5.62 \cdot 10^{-7}$
1.5	$5.45 \cdot 10^{-7}$
2.2	$1.65 \cdot 10^{-6}$
2.5	$5.62 \cdot 10^{-4}$
3.5	$1.59 \cdot 10^{-2}$
5	$5.96 \cdot 10^{-2}$

Table 4.4: Electrical conductivity values for different MWCNT weight percentages.

The experimental values of the electrical conductivity (table 4.4) as a function of the MWCNT weight percentages are shown in figure 4.13. Data were fitted thanks to the percolation model described in the second Chapter 2.2.2 [46], that describes the electrical conductivity as a function of conductive filler concentration above and below the percolation threshold.

The fitting curve shown in figure 4.13 shows that a percolative behavior is present with a percolation threshold equal to 2.5 wt%. Indeed, the increase of the weight percentage of MWCNT inside nanofibers bring to an improvement of electrical properties linked to the formation of a conductive network inside the nanostructured polymer matrix. Moreover, this conductive network is created at concentrations of conductive filler equal or higher than the percolation threshold. Specifically, for concentration of MWCNT lower than 2.5 wt%, the conductive network should be mostly absent, while should become more present for higher concentrations. So, increasing the weight percentage of MWCNT at percolation threshold, the electrical conductivity starts to increase many orders of magnitude with a very low increase of the filler fraction. After this percolation threshold, the curve starts to stabilize to a certain value near the one of 6 wt%.

Taking a comparison between the percolation curve obtained in the work of Massaglia et al. (figure 4.6) and the one obtained in this work (figure 4.13), some considerations can be done.

Looking the green curve of figure 4.6, relative to the deposition of the solution containing PEO with molecular weight of 600 kDa (PEO-600), the same used in this work, we can immediately notice that the percolation threshold for PEO/MWCNTs planar nanofiber mats is slightly lower (2.2 wt%) than the one obtained by fitting experimental data of

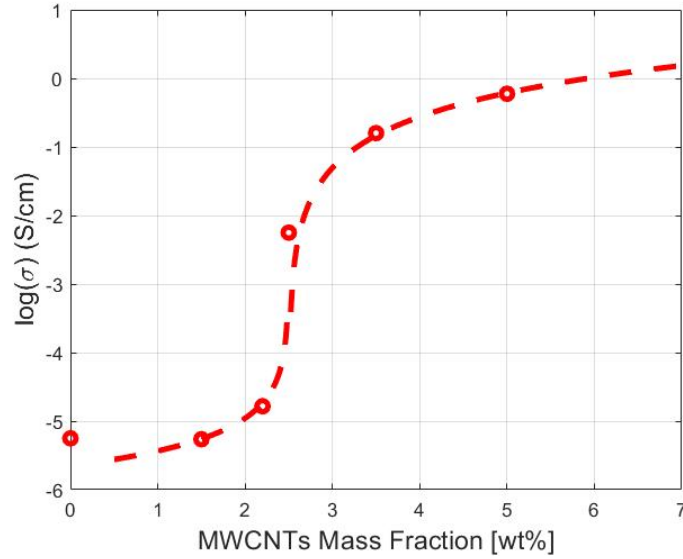


Figure 4.13: Fitting of experimental values of electrical conductivity of composite nanofibers for different MWCNTs concentrations.

table 4.4. As a first approximation, this is in accordance with what was demonstrated in the reference article, where, observing the two curves (blue and red curves of figure 4.6) related to the deposition of the solution containing PEO with molecular weight of 1000 kDa (PEO-1000), it is observed that using a higher working voltage a higher percolation threshold is obtained. So, being the working voltage used in this work (29.5 kV) higher than the one in the article of Massaglia et al. [46] (18 kV), the fact of having obtained a higher percolation threshold was quite expected.

Comparing instead the electrical conductivity values obtained after the percolation threshold, it is noted that those obtained in the present thesis work are higher than those obtained in the green curve of figure 4.6. This was also to be expected, as demonstrated by Massaglia et al. [46], because the increase of the working voltage brings to samples with more compact and dense filler network, increasing the probability of charge transfer across the mat of nanofibers, leading to higher electrical conductivity values for the same percentage of conductive filler. Indeed, this behavior is in line with the red and blue curves as reported in figure 4.6 relative to the PEO/MWCNT nanofiber deposited with respectively 23 kV and 18 kV as working voltage.

Finally we have to consider that in this work electrospun nanofibers were collected in wire and tubular configurations different from the traditional planar one used in the literature [46]. The configuration used in this work bring to a more orderly nanofibers assembly (see figure 4.14) deposited with respect to the random nanofiber deposition present in the planar configuration. In line with this hypothesis, FESEM pictures (figure 4.14) demonstrated and confirmed the presence of an ordered distribution of nanofibers inside final obtained mat. Indeed, morphological images highlighted how those nanofibers, with different amount of MWCNTs, showed a sort of directionality of themselves. Probably, the more

orderly structure of nanofibers obtained in this work, leads to a greater difficulty of contact between conductive nanonets reducing the probability of charge transfer across the mat of nanofibers and finally brings to an increase of the percolation threshold and a reduction of the electrical conductivity above threshold. Moreover, this higher percolation threshold found with respect to the one in literature [46] can be also due to the fact that during the electrical characterization performed, the electrical contacts were not optimally developed.

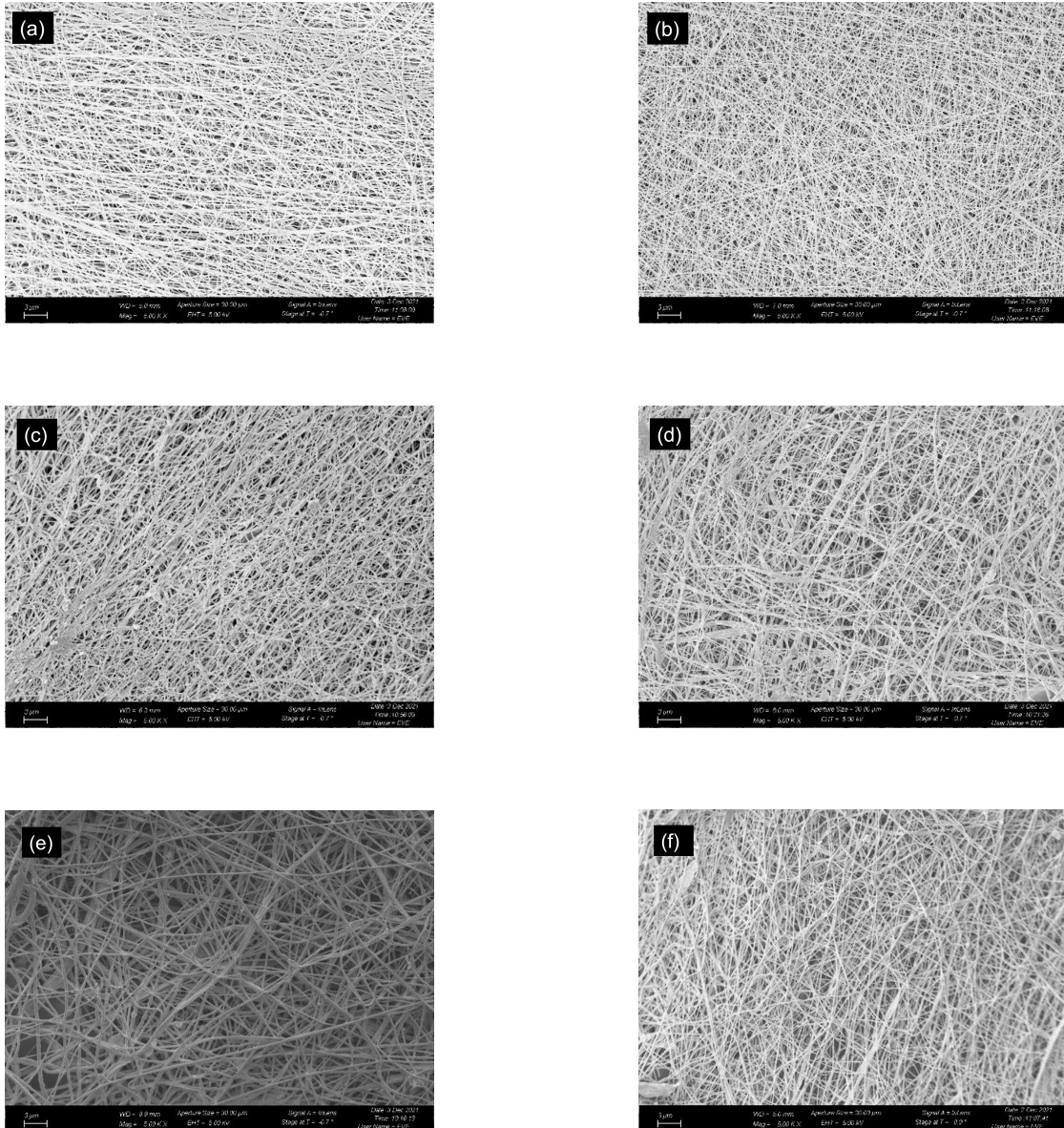


Figure 4.14: FESEM pictures of nanofibers at different MWCNTs concentrations: (a) 0 wt%, (b) 1.5 wt%, (c) 2.2 wt%, (d) 2.5 wt%, (e) 3.5 wt%, (f) 5 wt%.

4.3 Piezoresistive analysis of composite nanofibers

The piezoresistive effect represents an electrical resistance change of a material when a mechanical strain is applied on it. Like it was described in the chapter 2 of this work, different researchers try to explain the piezoresistive effect in nanocomposite materials. In this section we want to understand if the piezoresistive effect is present in our samples and if the nanofiber collection configuration may influence or not the piezoresistive response. In order to study the piezoresistive effect we have prepared two PEO/MWCNT solutions, the first with a MWCNTs weight percentage equal to 6 wt% and, in the second one, equal to 3 wt%. Since many works in the literature [4] demonstrated how the piezoresistive response of composite materials resulted to be stronger when the amount of conductive filler is close to the percolation threshold, we chose one concentration of 3 wt% MWCNTs, close to the percolation threshold, and one higher than the threshold (6 wt%). This happens because near percolation a small variation of the MWCNTs weight percentage brings to an abrupt change of electrical conductivity and so, a small pressure applied on our sample could bring to a large change of electrical conductivity [4]. The application of strain or of a certain pressure in a sample near percolation could lead to a reduction of the distance between nanonets, bringing to the construction of new conductive paths (figure 4.15), improving the charge transfer across the mat of nanofiber. This led to a strong electrical resistance change and so, to a great electrical conductivity variation. On the other hand, applying a certain pressure to a sample with a MWCNT weight percentage above percolation and very far from it, lead to a smaller change of its electrical conductivity.

The electrospinning parameters used for the nanofiber deposition of these two solutions are

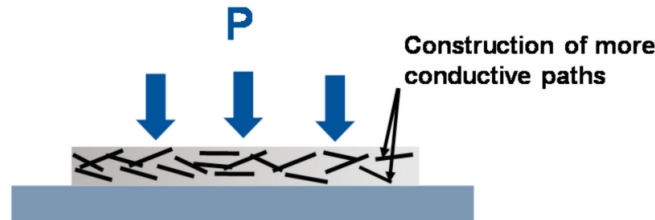


Figure 4.15: FESEM pictures obtained using 1.5 wt% MWCNTs using a working voltage of (a) 18 kV and 23 kV [4].

those shown in table 4.1 for the sample “BW2” except for the electrospinning time which has been increased to 1 h and 20 minutes, in order to have a greater number of nanofibers deposited. These two solutions (6 wt.% and 4 wt.%) were deposited on an hollow wire while it was also performed a piezoresistive analysis on a wire over which a composite nanofiber of MWCNT/PEO at 3.5 wt%, so near percolation, were electrospun.

A preliminary qualitative analysis was performed on a sample obtained by the electrospinning deposition of the solution containing MWCNT with a weight percentage of 6 wt%. Using a bias voltage of 1V, current values were measured thanks to the use of a digital multimeter. During this time interval, a pressure of unknown value was applied by fingers (as shown in figure 4.16 (c) and (d)) to the sample a certain number of times using two different set ups. During this electrical characterization we tried to keep the sample in a

position as stable as possible, so as not to deform it and to ensure that the piezoresistive response obtained was influenced only by the applied pressure.

In figure 4.16 (a) and (b) measured values of current were plotted as a function of time. It is immediately evident that the application of a pressure on the sample brings to a change of the measured current as a result of a variation of the sample electrical resistance. We also observe that in both graphs there is a sort of drift of the current over time probably due to the fact that by applying a certain pressure on the sample, we are going to change the morphological structure of the nanofibers deposited on the substrate that will take a certain amount of time to be able to return to the initial one before solicitation. In order to verify this concept, the current as a function of time applying a bias voltage of 1V (figure 4.17 (a)) and the I/V curve obtained applying a voltage between -10V and 10V (figure 4.17 (b)), were plotted before and after the application of a pressure on the sample.

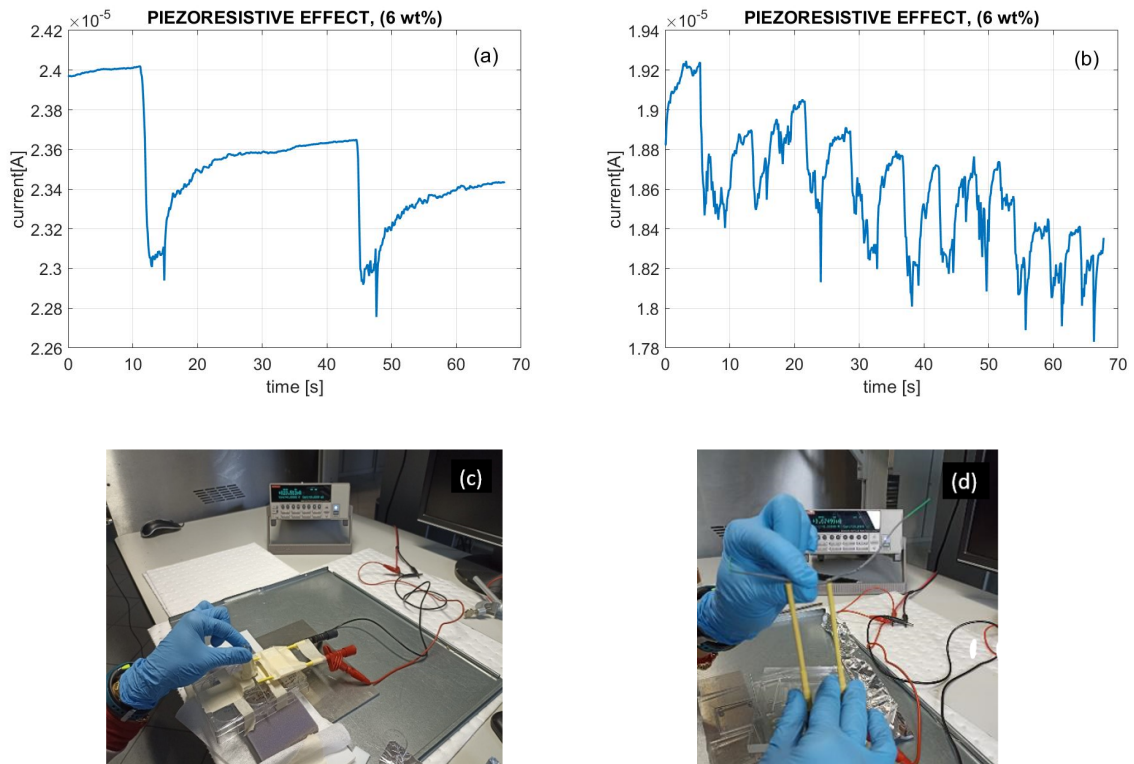


Figure 4.16: Preliminary piezoresistive analysis on samples containing MWCN with weight percentage of 6 wt%. (c) and (d) are the set-up of measurement while (a) and (b) are the corresponding characteristics obtained.

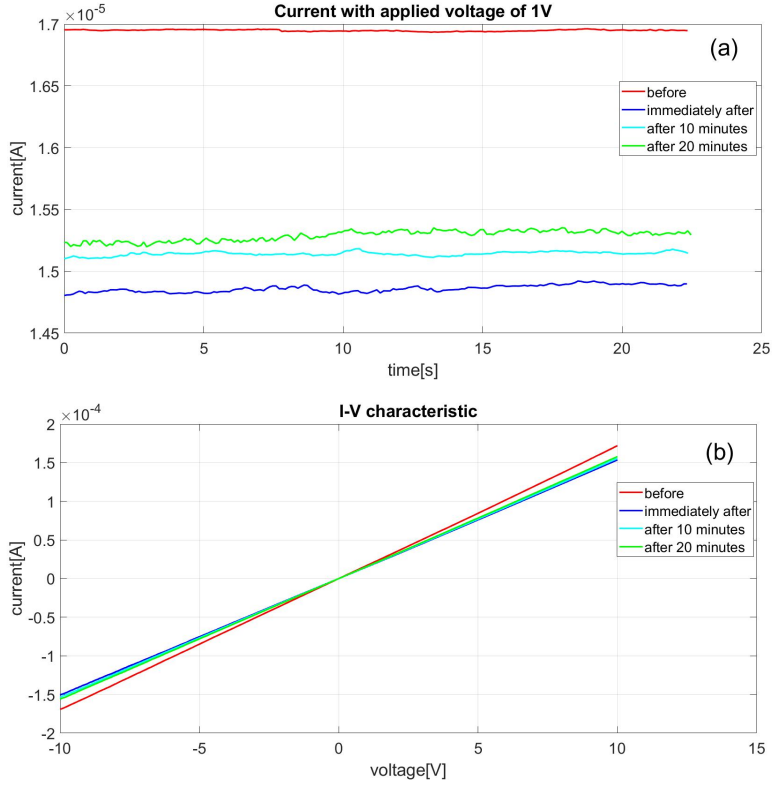


Figure 4.17: Electrical characterization of sample containing MWCNT with weight percentage of 6 wt%. (a) Current as a function of time (bias voltage equal to 1V), (b) I/V characteristic.

In both figures (figure 4.17 (a) and (b)) we tried to understand what happened to the sample immediately after (blue curves), after 10 minutes (cyan curves) and after 20 minutes (green curves) from the application of a certain pressure observing that the sample tends to regain the initial conformation before stress (red curves). Moreover, from the I/V curves it was possible to verify Ohmic trend was respected and to calculate the corresponding electrical resistance values as the I/V curves slope (table 4.5).

TIME OF MEASUREMENT	R [Ω]
Before	$5.87 \cdot 10^4$
Immediatly after	$6.59 \cdot 10^4$
After 10 minutes	$6.49 \cdot 10^4$
After 20 minutes	$6.38 \cdot 10^4$

Table 4.5: Electrical resistance values of a sample containing MWCNT weight percentages of 6 wt% before and after different time intervals from the stress applied on it.

Values of electrical resistance shown in table 4.5 were found to comply with the trend of the resistance values for the samples containing the different weight percentages of

MWCNT shown in table B.1. In support of what has been ascertained so far, it is seen that the resistance values after the application of pressure on the sample, tend more and more with the passage of time to approach the resistance value before the stress. Subsequently, we tried to make a more accurate analysis, trying to understand how the samples containing the two percentages of MWCNT (3 wt% and 6 wt%) responded to the application of a pressure of known value. The set up used is shown in figure 4.18. In addition, in figure 4.19, it is shown the set up used during the application of a pressure

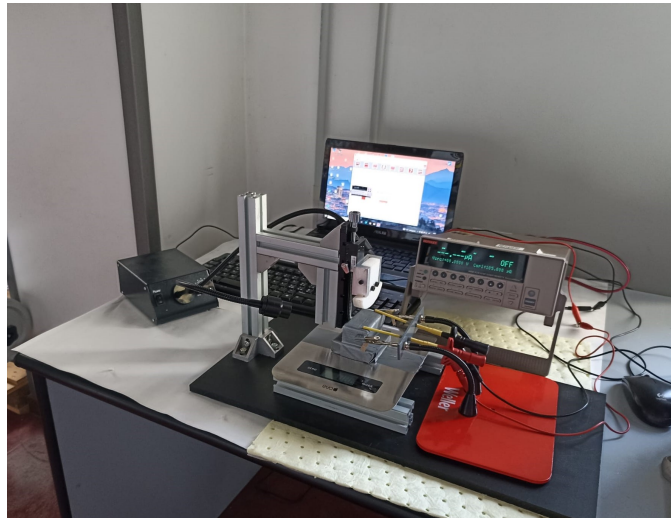


Figure 4.18: Piezoresistive characterization set-up.

on an hollow wire and on a wire.

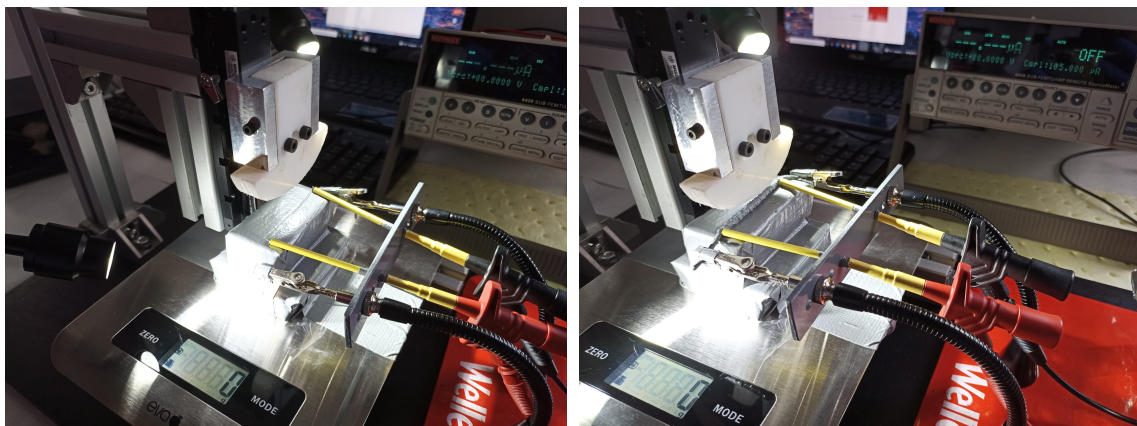


Figure 4.19: Piezoresistive characterization set-up for a wire (left) and for an hollow wire (right).

The set up used is composed by a tool that can apply a pressure on our sample. The sample was putted on a support as mechanically coupled with the surface of an electronic scale. So, when the tool touches the sample, through the scale we can measure a certain weight that, knowing the contact surface between the sample and the tool, will correspond to a certain pressure applied on it. Moreover, the sample is electrically connected to a digital multimeter, thanks to which we can perform an electrical characterization with different value of pressure applied on it. Applying a pressure we induce a deformation on the substrate over which nanofibers are deposited, and so also the nanofiber mat undergoes a certain deformation, like shown in figure 4.20 for a hollow wire substrate, which can bring to a current variation. It was important to keep the sample as stable as possible on the surface of the digital scales in order to minimize other contributions of deformation.

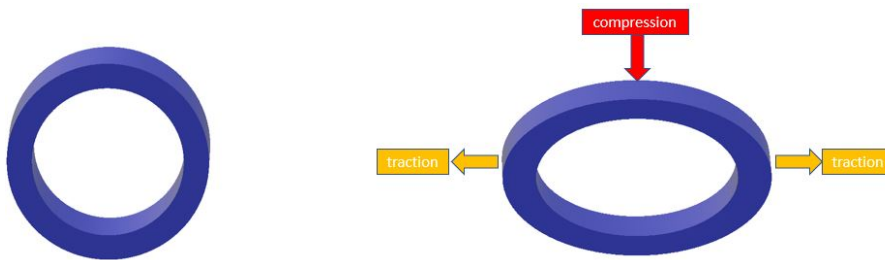


Figure 4.20: Schematic representation of the hollow wire used as deposition substrate with the starting shape (left) and after pressure application (right).

In order to confirm the Ohmic behavior, the I/V curve before and after the application of a pressure was analysed also for the wire over which a composite solution containing MWCNT weight percentage of 3.5 wt%, as shown in figure 4.21.

Figure 4.21 not only demonstrates a good electrical behavior of the nanofiber mats both

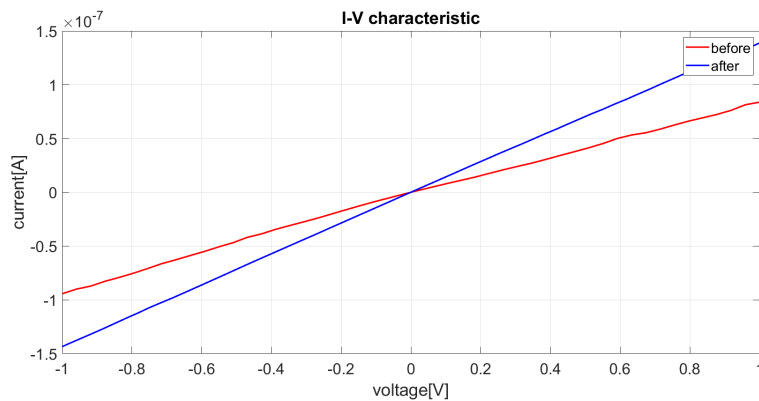


Figure 4.21: I/V characteristic of sample containing MWCNT with weight percentage of 3.5 wt%.

before and after the application of deformation, but also told us that this behavior is independent from the substrate shape used to deposit the nanofiber mat, but only depend on the weight percentage of MWCNT inside the solution. Anyway, further analysis should be performed to investigate in more details the behavior of the sensor during cyclic loading. Figures 4.22, 4.23 show the plots of current as a function of time applying a bias voltage of 1V during the application of a pressure for samples containing MWCNT weight percentage of 6 wt% and 3.5 wt% respectively. In addition, after each of these figures, there is a table (table 4.7 – 4.8) containing the pressure values applied to the nanofiber mats, considering the fact that, being the measurement set up not entirely accurate, the pressure values are approximate.

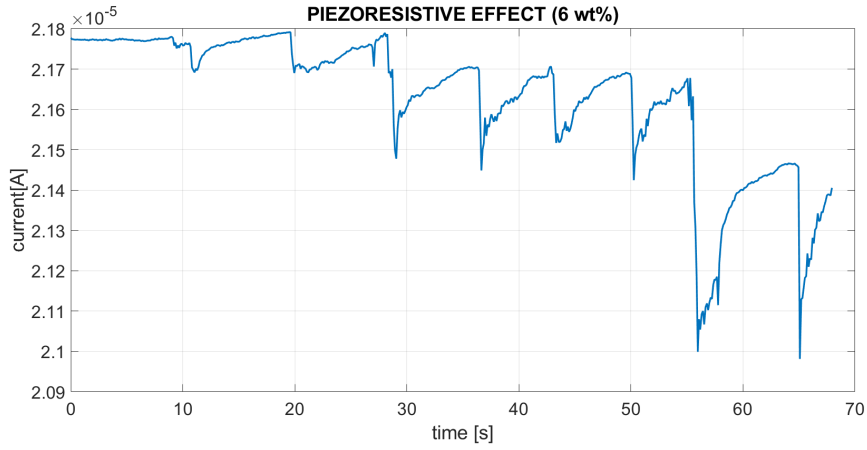


Figure 4.22: Piezoresistive analysis on nanofiber mat deposited on a hollow wire from a solution containing MWCNT with weight percentage of 6 wt%.

m[g]	F=mg[N]	P=F/S[kPa]
~96	0.9	~22
~96	0.9	~22
~240	2.4	~57
~240	2.4	~57
~240	2.4	~57
~240	2.4	~57
~300	2.9	~71
~300	2.9	~71

Table 4.6: Values of pressure applied on wire with MWCNT weight percentage of 6 wt%.

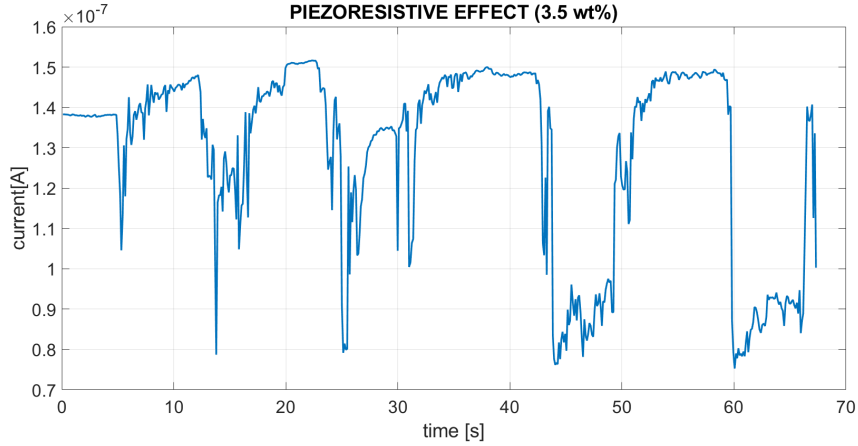


Figure 4.23: Piezoresistive analysis on nanofiber mat deposited on a hollow wire from a solution containing MWCNT with weight percentage of 3.5 wt%.

m[g]	F=mg[N]	P=F/S[MPa]
~120	1.2	~0.4
~170	1.7	~0.5
~205	2.4	~0.6
~320	3.1	~0.8
~320	3.1	~0.8

Table 4.7: Values of pressure applied on wire with MWCNT weight percentage of 3.5 wt%.

From the electrical characterization of all the samples it is observed that, as expected, applying greater pressures we obtain greater current variations and therefore, greater electrical resistance changes. This can be easily explained, because the application of a greater pressure on our sample, brings to a greater variation of the morphological structure of nanofibers deposited on the substrate, changing in a stronger way charge conductive paths.

4.3.1 Sensitivity curves

The sensitivity of a piezoresistive pressure sensor can be defined as:

$$S = \frac{\Delta R/R_0}{P} \quad (4.4)$$

where $\Delta R/R_0$ is the change in the device electrical resistance due to a specific value of the applied pressure P . In order to find the sensitivity value for both the two deposition configurations (wire and hollow wire) and for the two MWCNT weight percentages near and above and far from the percolation threshold, an electrical characterization was performed using the set-up shown in figure 4.18. Specifically, for each sample were performed different I/V curves applying a voltage in the range $-10 \div 10$ V for five different values of the applied pressure ranging between 0 and 60 kPa, for the hollow wire, and between 0 and

0.9 MPa, for the wire. Thanks to the different I/V curves, the electrical resistance values were calculated for each value of the applied pressure. Subsequently, the absolute values of electrical resistance variation $\Delta R/R_0$ obtained were plotted for each sample as a function of the applied pressure, like shown in figures 4.24, 4.25, 4.26 .

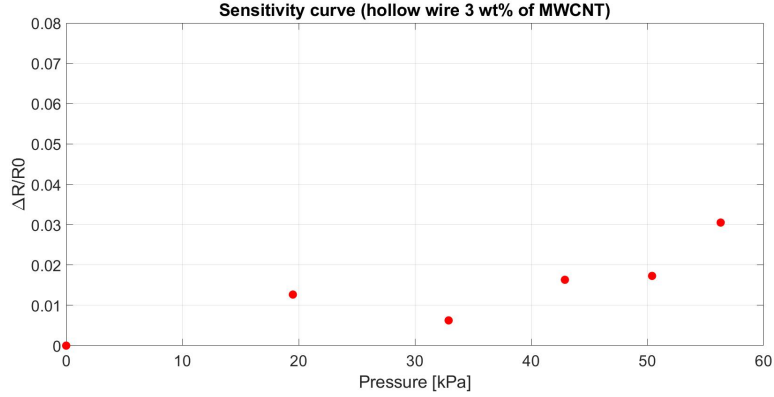


Figure 4.24: Electrical resistance variations as a function of the applied pressure for the hollow wire at 3 wt% of MWCNT.

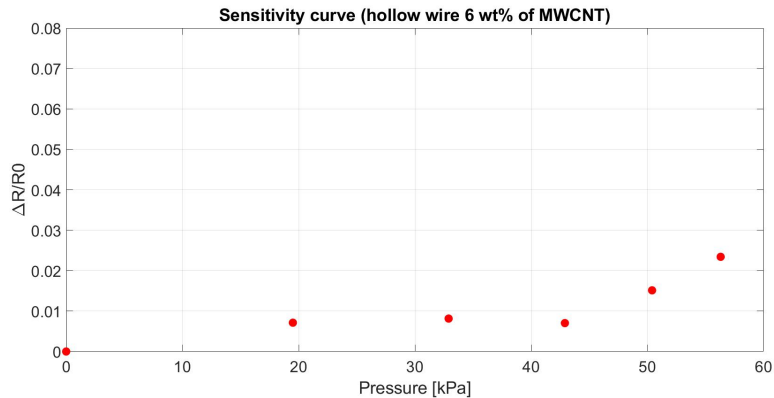


Figure 4.25: Electrical resistance variations as a function of the applied pressure for the hollow wire at 6 wt% of MWCNT.

In all the three plots, the trend is comparable with what is present in literature [130] [131]. First of all, it is possible to deduce an increase in the electrical resistance variation with the increasing applied pressure. This behavior can be explained as a result of the destruction of the existing percolating channels which consequently bring to a variation of the electron's path and so, to an increase of electrical resistance [131]. Moreover, in the work of Chen et al. [131] it was observed the presence of three different regions of the resistance-pressure curve obtained by a sample of silicon rubber/graphite

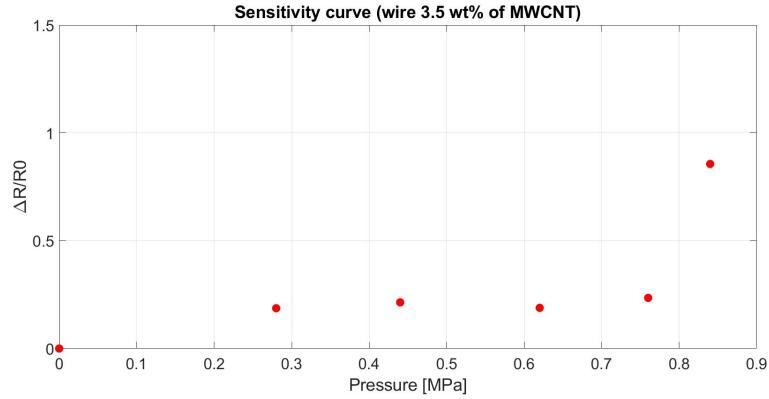


Figure 4.26: Electrical resistance variations as a function of the applied pressure for the wire at 3.5 wt% of MWCNT.

nanosheets nanocomposite. In the "first region", corresponding to low pressure values applied, it is possible to observe an almost flat line. In the "second region", when pressure increases, the electrical resistance values rises by three order of magnitude while in the "third" one the resistance increases by more than five orders of magnitude. Specifically, in the third region the destruction of the existing percolating channels is enhanced, bringing to a sharply increase of the electrical resistance.

Comparing this behaviour with what was found in curves of figures 4.24, 4.25, 4.26, the trend previously described is almost respected. Specifically, it can be deduced the presence of the almost flat "first region", where the increasing pressure doesn't bring to a big variation of the electrical resistance.

wt%	$(\Delta R/R_0)_1$ [%]	$(\Delta R/R_0)_2$ [%]	$(\Delta R/R_0)_3$ [%]	$(\Delta R/R_0)_4$ [%]	$(\Delta R/R_0)_5$ [%]
3	1.3	0.6	1.6	1.7	3.5
6	0.7	0.8	0.7	1.5	2.3

Table 4.8: Values of percentage resistance change obtained applying the same pressure value on the two samples with MWCNT weight percentage of 3 wt% and 6 wt%.

Moreover also the presence of the "second region", where the resistance variation starts to increase because of the application of an higher pressure, can be deduced. Probably, by the application of higher pressure values than the ones used in this characterization, also the third region could be verified.

Taking a comparison between the resistance variation-pressure curves obtained for the hollow wires samples containing a MWCNT weight percentage of 3 wt% with the one at 6 wt%, some considerations can be done. Specifically, like reported in table 4.8, with the same pressure value applied on each of the two samples at different conductive filler concentration, the electrical resistance variation results to be higher for the sample near percolation (3 wt%). This is in accordance with previous works [130] [131] and can be probably due to the fact that around the percolation threshold, a small change in pressure can cause a

larger change in electrical resistance since in this region the resistance changes abruptly with the conductive filler volume fraction.

Chapter 5

Piezoelectric effect

5.1 Materials and configurations used

The piezoelectric analysis was conducted on poly(vinylidene fluoride) (PVDF) nanofibers, prepared by applying the electrospinning technique using different types of collectors. Typically, in the final solutions to be electrospun, PVDF is dissolved in a single polar solvent such as dimethylacetamide (DMAc), dimethyl sulfoxide (DMSO), dimethylformamide (DMF), and N-methyl-2-pyrrolidone (NMP), or a binary mixture of these solvents with acetone [107]. In this work, the solutions were prepared by dissolving 14 wt% of PVDF in powder form (M_w 534.000, Sigma-Aldrich) in the solvent mixture DMF (Sigma-Aldrich) and acetone (Sigma-Aldrich) with a volume ratio 50:50 wt%. As deeply investigated in the literature [116] [117], the definition of a binary mixture of a polar solvent with acetone played a pivotal role to tune the solution viscosity and the final The solvent mixture used is not a random choice. Indeed, in the work of Choi et al. [116] it was demonstrated that using a binary mixture of a polar solvent with the addition of acetone, the viscosity of the PVDF solution is reduced and, like previously discussed (see chapter 3 section 3.6.1), this can be an advantage for the nanofiber stretching and for the final β -phase formation. In this context Choi et al. [116] demonstrated how the addition of acetone to a polar solvent reduced final viscosity of solution, ensuring a nanofiber stretching and a consequent formation of β -phase. Gee et al. [117], moreover, investigate how different polar solvents, used for polymeric solution, can affect the fraction of β -phase inside the PVDF nanofibers, demonstrating the effectiveness of DMF as polar solvent to induce an higher fraction of β -phase with respect to nanofibers produced with DMSO and NMP. On the contrary, several works in the literature [79], [132] showed that a fraction of acetone in the solvent mixture above 50 v/v%, limited the formation of β -phase inside the final nanostructured samples. Taking into account all these results, during my project thesis, a polymeric solution contained 14 wt% of PVDF in powder form (M_w 534.000, Aldrich) in the solvent mixture DMF and acetone (purchased from Sigma-Aldrich) with a volume ratio 50:50 wt% was used for electrospinning process.

The PVDF/DMF/acetone final solution was heated to 60 °C and stirred with a rotation speed of 310 rpm for 30 minutes and subsequently it was left on the stirrer at the same rotation speed of rotation for at least 2 hours at room temperature.

The electrospinning equipment (NANON 01A by MECC) was the same used before for

the deposition of PEO/MWCNT solutions. PVDF solutions were deposited on three different types of reference substrates. The first one, was a non-conductive wire using the electrospinning set up showed in figure 4.3 of chapter 4. The second and the third reference substrates were aluminum foils arranged on a planar (figure 5.1 (a)) and drum collector, with a length of 22.5 cm and diameter of 10 cm (figure 5.1 (b)), respectively.

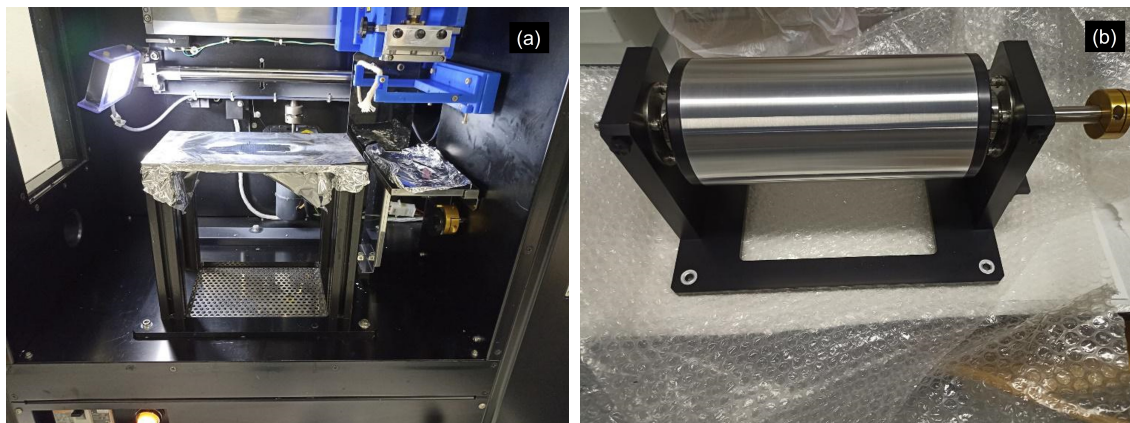


Figure 5.1: Reference substrate and type of collectors used during the PVDF nanofibers deposition: (a) planar and (b) drum collector.

5.2 Choosing electrospinning parameters for PVDF solution deposition

Electrospinning parameters for PVDF solutions deposition have been chosen to be able to make the piezoelectric response of the layer of the deposited nanofibers, as high as possible. Like it was extensively discussed in chapter 3 section 3.6, the piezoelectric response of PDVF is strictly correlated to the fraction of polar phases, in particular the β one, inside the sample. Indeed, electrospinning parameters have to be chosen in order to enhance the nanofiber stretching and alignment and, solvents evaporation [104], [105], [106], [107] (see chapter 3 section 3.6).

During these years, many researchers (see tables C.3 C.4 in appendix C) have tried to understand the influence of various electrospinning parameters on morphology, β phase fraction and therefore, on the piezoelectric response of PVDF nanofibers. In particular, many works in the literature focused their attention on the electric field that affect β phase fraction, defining a range of electric fields values between 0.5 kV/cm and 1.6 kV/cm. Moreover, it is evident that very often the value used as tip-to-collector distance is equal to 150 mm. Using a drum collector for the nanofiber deposition, the rotation speed was set equal to 50 rpm that corresponds to a tangential velocity of 0.27 m/s, in order to find if this tangential velocity was sufficient to favour the increase of the crystalline β -phase fraction inside the PVDF nanofiber mat. In line with all these considerations, in my project thesis, electrospinning parameters were also chosen in order to have a continuous polymeric jet,

during the electrospinning process, ensuring thus the formation of nanofibers mats, avoiding as much as possible electrospray process.

Finally, electrospinning parameters for the deposition of PVDF nanofibers on both planar (samples denominated with number '1') and drum (sample denominated with number '2') collector were chosen and shown in table 6.1. Particular attention, in this choice, was given to the electric field values used.

Samp.	Collector type	Applied voltage [kV]	Tip to collector distance [mm]	Feed rate [ml/h]	Rotation speed [rpm]	Spinneret width [mm]	Time of dep. [min]
1a	Planar	22	150	2	-	85	30
1b	Planar	26	120	2	-	85	30
1c	Planar	26	110	3	-	85	30
2a	Drum	22	150	2	50	85	120

Table 5.1: Electrospinning parameters used for PVDF deposition.

The deposition time was chosen in order to have a thickness of the electrospun nanofiber mat on the substrate to be able to perform both IR (see appendix A section A.3) and piezoelectric characterization. Indeed, the deposition of nanofibers on drum was done for a longer time (2h) than the planar one (30 min).

5.3 FT-IR characterization

Fourier Transformed infrared (IR) spectroscopy (see appendix A.1) was carried out with the main aim to verify the presence of β phase fraction and γ phase fraction, which are normally responsible for piezoelectric behaviour/properties [79]. FT-IR analyses was implemented for each of the samples previously realized. Moreover, a preliminary step was necessary to perform in a better way samples FT-IR characterizations. All spectra were baseline subtracted.

The FT-IR spectroscopy sample analysis was performed choosing a range of wavenumbers from 400 cm^{-1} to 1500 cm^{-1} , consistent with the wavenumbers of the three different crystalline phases of PVDF (α , β , γ) found in the literature (see tables C.3 and C.4 in appendix C). The FTIR plots for different samples are shown in figure 5.2, while in table 5.2 the wavenumber of the peaks belonging to the two different polar phases β and γ , are summarized. From the FTIR plots the peaks at 532 cm^{-1} and 761 cm^{-1} belong to the α -phase of the PVDF nanofibers. On the other hand, the larger peaks belonging to the β -phase at 510 cm^{-1} and 840 cm^{-1} highlight that most of the α -phase has been converted to the β -phase. Moreover, other peaks belonging to the β -phase at 445 cm^{-1} , 1274 cm^{-1} and 1430 cm^{-1} are present. The last one at 1430 cm^{-1} is present as a sort “knee” inside the spectra but more pronounced in sample 1a, indicating that probably the final β -phase peak formation was not finished. γ -phase peaks are present at 431 cm^{-1} and 1234 cm^{-1} . The last one is less pronounced for sample 1c, probably because the electric field used for the deposition of the PVDF nanofiber mat was too high with respect to the electric field

range used in literature (see table C.3). From all the FTIR plots, despite small differences in the position of some peaks in the different samples, it is still possible to observe in each of them the presence of peaks related to the two polar crystalline phases β and γ , which suggest a possible piezoresistive response to the application of an external stress.

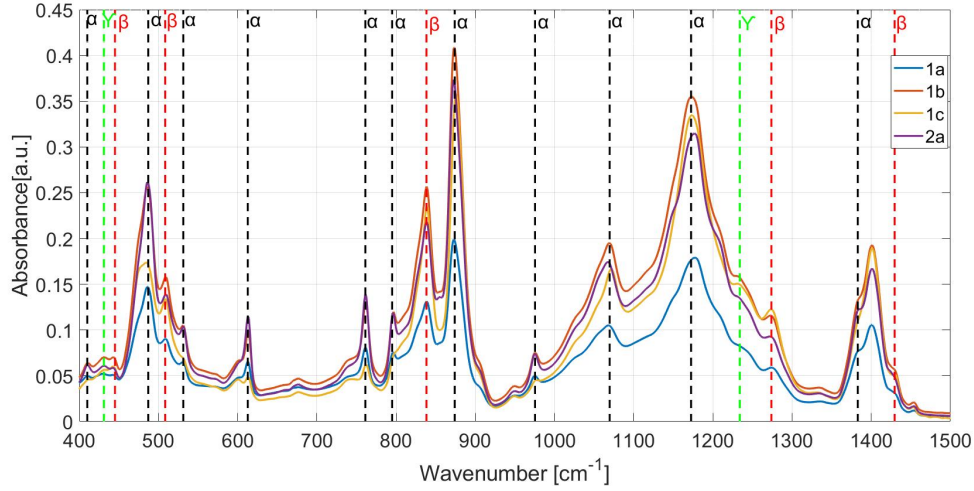


Figure 5.2: IR spectra of samples in planar (1a, 1b, 1c) and drum (2a) deposition configurations. The three different crystalline phases of PVDF nanofiber mat are highlighted in red for the β -phase, in green for the γ -phase and in black for the non-polar α -phase.

β -peaks [cm^{-1}]	γ -peaks [cm^{-1}]
445	431
510	1234
840	
1274	
1430	

Table 5.2: β and γ phases peaks position (wavenumber).

In figure 5.3 was taken a comparison between sample 1a and sample 2a. This was done because all the electrospinning parameters used for the realization of these two samples are the same except for the deposition time and configuration used, the first one planar (1a) and the second one on drum (2a).

It is important to notice that there is no difference between the spectrum obtained from the sample in which the layer of nanofibers was deposited in planar configuration (1a) and that on drum (2a). As mentioned in chapter 3 section 3.6.1, it could be expected to obtain more β peaks because the drum rotation speed can influences the nanofibers stretching

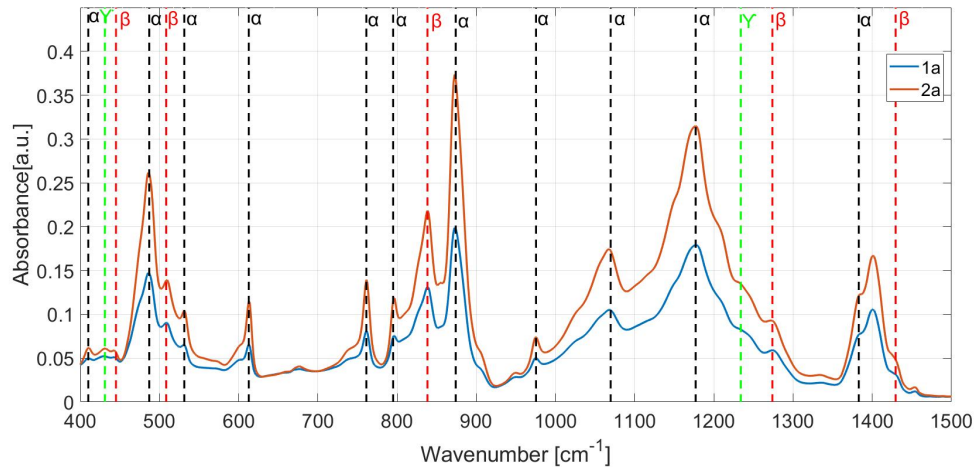


Figure 5.3: Comparison between IR spectra of samples 1a and 2a. The three different crystalline phases of PVDF nanofiber mat are highlighted in red for the β -phase, in green for the γ -phase and in black for the non-polar α -phase.

and alignment thus favoring the conversion of α peaks into β ones [105]. Probably, this was not obtained because the selected drum rotation speed was not the right one to improve this conversion.

5.4 Piezoelectric characterization

Ferroelectric polarization hysteresis loops, and piezoelectric displacement measurements were recorded simultaneously by a Piezo Evaluation System (PES, TFAalyzer 2000HS, Aixacct) coupled to a single point laser vibrometer (Polytec OVF-505), exploiting the converse piezoelectric effect (i.e., generation of a mechanical displacement under the application of an electric field). To perform the piezoelectric characterization of our samples, PVDF nanofiber were deposited on both planar and drum collectors using as substrate an aluminum foil on which a piece of polyimide-copper sheet was attached (figure 5.4).

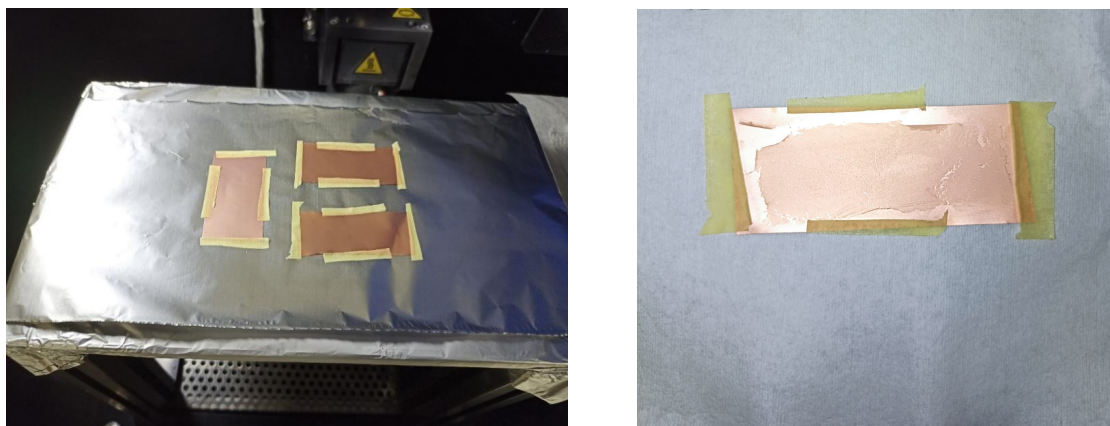


Figure 5.4: (Left) Kapton-copper sheet used as deposition substrate. (Right) Example of PVDF nanofiber deposition on a Kapton-copper sheet.

PVDF nanofibers are deposited on a polyimide-copper sheet in order to perform the piezoelectric characterization of nanofibers deposited on it. Polyimide-copper was used not only to guarantee a good mechanical conductance of the stress applied and a system able to deform without bringing to the rupture of the nanofiber mat deposited on it, but also as an electrical contact to perform the characterization. Moreover, the upper electrode was obtained by sputtering deposition.

By applying a voltage stimulus to the polymeric nanofiber mat with the piezo evaluation system, the ferroelectric hysteresis loops and the displacement loops were obtained.

All samples showed some piezoelectric response, confirming that the presence of β -phase peaks within the IR spectrum is related to the piezoelectric properties of the analyzed material. Among all the samples realized in planar configuration (1a, 1b, 1c), 1a is the one from which the piezoelectric response was analyzed. The results are shown in figure 5.5, in which the ferroelectric hysteresis loop, Polarization vs Voltage, and the displacement loop, Polarization vs Displacement, for sample 1a are shown. The reason for the better behavior shown by sample 1a, is probably due to the fact that the electric field used for the realization of sample 1a is equal to 1.46 kV/cm, the only one exactly inside the electric field range proposed in literature (see table C.3) (0.5 kV/cm – 1.6 kV/cm) which probably bring to an higher crystalline β phase fraction. However, what we expected from the piezoelectric analysis of the samples, was to get a better response from the sample made by depositing

the PVDF solution on the drum instead of the planar collector. This because, like previously exposed in chapter 3 section 3.6.1, the orientation of electrospun fibers obtained by using a rotating collector favours the conversion of the crystalline phase into the β one [105]. Probably, this was due not only to the selected drum rotation speed not perfect to emphasize this conversion, like previously said (see 5.3), but also due to the too low PVDF nanofiber mat thickness obtained [104] (see chapter 3 section 3.6.1).

In figure 5.5 the ferroelectric hysteresis loop, Polarization vs Voltage, and the displace-

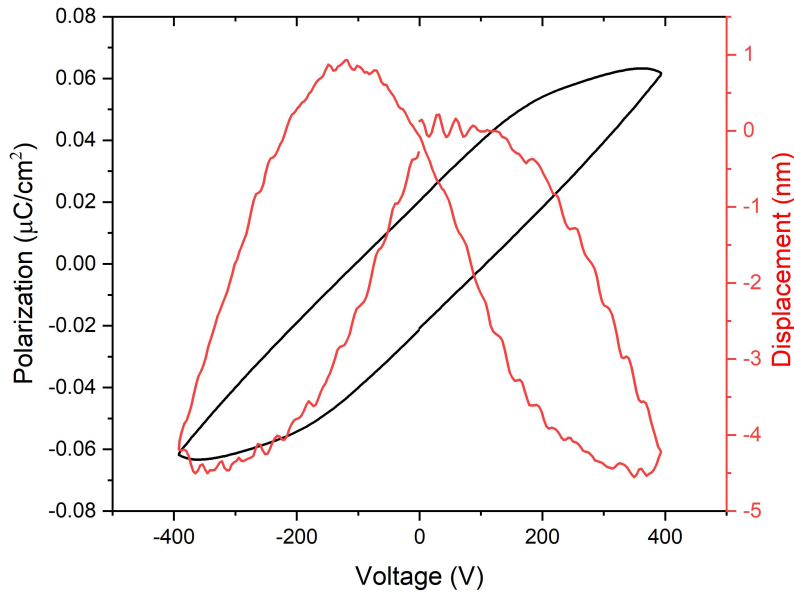


Figure 5.5: Ferroelectric hysteresis loop and the displacement loop of sample 1a.

ment loop, Polarization vs Displacement, loop obtained from sample 1a were shown. The graph shows an hysteretic behavior with a remanent polarization of about $0.02 \text{ } \mu\text{C}/\text{cm}^2$ and a coercive voltage of about 100 V, which highlights a piezoelectric response of the nanofibers mat. The value of the remanent polarization was comparable with the literature [127]. Together with the coercive voltage, the remanent polarization it's an important parameter of ferroelectric materials because determines the amount of polarization that remains in the material after the electric field removal (see chapter 2 section 2.3). The shape of the hysteresis curves tends to the rectangular shape of ideal ferroelectric materials but is slightly distorted by the presence of defects inside the sample, which increase its electrical conductivity worsening the ferroelectric properties [128]. As explained in the previous paragraph, the improvement of the ferroelectric response of the material, is linked to the fraction of β -phase inside the PVDF nanofiber mat, directly linked to the solution and electrospinning condition used during nanofiber deposition. Moreover, piezoelectric materials develop an electric voltage at their ends if they are deformed and vice versa, they deform if they are immersed in an electric field. Regarding the deformations induced by

the application of a certain electric field on the PVDF nanofiber mat, the displacement curve was obtained with a typical butterfly shape which is in accordance with displacement curves found in the literature [128] [129]. This displacement curve probably could be improved thanks to the reduction of the diameter of the deposited nanofibers, like it was demonstrated in the work of Bui, Tan Tan, et al. [129]. In this work, it was described that a reduction of the nanofiber diameter from 200 nm to 70 nm brings to an improvement of the shape of the butterfly displacement curve, finding a higher displacement with lower bias voltage applied for PVDF nanofibers with a diameter of 70 nm.

5.5 Repeatability

From the piezoelectric tests on samples 1a, 1b, 1c and 2a, sample 1a was found to be the one with a better piezoresistive response. In order to confirm the repeatability of the deposition, we have made six different replicas of sample 1a. These replicas were obtained using the same electrospinning parameters but with different solutions, all obtained using the same PVDF, the same binary mixture of the two solvents DMF/acetone and the same procedure used before and described in the first section of this chapter.

The infrared spectroscopy sample analysis was performed in the way described in appendix A section A.3. The FTIR plots for different replicas are shown in figure 5.6 together with that of the sample 1a previously analyzed.

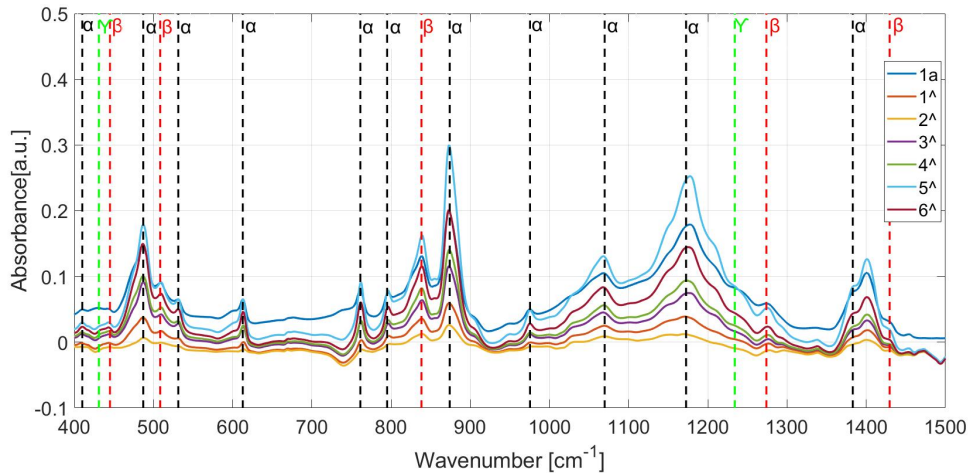


Figure 5.6: Comparison between IR spectra of samples 1a and all the six replicas. The three different crystalline phases of PVDF nanofiber mat are highlighted in red for the β -phase, in green for the γ -phase and in black for the non-polar α -phase.

From the FTIR plots obtained, it is possible to confirm the repeatability of the deposition. Indeed, all the spectra have the same profile and the same position of the peaks, in particular those related to the two polar phases β and γ .

However, what we expected from the piezoelectric analysis of the samples, was to get a better response from the sample made by depositing the PVDF solution on the drum instead

of on the planar collector. Like said before, this was probably due to the drum rotation speed used during the PVDF nanofibers deposition. In order to eliminate any doubt that the piezoelectric response of the sample obtained by deposition on drum was also influenced by the deposition time, a second sample was made, using the same electrospinning parameters of sample 2a but with a longer deposition time, i.e. instead of two hours, three hours of deposition. The FTIR spectrum obtained by these two samples obtained with two different deposition times, are shown in figure 6.1. Looking closely at the two curves

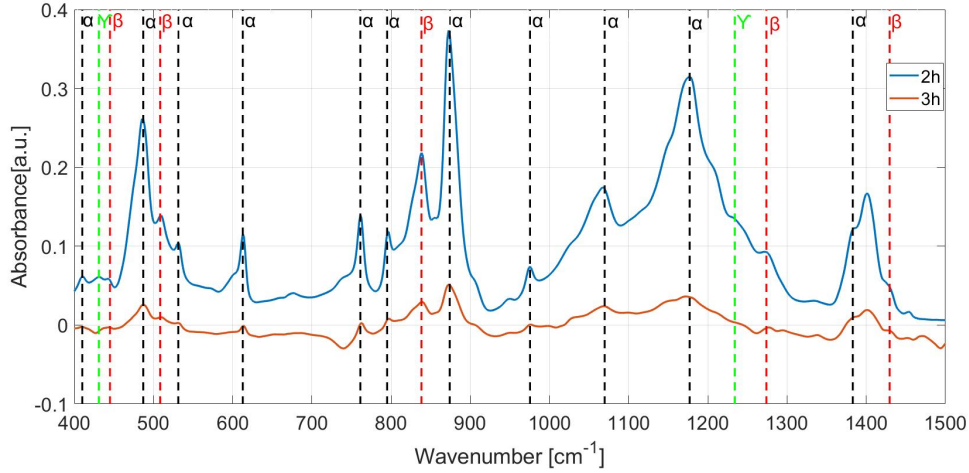


Figure 5.7: Comparison between IR spectra of samples realized with drum collector for 2h and 3h of deposition. The three different crystalline phases of PVDF nanofiber mat are highlighted in red for the β -phase, in green for the γ -phase and in black for the non-polar α -phase.

of figure 6.1, it is noted that the spectra obtained from the samples by deposition of the PVDF solution on drums with different deposition times, turn out to be of the same type. Indeed, the position of the peaks, in particular those related to the two polar phases β and γ , are the same. This is a demonstration of the fact that, the deposition time, and therefore the thickness of the PVDF nanofiber mat, does not affect in any way the IR spectrum obtained, as is also demonstrated in the literature [105]. Indeed, like previously said, the PVDF nanofiber mat thickness has an effect only on the energy conversion of the PVDF nanofiber-based device [104].

Chapter 6

Fututure developments

In this section it is described a possible strategy for a future realization of an all-nanofibers flexible sensing able to combine both piezoelectric and piezoresistive mechanisms. This is introduced in order to give the possibility to realize a flexible sensor able to detect static and highly dynamic signals integrating both piezoresistive and piezoelectric nanofibers in the same sensing unit by a layer-by-layer approach.

This approach consists in the realization of a nanostructured core based on composite nanofibers of PEO/MWCNTs, covered by a piezoelectric nanofiber layer, made of PVDF, as represented in figure 6.1.

To realize a core based on composite nanofibers of PEO/MWCNTs, a polymeric solution

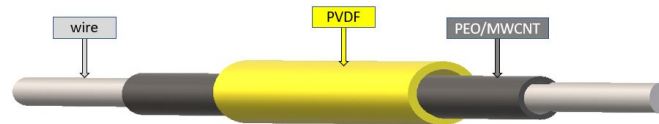


Figure 6.1: Schematic representation of the “layer-by-layer” deposition.

of 3.5 wt% MWCNTs and 5wt% PEO was prepared, like described into chapter 4. This solution was initially deposited on a non-conductive wire. Subsequently, a PVDF solution was electrospun and deposited onto nanostructured core. The electrospinning parameters used for these two electrospinning depositions, are shown in table 6.1.

Solution type	Applied voltage [kV]	Tip to collector distance [mm]	Feed rate [ml/h]	Rotation speed [rpm]	Spinneret width [mm]	Deposition time [min]
PEO/CNT	29.5	145	0.5	100	70	20
PVDF	26	145	1.5	50	15	5

Table 6.1: Electrospinning parameters used.

The spinneret width electrospinning parameter, defined as the travelled distance from the center of the collector by spinneret, is strictly correlated with the length of final samples. In this case, with the main target to cover only a region of PEO/MWCNTs nanofibers with PVDF nanofibers, two different spinneret width values were defined: 70 mm for PEO/MWCNT solution and 15 mm for PVDF solution. In this way, the presence of conductive composite nanofibers at the extremities of insulator yarn is guaranteed and an electrical characterization can be performed.

The electrical characterization was done using the same benchtop digital multimeter used for all the previous electrical characterizations (see 4 section 4.1). A bias voltage of 1V was applied firstly, at the extremities of the wire, named in figure 6.2 “External part”, and secondly, at the extremities of the PVDF nanofiber layer, named in figure 6.2 “Internal part”. Electrical current values were measured for a certain time interval corresponding to the acquisition of 100 values.

From figure 6.2 it is possible to see that, current measured in the “Internal part”, the one where PVDF nanofiber are present in the external layer, is much lower than the one measured in the “External part”, where we have only PEO/MWCNT nanofiber deposited. This gives us the demonstration of the fact that the electrospinning system can be used for a layer-by-layer deposition, of a layer of non-conductive nanofibers on a layer of conductive ones. From the electrical characterization performed, it is possible to deduce that there is no electrical interaction between these two layers.

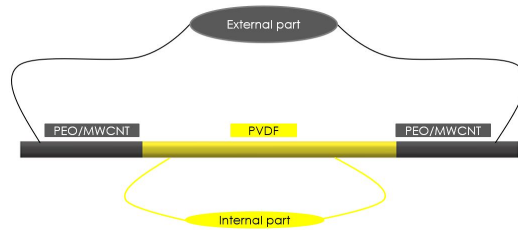


Figure 6.2: Schematic representation of the electrical characterization set-up.

In order to understand if the Ohmic behavior was present or not, for both internal and external part the I/V characteristics were made, setting a voltage varying from -10V to 10V and measuring the corresponding current in a number of point which have been set to 600. From figure 6.4 it is possible to verify that the linear Ohmic trend is present, with a electrical resistance value of the external part (PEO/MWCNT) equal to $R_{external} = 4.27 \cdot 10^6 \Omega$ much lower than the internal (PVDF) one $R_{internal} = 6.96 \cdot 10^9 \Omega$. Moreover, the resistance value obtained for the external part (PEO/MWCNT) is comparable to the one previously obtained in chapter 4 for the solution at 3.5 wt% conductive filler weight percentage (see table 4.2). This is a demonstration of what previously said about the absence of electrical interaction between these two layers.

This preliminary study of this layer-by-layer configuration of deposition lays the foundations for the future development of a sensor capable of combining the piezoresistive effect with the piezoelectric one, with all the advantages linked not only to nanostructuring (see chapters 1 and 2), but also to use a versatile and low-cost nanostructuring method such

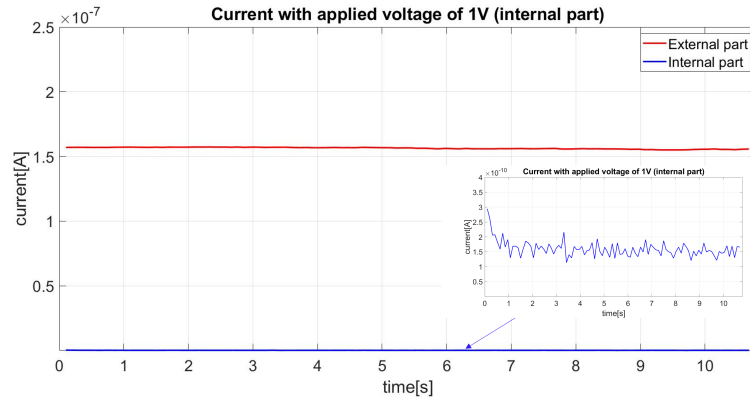


Figure 6.3: Current values obtained setting a bias voltage equal to 1V for the “External part” (red curve) and the “Internal part” (blue curve).

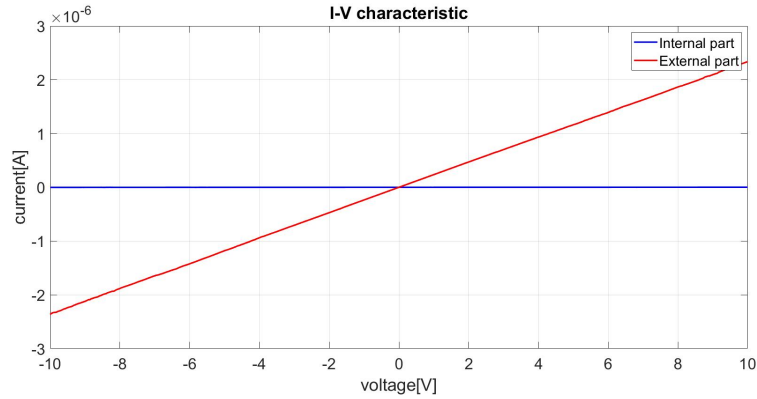


Figure 6.4: I/V curves for the “External part” (red curve) and the “Internal part” (blue curve).

as electrospinning. In future, this layer-by-layer configuration could be realized on all the different type of deposition substrates used in this thesis to match the requirements of the application.

Moreover, the future realization of this sensing unit could be improved trying to enhance the ferroelectric response of the PVDF "Internal part", for example by changing some electrospinning deposition parameters such as the rotation speed. Like previously said the correct choose of the wire rotation velocity could bring to an enanchment of the nanofiber alignment, favoring the conversion of the α into β crystalline phase. In the work of Ahn, Yongjin, et al. [127] it is showed another possibility to improve the PVDF nanofiber mat piezoelectric response. In this work it was demonstrated that the addition of MWCNTs inside the PVDF polymer matrix further enhance the ferroelectric properties and the value of the remanent polarization is increased. This is due to the promotion of the conversion of the PVDF α -phase into the β -phase because they behave like nuclei in the crystallization

process and induce charge accumulation at the interface [127].

Another possible improvement of this thesis work with the final aim of realizing this layer-by-layer configuration, could be produced by studying the piezoresistive response of the PEO/MWCNT layer using a more accurate electrical contacts and set-up of analysis, perhaps using more and even higher pressure values in such a way as to construct a resistance-pressure curve that includes all three regions mentioned in the literature [130], [131].

In future it could also be useful to study the behavior of the various deposition substrates, in particular the tubular one, used in this thesis work to better understand the actual deformation induced on the nanofiber mat under the application of a certain external stimulus. A preliminary literature review was performed trying to compare the tubular shape used in this thesis with a very similar shape like the one of blood vessels [133], [134].

Chapter 7

Conclusions

In conclusion, the main aim of this work is the design and optimization of electrospun polymeric nanofibers, developed as sensitive materials of piezoresistive and piezoelectric flexible sensors. This work demonstrates that not only electrospinning is an effective method to fabricate functional nanomaterials for pressure and strain flexible sensors, but it also offers several strategies to adapt and tune the final architecture of the functional nanomaterials, to match the requirements of the application (e.g., integration in smart-textiles, design of wearable sensors).

Electrospun composite nanofibers, based on PEO/MWCNTs, were optimized to develop a suitable piezoresistive materials, while, on the other hand, PVDF nanofibers were investigated for their piezoelectric properties. From a piezoresistive point of view, obtained results allowed confirming the percolative behavior of PEO/MWCNTs composite nanofibers, regardless of the collectors' architecture. Furthermore, the analysis of piezoresistive responses, achieved when two composite nanofibers, containing a wt% of MWCNTs close to percolation threshold and one wt% MWCNTs far from it, confirmed a certain piezoresistive response, comparable with one exposed in the literature.

The main result obtained from the analysis of electrospun composite nanofibers of CNTs/polymer demonstrated and confirmed their percolative behaviour, also if final nanofiber' mats were directly collected on a substrate, wire and tubular shapes, that showed a geometrical configuration different from the common planar architecture. Moreover, performing a preliminary analysis of two samples with conductive filler weight percentages close to the percolation threshold and above and far from it, a certain piezoresistive response was obtained, in accordance with literature.

On the other hand, the main results obtained from the analysis of PVDF electrospun nanofiber mats on a planar and drum collector, was the IR spectra of different samples realized by using different electrospinning parameters, which were consistent with previous works found in literature, confirming the presence of the polar β -phase, linked to its piezoelectric properties. Moreover, thanks to the use of a Piezo Evaluation System, the ferroelectric hysteresis loop, and the displacement loop were obtained from one of the realized samples, confirming that the presence of β -phase peaks within the IR spectrum was related to the piezoelectric properties of the analyzed material.

Since one of the main goal was to develop an all-NFs flexible sensing platform, able to combine both piezoelectric and piezoresistive mechanisms, a possible strategy was designed and

applied.

Appendix A

Instruments of analysis

In this section a brief description of the principal instrument used in this thesis for the analysis is presented. In the next chapters the different uses of each of these instruments is explained.

A.1 Optical microscope

An optical microscope is a microscope based on optical lenses and it can produce a magnification of samples or detail of them, too small to be observed with human eye. The optical microscope works with visible light with a wavelength between infrared and ultraviolet. This type of microscope, by means of a system of lenses, enlarges the image of the sample, collecting the visible light reflected (reflection configuration), transmitted (transmission configuration) or emitted by the sample itself (figure A.1).

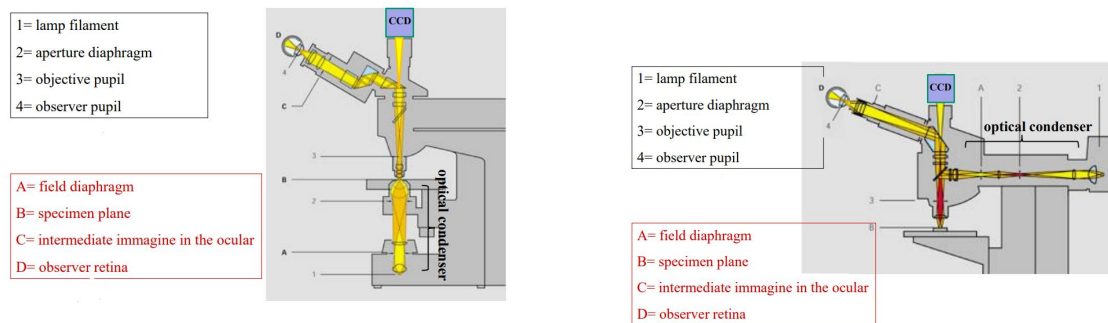


Figure A.1: Scheme of an optical microscope operating in reflection (right) and transmission (left) [110].

Three parameters define the efficiency of an optical microscope: magnification, resolution power and diffraction.

Magnification is defined as the ratio between the dimensions of the original object, and

those of the image obtained. The magnification of a microscope cannot be indefinitely increased since the diffraction phenomenon. Indeed, the objective diffraction limits the smaller distance between two objects allowing distinct images, so limiting the magnification.

The resolution power is defined as the minimum distance between two points that the microscope allows to observe distinct. Unfortunately, the resolution power is limited by the diffraction phenomenon. The resolution power of the microscope can be expressed thanks to the formula $r = 0.61 \cdot \lambda / AN$ where λ is the wavelength of the used light source and AN is the objective numerical aperture.

To achieve higher resolutions, it is necessary to use smaller wavelengths, such as in the X-ray microscope, or, taking advantage of the equivalence between waves and particles defined by quantum mechanics, using electrons (electronic microscope) whose wavelength equivalent is much smaller than that of visible light.

So, in some cases it is convenient to use electron microscopy instead of optical microscopy, it depends on what it is necessary to study. In the table below the advantages of electron microscopy over optical one is showed, but the optical microscope is cheaper with respect to an electron microscope.

	MAGNIFICATION	RESOLUTION
Optical microscopy	4x-1000x	$\sim 0.5\mu m$
Electron microscopy	20x-106x	$< 10^{-3}\mu m$

Table A.1: Advantages over optical microscopy [110]

A.2 FESEM

FESEM stands for Field Emission Scanning Electron Microscopy, and it is an instrument that belongs to the optical microscopy. Like SEM (Scanning Electron Microscopy), it gives us a very wide variety of information from the sample surface that is scanned with an electron beam while a monitor displays the information of user interest on the basis of detectors available. Accelerated electrons interact with the sample atoms producing different types of signals: secondary electrons, reflected or back-scattered electrons, X-rays and light (cathodoluminescence). For each of these signals it is present a detector inside the FESEM apparatus. Samples in the FESEM (figure A.2 (a)) are observed in high vacuum because gas molecules tend to disturb the electron beam and the emitted secondary and backscattered electrons used for the analysis.

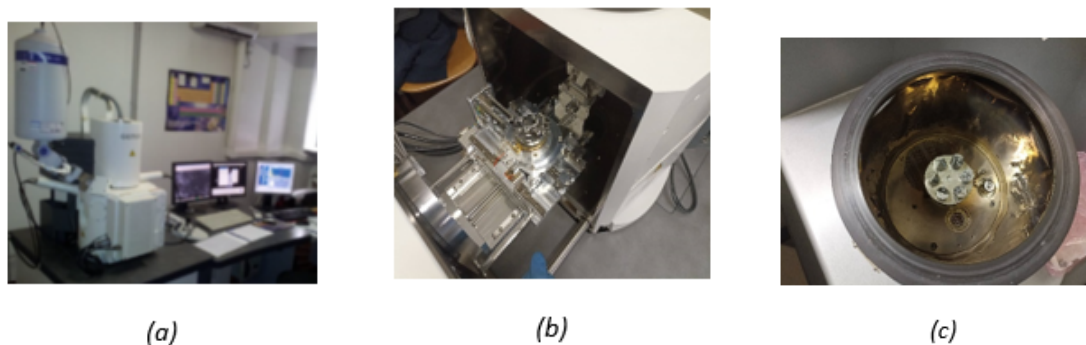


Figure A.2: a) FESEM of Polytechnic of Turin laboratory, (b) FESEM sample holder, (c) sample preparation before the FESEM analysis.

FESEM samples must be small enough to be putted in the sample holder, and they need a previous preparation to increase their electrical conductivity and to maintain them stable during the analysis because they must withstand the high vacuum conditions and the high energy beam of electrons. In order to enhance their stability, samples are generally mounted rigidly on a specimen holder or stub using a conductive adhesive (figure A.2 (b)). If it is required to analyze nonconductive or very low conductive samples, it is necessary to cover them with a conductive film like platinum, gold, palladium, but without producing damages on their surface. For example, in our analysis samples are covered with platinum by low-vacuum sputtering (figure A.2 (c)). This step must be done because of the charge-up effect; when an insulator is irradiated with a primary electron beam, electrons tend to localize on its surface. To reduce it a conductive ultra-thin film is deposited on the sample surface to obtain a sort of short circuit between the sample surface and the sample holder which is conductive. Connecting the sample holder to the ground of the system, the impinging primary beam has a certain high mobility on the surface which can be discharged exploiting to the sample holder connected to the ground.

FESEM shows higher resolution and much greater energy range with respect to SEM. FESEM makes use of in-lens detectors. These detectors are optimised to work at high resolution and low acceleration potential and are fundamental for getting the maximum performance from the equipment.

The biggest difference between FESEM and SEM systems lies in the electron generation system. FESEM uses a field emission gun that provides extremely focused high and low energy electron beams, which improves spatial resolution and allow to work at very low potentials. This reduces the charging-up effect for non-conductive samples and helps to avoid damage to electron beam sensitive samples.

A.3 FT-IR

Fourier-transform infrared spectroscopy (FTIR) is a particular type of IR spectroscopy [111]. IR spectroscopy is an absorption technique that works with electromagnetic radiation in the infrared region. IR is a vibrational spectroscopy technique. The basic idea behind any vibrational spectroscopy is the observation of how light is scattered or absorbed when

reaches the material.

As a general approximation, the energy levels of electrons in a molecule can be divided into three classes: rotational, vibrational, and electronic energy levels. The absorption of infrared radiation brings about changes in molecular vibration within molecules. So, a molecule can be excited to a higher vibrational state when absorbs infrared radiation. In general, the frequency at which a particular bond absorbs the radiation depend on atom size, bond length and bond strength. The absorption of the infrared photon occurs only if it has a sufficient energy for the transition to the next allowed vibration energy state and when the infrared radiation interacts with a molecule bringing to a permanent change in dipole.

FTIR differently from simple IR spectroscopy, uses not a monochromatic beam of light toward the sample, but a beam containing many frequencies of light at once and measures how much of the beam is absorbed by the sample. The Fourier transform is needed to transform the signal from the time domain to the frequency domain. The produced final spectrum can give both qualitative and quantitative information. Absorbed wavelengths are due to the chemical groups present in the sample. The absorption intensity at a particular wavelength is related to the concentration of the chemical group that absorbs this wavelength.

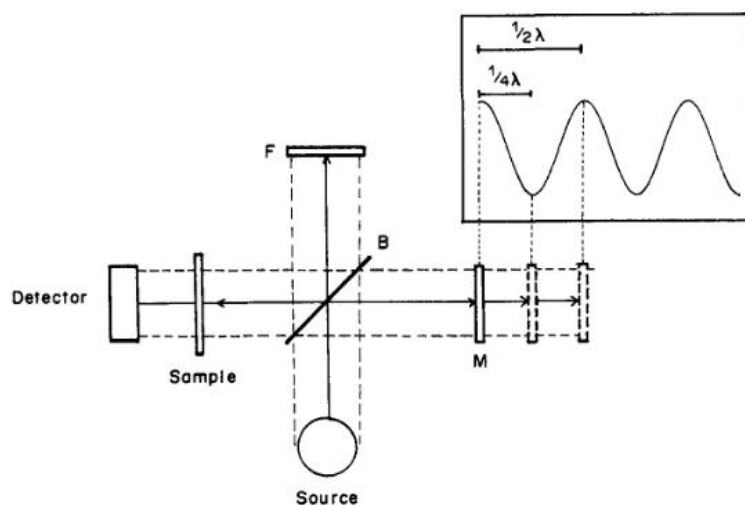


Figure A.3: Schematic representation of the Michelson Interferometer. Reprinted from [111], Copyright (1993), with permission from Elsevier.

FTIR spectrometers are based on the Michelson Interferometer (figure A.3). Indeed, FTIR produce an interferometric pattern that reaches the detector after passing through the sample. A light source emits a light beam in the infrared region; this beam reaches a semi-reflective mirror, called beamsplitter, that divides it into a 50% toward a fixed mirror (F) and 50% toward a moving mirror (M). Rays reflected by these mirrors are sent again to the beamsplitter (B) which reunites the two rays and sends them to the detector passing through the sample. Even if the two rays reached the detector together, they made

a different optical path. Depending on this difference in the optical path, constructive or destructive interferences can occur, creating a signal proportional to the difference in the optical path of the two rays and to the position of the moving mirror. The produced signal, the interferogram, is a plot of intensity vs optical path difference or mirror movement. The interferometric data from this time domain is then Fourier transformed into the frequency domain.

To sum up, FTIR is a very diffused technique that gives us information about the type of molecules present in the sample, thanks to identification of molecular bonds. It is a very versatile technique, that gives the possibility to study organic, inorganic, biological, liquid, solid and gaseous samples. Thanks to the FTIR spectrum it is possible to obtain qualitative and quantitative information with very high accuracy and precision. Moreover, because all the frequencies are measured simultaneously, the generation of the spectrum is very fast.

Appendix B

Deposition of PEO/MWCNT solutions at different CNTs weight percentages.

The deposition of solutions prepared at different weight percentages of MWCNT with respect to PEO was performed using electrospinning parameters relative to sample “BW2” as reported by table 4.1 of Chapter 4 but with a longer time of deposition of 40 minutes, to have a greater amount of nanofibers deposited for a better electrical characterization. Like said in chapter 4 section 4.1, the different solutions were deposited on a hollow wire of a heat shrinkable material with a length equal to 9 cm.

Figure B.2 showed the I/V curve of all the realized samples in order to understand if

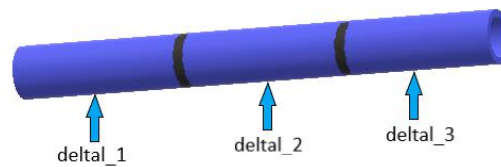


Figure B.1: Schematic representation of the hollow wire division in segments for multimeter data acquisition.

the Ohmic behavior is respected. Moreover, for each sample the I/V curve was plotted at different sample locations (figure B.1), in order to take into account the possibility to have a non-perfect uniform deposition over the entire sample length. In this way the final conductivity value is the result of an average on conductivity values calculated in different segments of the sample under test.

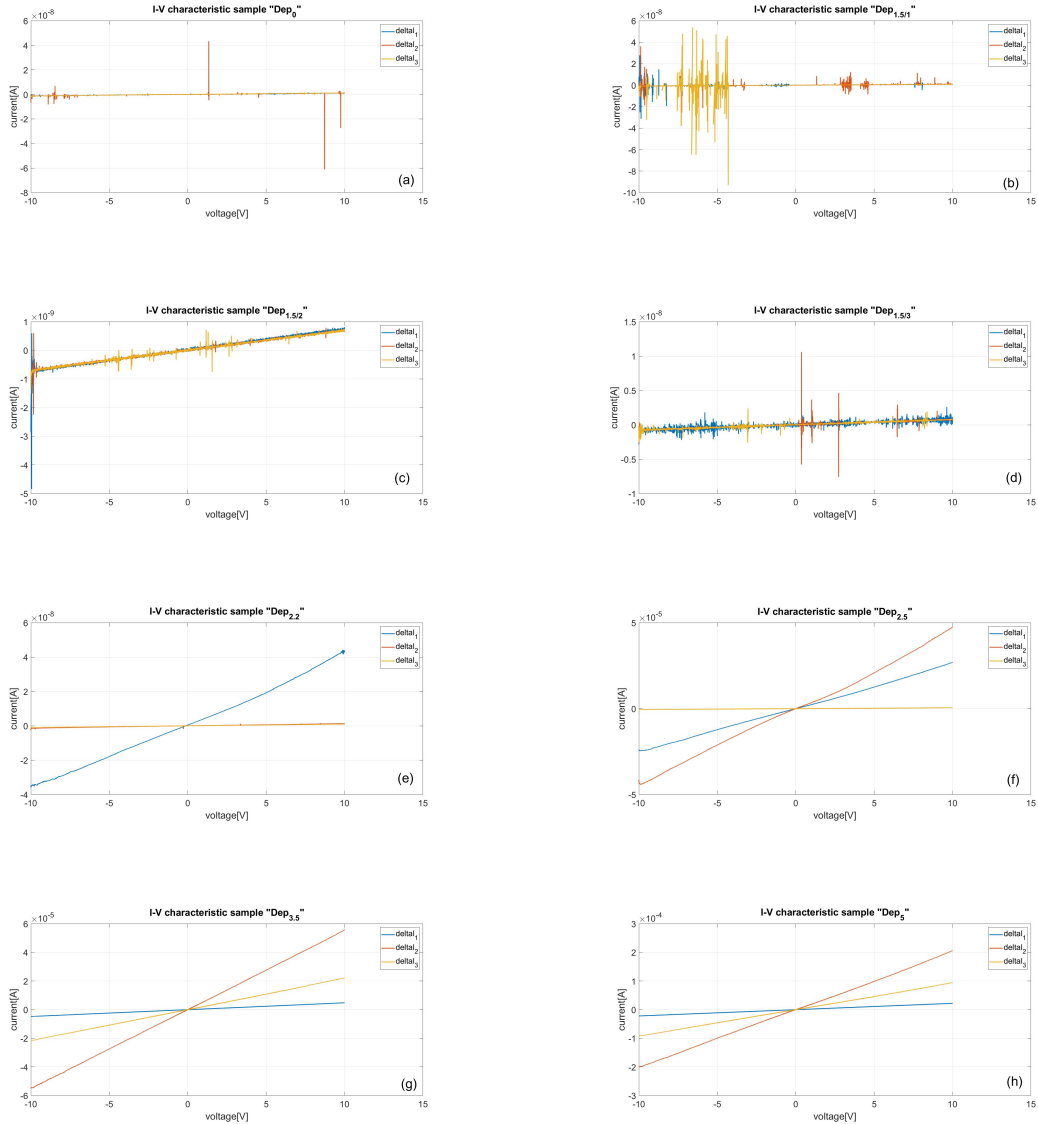


Figure B.2: I/V curves of samples at different MWCNT weight percentages for different sample locations: (a) sample with 0 wt%, (b), (c), (d) samples with 1.5 wt%, (e) sample with 2.2 wt%, (f) sample with 2.5 wt%, (g) sample with 3.5 wt% and (h) sample with 5 wt%.

Looking at the I/V curves related to the different samples, it can be seen that the linear trend is almost respected. However, in samples containing a weight percentage of MWCNT less than or equal to 1.5 wt% (figure B.2 (a), (b), (c) and (d)), the presence of a significant amount of noise is observed, since these samples, being poorly electrical conductive, are affected by the background noise of the multimeter during the measurement of the current. In addition, in all the other samples (figure B.2 (e), (f), (g) and (h)), the I/V characteristic made for the different Δl 's turns out to have different slopes, indicating that, probably in some substrate' regions, there is a greater amount of composite nanofibers than in other

segments of the same sample. In table A.1 are shown the electrical resistance values of each sample and for each Δl , calculated as the slope of the I/V curve. The solution containing a 1.5wt% of MWCNTs was tested 3 times, obtaining also three comparable different nanofiber' mats, since this MWCNTs' amount could be close to the percolation threshold, as already demonstrated by Massaglia Massaglia, et al. [46].

wt%	Sample	Δl_1 [cm]	Δl_2 [cm]	Δl_3 [cm]	$R_{\Delta l_1}[\Omega]$	$R_{\Delta l_2}[\Omega]$	$R_{\Delta l_3}[\Omega]$
0	Dep_0	1.4	2	1.5	$8.49 \cdot 10^9$	$8.70 \cdot 10^9$	$8.10 \cdot 10^9$
1.5	$Dep_{1.5/1}$	1.35	2.1	2.4	$1.19 \cdot 10^{10}$	$1.12 \cdot 10^{10}$	$1.06 \cdot 10^{10}$
1.5	$Dep_{1.5/2}$	2	2.2	2.2	$1.32 \cdot 10^{10}$	$1.43 \cdot 10^{10}$	$1.43 \cdot 10^{10}$
1.5	$Dep_{1.5/3}$	2	2.2	1.6	$1.24 \cdot 10^{10}$	$1.30 \cdot 10^{10}$	$1.29 \cdot 10^{10}$
2.2	$Dep_{2.2}$	1.6	2.35	2.5	$2.59 \cdot 10^8$	$7.45 \cdot 10^9$	$1.11 \cdot 10^{10}$
2.5	$Dep_{2.5}$	1.8	1.2	2.8	$3.91 \cdot 10^5$	$2.27 \cdot 10^5$	$1.96 \cdot 10^7$
3.5	$Dep_{3.5}$	1.9	2.65	2.5	$2.10 \cdot 10^6$	$1.81 \cdot 10^5$	$4.60 \cdot 10^5$
5	Dep_5	1.85	2.05	1.85	$4.54 \cdot 10^5$	$4.97 \cdot 10^4$	$1.08 \cdot 10^5$

Table B.1: Electrical resistance values for each sample with different MWCNT weight percentages and for each Δl .

The samples electrical characterization was performed again using the set-up shown in figure B.3, where the electrical contacts were realized through metallic contact plates. To define the electrical conductivity values for each sample and for each Δl , the nanofiber

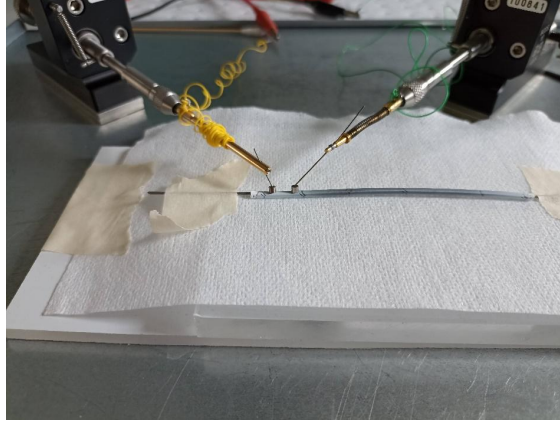


Figure B.3: Set up for a more accurate electrical characterization of our samples.

mats' cross-section S was defined, considering also the geometry of substrate on which nanofibers were directly collected, as reported in equation B.1.

$$S = \pi((R + r)^2 - R^2) \quad (\text{B.1})$$

where $R = 1.375$ mm represents the outer radius of the hollow wire, while r is the nanofiber mat thickness deposited on it. To better assess the value of r , each sample was carefully

cut into three pieces so as not to damage the layer of nanofibers deposited. Subsequently, thanks to the use of the optical microscope and of a tool that was able to keep the sample in upright position (figure B.4 (Left)), different values of r were measured in different sample's locations. At the end, for each sample the final value of r was evaluated as an average of all the measured thickness values. In this way any non-uniformity of deposition can partly be taken into account.



Figure B.4: (Left) Set up used for nanofiber mat thickness. (Right) Schematic representation of a sample cross section.

In table B.2 the thickness values of the layer of deposited nanofibers and the corresponding calculation of the sections are shown. It can be immediately noticed that samples $Dep_{2.2}$ and $Dep_{2.5}$ have an average thickness one order of magnitude greater with respect to all the other samples. This can be explained thanks to the electrical resistance values calculated in these two samples for different Δl shown in B.1. Indeed, in sample $Dep_{2.2}$ the three electrical resistance values related to the three different Δl vary by one or two orders of magnitude relative to each other, leading thus to suppose how a greater thickness of nanofibers' layer affects the calculation of the average thickness $r_{average}$. This non uniform nanofiber deposition along the wire could be justified by the fact that these sample, containing a weight percentage of MWCNT very close to the percolation threshold have a less stable behavior during the electrospinning deposition than solutions well below or above percolation.

wt%	Sample	$r_{average} [\mu m]$	$S [cm^2]$
0	Dep_0	3.9	$3.4 \cdot 10^{-4}$
1.5	$Dep_{1.5/1}$	3.1	$2.7 \cdot 10^{-4}$
1.5	$Dep_{1.5/2}$	3.4	$2.9 \cdot 10^{-4}$
1.5	$Dep_{1.5/3}$	3.8	$3.3 \cdot 10^{-4}$
2.2	$Dep_{2.2}$	15.5	$1.3 \cdot 10^{-3}$
2.5	$Dep_{2.5}$	67.2	$5.9 \cdot 10^{-3}$
3.5	$Dep_{3.5}$	5.1	$4.4 \cdot 10^{-4}$
5	Dep_5	4.1	$3.5 \cdot 10^{-4}$

Table B.2: Evaluation of nanofiber mat cross section.

In order to be sure that the thickness values of the nanofiber layer measured with the optical microscope were correct these values were compared with the ones obtained by analyzing FESEM (Appendix A.2) images, represented in figure B.5. FESEM images allowed confirming how measured thickness results to be in line with the ones estimated by analyzing optical microscope images. For this reason, the section values used in the final calculation of conductivity were those obtained from the measurement by optical microscope, shown in the table B.2.

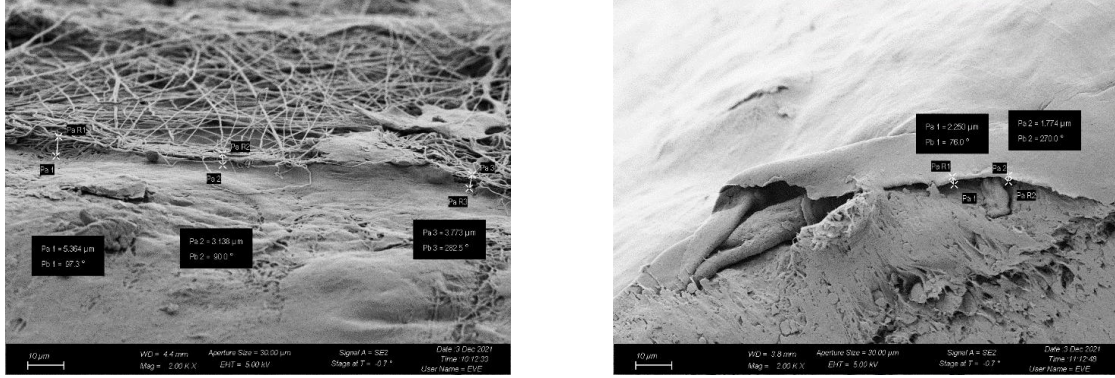


Figure B.5: (Left) FESEM image of sample $Dep_{1.5/3}$. (Right) FESEM image of sample $Dep_{3.5}$

To obtain the final implementation of the percolation curve, conductivity values are calculated for each sample and for each Δl , thanks to the electrical resistance values previously calculated and shown in table B.1 and using the values of cross-section S , obtained with the measurement of the nanofiber mat thickness shown in table B.2. In Table B.2 these values of conductivity are summarized.

wt%	Sample	$\sigma_{\Delta l_1}$ [S/cm]	$\sigma_{\Delta l_2}$ [S/cm]	$\sigma_{\Delta l_3}$ [S/cm]
0	<i>Dep₀</i>	$4.79 \cdot 10^{-7}$	$6.68 \cdot 10^{-7}$	$5.38 \cdot 10^{-7}$
1.5	<i>Dep_{1.5/1}</i>	$4.23 \cdot 10^{-7}$	$6.94 \cdot 10^{-7}$	$8.38 \cdot 10^{-7}$
1.5	<i>Dep_{1.5/2}</i>	$5.17 \cdot 10^{-7}$	$5.26 \cdot 10^{-7}$	$5.26 \cdot 10^{-7}$
1.5	<i>Dep_{1.5/3}</i>	$4.89 \cdot 10^{-7}$	$5.13 \cdot 10^{-7}$	$3.75 \cdot 10^{-7}$
2.2	<i>Dep_{2.2}</i>	$4.56 \cdot 10^{-6}$	$2.33 \cdot 10^{-7}$	$1.67 \cdot 10^{-7}$
2.5	<i>Dep_{2.5}</i>	$7.72 \cdot 10^{-4}$	$8.90 \cdot 10^{-4}$	$2.41 \cdot 10^{-5}$
3.5	<i>Dep_{3.5}</i>	$2.06 \cdot 10^{-3}$	$3.32 \cdot 10^{-2}$	$1.24 \cdot 10^{-2}$
5	<i>Dep₅</i>	$1.17 \cdot 10^{-2}$	$1.19 \cdot 10^{-1}$	$4.92 \cdot 10^{-2}$

Table B.3: Electrical conductivity values for each sample with different MWCNT weight percentages and for each Δl .

The final conductivity values were obtained as an average of the three electrical conductivity values in each of the three different Δl for each sample. Only for the solution which contains MWCNT with a weight percentage equal to 1.5 wt% three samples were realized. So, the final conductivity for MWCNT weight percentage equal to 1.5 wt% is obtained by the average of the conductivity values of each of these three samples.

Appendix C

Electrospinning parameters for PVDF deposition in literature

Wire number of α -phase[cm^{-1}]	Wire number of β -phase[cm^{-1}]	Wire number of γ -phase[cm^{-1}]	Ref.
1182 1073 878 765	841 1280	-	[119]
489 532 613 762 795 975	475 510 840 1275	483 512 838 1234	[120]
761	840 1274	-	[104]
613 763	840 1275	-	[106]
-	510 840 1279	776 881 1236	[121]
530 612 760 796 970	510 840 1274 1430	-	[122]
410 854 489 975 532 1149 614 1209 763 1383 795 1432	445 473 1275 1431 510 840	431 482 811 1234 1429	[123]
766	840	-	[124]
766	840 1275	1234	[125]
614 766 795 975	510 840 1279	-	[126]

Table C.4: Wavenumbers of α , β , and γ peaks of infrared spectra from literature.

Material	Solvents	Stirring	Collector Type	RH [%]	T of dep. [°C]	Time of electro-spinning	Voltage [KV]	Dist. [mm]	Flow Rate [ml/h]	Rot. Speed [rpm]	Ref.
PVDF pellets; (M _w =172000); 10 wt%	DMF-ACETONE (4/6 v/v)	2h at 70°C	Cylindrical drum collector (l=40cm d=20cm)	40	20	-	14;16;18; 20;22;24	150	0.5;1;1.5 2;3	300	[119]
PVDF powder (M _v =534000); 16 wt%	NMP-ACETONE (5/5 v/v)	-	Vertical electro-spinning setup	55-60	30	-	7.5	100	0.08	-	[120]
PVDF pellets (M _v =275000); 16-26 WT%	DMF-ACETONE (4/6 v/v)	-	Rotating drum collector (l=10cm d=5cm)	-	Ambient	Varied to control the mat thickness	15	150	1	100	[104]
PVDF powder (M _v =550000); 10,14,18 wt%	DMF-ACETONE (50:50 wt%)	0.5h at 70°C	Rotating cylindrical drum collector covered by a 30x30cm sheet of aluminum foil	-	Ambient	Varied to produce fiber mats of five different basis weight (10,20,30, 40 and 50) g/m ²	27	200	5	30	[106]

Table C.1: Electrospinning parameters used for PVDF deposition in literature.

Material	Solvents	Stirring	Collector Type	RH [%]	T of dep. [°C]	Time of electro-spinning	Voltage [KV]	Dist. [mm]	Flow Rate [ml/h]	Rot. Speed [rpm]	Ref.
PVDF granules (Mv=275000, size 5mm); 12 wt%	DMF-ACETONE (7:3)	70°C until the solution transparent and homogeneous	Rotating drum collector	-	Ambient	10h	20	150	0.02	-	[121]
PVDF (Mw=275000); 24 wt%	DMF-ACETONE (1:1)	4h at 700rpm 50°C	Rotating collector (diam=0.8mm)	30-60	25	8 min	15	180	6	-	[122]
PVDF powders (Mv=625000)	NPT-ACETONE (EXP1=9/1 EXP2=9/1 EXP3=5/5 v/v)	Few hours at 50°C	Vertical electro-spinning setup	-	EXP1=60°C EXP2=Ambient EXP3=Ambient	-	7.5	100	EXP1=0.06 EXP2=2 EXP3=0.06	-	[123]
PVDF (Mv=275000); 22 wt%	NPT-ACETONE (9/1-7/3 v/v)	24h at 50°C 200rpm	Vertical electro-spinning setup	44	Ambient	-	From 10 to 13	From 100 to 250	0.5	-	[124]

Table C.2: Electrospinning parameters used for PVDF deposition in literature.

Material	Solvents	Stirring	Collector Type	RH [%]	T of dep. [°C]	Time of electro-spinning	Voltage [KV]	Dist. [mm]	Flow Rate [ml/h]	Rot. Speed [rpm]	Ref.
PVDF powder (Mv=534000); 20 wt%	DMF(6ml)- ACETONE (4ml)	3h on a hot plate	Rotating drum collector	-	-	-	15	150	2	1500	[125]
PVDF powders (Mv=534g/mol)	ACETONE- DMAC	1h on hot plate	Rectangular aluminium collector	-	Ambient	-	>10	200	0.08	-	[126]

Table C.3: Electrospinning parameters used for PVDF deposition in literature.

Bibliography

- [1] Weng, W., Chen, P., He, S., Sun, X., & Peng, H. (2016). Smart electronic textiles. *Angewandte Chemie International Edition*, 55(21), 6140-6169.
- [2] Zanobini A., slides of the course of "Misure elettronica", University of Florence, electronic and telecommunication department, October 2002.
- [3] <https://digilander.libero.it/materiali.scuola/MATERIALI/sensori.pdf>
- [4] Kanoun, O., Bouhamed, A., Ramalingame, R., Bautista-Quijano, J. R., Rajendran, D., & Al-Hamry, A. (2021). Review on conductive polymer/CNTs nanocomposites based flexible and stretchable strain and pressure sensors. *Sensors*, 21(2), 341.
- [5] Khalid, M. A. U., & Chang, S. H. (2022). Flexible strain sensors for wearable applications fabricated using novel functional nanocomposites: A review. *Composite Structures*, 115214.
- [6] Amjadi, M., Kyung, K. U., Park, I., & Sitti, M. (2016). Stretchable, skin-mountable, and wearable strain sensors and their potential applications: a review. *Advanced Functional Materials*, 26(11), 1678-1698.
- [7] Zang, Y., Zhang, F., Di, C. A., & Zhu, D. (2015). Advances of flexible pressure sensors toward artificial intelligence and health care applications. *Materials Horizons*, 2(2), 140-156.
- [8] textitNanomaterials, 10(11), Verpoorten, E., Massaglia, G., Ciardelli, G., Pirri, C. F., & Quaglio, M., Design and optimization of piezoresistive PEO/PEDOT: PSS electrospun nanofibers for wearable flex sensors, 2166 (2020)
- [9] Wen, N., Zhang, L., Jiang, D., Wu, Z., Li, B., Sun, C., & Guo, Z. (2020). Emerging flexible sensors based on nanomaterials: Recent status and applications. *Journal of Materials Chemistry A*, 8(48), 25499-25527.
- [10] Wang, Y., Yokota, T., & Someya, T. (2021). Electrospun nanofiber-based soft electronics. *NPG Asia Materials*, 13(1), 1-22.
- [11] Smith, P., Lemstra, P. J., Kalb, B., & Pennings, A. J. (1979). Ultrahigh-strength polyethylene filaments by solution spinning and hot drawing. *Polym. Bull*, 1(11), 733.
- [12] Feng, L., Li, S., Li, H., Zhai, J., Song, Y., Jiang, L., & Zhu, D. (2002). Superhydrophobic surface of aligned polyacrylonitrile nanofibers. *Angewandte Chemie International Edition*, 41(7), 1221-1223.
- [13] Zhang, Y., Lim, C. T., Ramakrishna, S., & Huang, Z. M. (2005). Recent development of polymer nanofibers for biomedical and biotechnological applications. *Journal of materials science: materials in medicine*, 16(10), 933-946.
- [14] Park, J. H., Kim, B. S., Yoo, Y. C., Khil, M. S., & Kim, H. Y. (2008). Enhanced

- mechanical properties of multilayer nano-coated electrospun nylon 6 fibers via a layer-by-layer self-assembly. *Journal of applied polymer science*, 107(4), 2211-2216.
- [15] Xue, J., Xie, J., Liu, W., & Xia, Y. (2017). Electrospun nanofibers: new concepts, materials, and applications. *Accounts of chemical research*, 50(8), 1976-1987.
- [16] Nagam Hanumantharao, S., & Rao, S. (2019). Multi-functional electrospun nanofibers from polymer blends for scaffold tissue engineering. *Fibers*, 7(7), 66.
- [17] Yang, Y., Zhang, Z., Wan, M., Wang, Z., Zou, X., Zhao, Y., & Sun, L. (2020). A Facile Method for the Fabrication of Silver Nanoparticles Surface Decorated Polyvinyl Alcohol Electrospun Nanofibers and Controllable Antibacterial Activities. *Polymers*, 12(11), 2486.
- [18] Fong, H., Chun, I., & Reneker, D. H. (1999). Beaded nanofibers formed during electrospinning. *Polymer*, 40(16), 4585-4592.
- [19] Wang, M., Fang, D., Wang, N., Jiang, S., Nie, J., Yu, Q., & Ma, G. (2014). Preparation of PVDF/PVP core-shell nanofibers mats via homogeneous electrospinning. *Polymer*, 55(9), 2188-2196.
- [20] Li, L., Peng, S., Lee, J. K. Y., Ji, D., Srinivasan, M., & Ramakrishna, S. (2017). Electrospun hollow nanofibers for advanced secondary batteries. *Nano Energy*, 39, 111-139.
- [21] Massaglia, G., & Quaglio, M. (2018). Semiconducting nanofibers in photoelectrochemistry. *Materials Science in Semiconductor Processing*, 73, 13-21.
- [22] Ding, J., Zhang, J., Li, J., Li, D., Xiao, C., Xiao, H., ... & Chen, X. (2019). Electrospun polymer biomaterials. *Progress in Polymer Science*, 90, 1-34.
- [23] Homayounfar, S. Z., & Andrew, T. L. (2020). Wearable sensors for monitoring human motion: a review on mechanisms, materials, and challenges. *SLAS TECHNOLOGY: Translating Life Sciences Innovation*, 25(1), 9-24.
- [24] Zhang, H., Zhang, J., Hu, Z., Quan, L., Shi, L., Chen, J., ... & Luo, J. (2019). Waist-wearable wireless respiration sensor based on triboelectric effect. *Nano Energy*, 59, 75-83.
- [25] Lin, Z., Chen, J., Li, X., Zhou, Z., Meng, K., Wei, W., ... & Wang, Z. L. (2017). Triboelectric nanogenerator enabled body sensor network for self-powered human heart-rate monitoring. *ACS nano*, 8830-8837.
- [26] Niu, S., Zhou, Y. S., Wang, S., Liu, Y., Lin, L., Bando, Y., & Wang, Z. L. (2014). Simulation method for optimizing the performance of an integrated triboelectric nanogenerator energy harvesting system. *Nano Energy*, 8, 150-156.
- [27] Qin, J., Yin, L. J., Hao, Y. N., Zhong, S. L., Zhang, D. L., Bi, K., ... & Dang, Z. M. (2021). Flexible and stretchable capacitive sensors with different microstructures. *Advanced Materials*, 33(34), 2008267.
- [28] Dobrzynska, J. A., & Gijs, M. A. (2012). Flexible polyimide-based force sensor. *Sensors and Actuators A: Physical*, 173(1), 127-135
- [29] Ntagios, M., Nassar, H., Pullanchiyodan, A., Navaraj, W. T., & Dahiya, R. (2020). Robotic hands with intrinsic tactile sensing via 3D printed soft pressure sensors. *Advanced Intelligent Systems*, 2(6), 1900080.
- [30] Yang, X., Wang, Y., & Qing, X. (2019). A flexible capacitive sensor based on the electrospun PVDF nanofiber membrane with carbon nanotubes. *Sensors and Actuators A: Physical*, 299, 111579.
- [31] Li, X., Zhang, R., Yu, W., Wang, K., Wei, J., Wu, D., ... & Zhu, H. (2012). Stretchable and highly sensitive graphene-on-polymer strain sensors. *Scientific reports*, 2(1), 1-6.

- [32] Shi, J., Wang, L., Dai, Z., Zhao, L., Du, M., Li, H., & Fang, Y. (2018). Multiscale hierarchical design of a flexible piezoresistive pressure sensor with high sensitivity and wide linearity range. *Small*, 14(27), 1800819.
- [33] Charara, M., Luo, W., Saha, M. C., & Liu, Y. (2019). Investigation of lightweight and flexible carbon nanofiber/poly dimethylsiloxane nanocomposite sponge for piezoresistive sensor application. *Advanced Engineering Materials*, 21(5), 1801068.
- [34] Toprakci, H. A., Kalanadhabhatla, S. K., Spontak, R. J., & Ghosh, T. K. (2013). Polymer nanocomposites containing carbon nanofibers as soft printable sensors exhibiting strain-reversible piezoresistivity. *Advanced Functional Materials*, 23(44), 5536-5542.
- [35] Jason, Naveen N., My D. Ho, and Wenlong Cheng. (2017). Resistive electronic skin. *Journal of Materials Chemistry C*, 5(24), 5845-5866.
- [36] Ueberschlag, P. (2001) PVDF piezoelectric polymer. *Sensor review*.
- [37] Sappati, K. K., & Bhadra, S. (2018). Piezoelectric polymer and paper substrates: A review. *Sensors*, 18(11), 3605.
- [38] Khan, H., Razmjou, A., Ebrahimi Warkiani, M., Kottapalli, A., & Asadnia, M. (2018). Sensitive and flexible polymeric strain sensor for accurate human motion monitoring. *Sensors*, 18(2), 418.
- [39] Lu, L., Zhao, N., Liu, J., & Yang, B. (2021). Coupling piezoelectric and piezoresistive effects in flexible pressure sensors for human motion detection from zero to high frequency. *Journal of Materials Chemistry C*, 9(29), 9309-9318.
- [40] Kim, K. K., Hong, S., Cho, H. M., Lee, J., Suh, Y. D., Ham, J., & Ko, S. H. (2015). Highly sensitive and stretchable multidimensional strain sensor with prestrained anisotropic metal nanowire percolation networks. *Nano letters*, 15(8), 5240-5247.
- [41] Kumar, C. S. (Ed.). (2007). *Nanomaterials for biosensors*. John Wiley & Sons.
- [42] Sankar, V., Balasubramaniam, K., & Sundara, R. (2021). Insights into the effect of polymer functionalization of multiwalled carbon nanotubes in the design of flexible strain sensor. *Sensors and Actuators A: Physical*, 322, 112605.
- [43] Gong, X. X., Fei, G. T., Fu, W. B., Fang, M., Gao, X. D., Zhong, B. N., & De Zhang, L. (2017). Flexible strain sensor with high performance based on PANI/PDMS films. *Organic Electronics*, 47, 51-56.
- [44] Jung, J., Lee, H., Ha, I., Cho, H., Kim, K. K., Kwon, J., ... & Ko, S. H. (2017). Highly stretchable and transparent electromagnetic interference shielding film based on silver nanowire percolation network for wearable electronics applications. *ACS applied materials & interfaces*, 9(51), 44609-44616.
- [45] AlAhzm, A. M., Alejli, M. O., Ponnamma, D., Elgawady, Y., & Al-Maadeed, M. A. A. (2021). Piezoelectric properties of zinc oxide/iron oxide filled polyvinylidene fluoride nanocomposite fibers. *Journal of Materials Science: Materials in Electronics*, 32(11), 14610-14622.
- [46] Massaglia, G., Chiodoni, A., Salvador, G. P., Delmondo, L., Munoz-Tabares, J. A., Bocchini, S., ... & Quaglio, M. (2017). Defining the role of nanonetting in the electrical behaviour of composite nanofiber/nets. *RSC advances*, 7(62), 38812-38818.
- [47] Xie, Xiao-Lin, Yiu-Wing Mai, & Xing-Ping Zhou. (2005). Dispersion and alignment of carbon nanotubes in polymer matrix: a review. *Materials science and engineering: R: Reports*, 49(4), 89-112.
- [48] Sandler, J., Shaffer, M. S. P., Prasse, T., Bauhofer, W., Schulte, K., & Windle, A. H. (1999). Development of a dispersion process for carbon nanotubes in an epoxy matrix

- and the resulting electrical properties. *Polymer*, 40(21), 5967-5971.
- [49] Tung, T. T., Yeon, J. H., Kim, T. Y., & Suh, K. S. (2010). Synthesis and characterization of the carbon nanotube-based composite materials with poly (3, 4-ethylenedioxythiophene) *Synthetic metals*, 160(11-12), 1266-1272.
- [50] Kalaitzidou, K., Fukushima, H., & Drzal, L. T. (2010). A route for polymer nanocomposites with engineered electrical conductivity and percolation threshold. *Materials*, 3(2), 1089-1103.
- [51] Clingerman, M. L., Weber, E. H., King, J. A., & Schulz, K. H. (2003). Development of an additive equation for predicting the electrical conductivity of carbon-filled composites. *Journal of applied polymer science*, 88(9), 2280-2299.
- [52] Modesti M., "Applicazione di CNT in nanocompositi polimerici: casi di studio.", University of Padova, Industrial engineering department, May 2013.
- [53] Krishnamoorti, R., & Chatterjee, T. (2015). Carbon nanotube-based poly (ethylene oxide) nanocomposites. In *Handbook of Polymer Nanocomposites. Processing, Performance and Application*, (pp. 299-334). Springer, Berlin, Heidelberg.
- [54] Mohanraj, G. T., Chaki, T. K., Chakraborty, A., & Khastgir, D. (2007). Measurement of AC conductivity and dielectric properties of flexible conductive styrene-butadiene rubber-carbon black composites. *Journal of applied polymer science*, 104(2), 986-995.
- [55] Vionnet-Menot, S., Grimaldi, C., Maeder, T., Strässler, S., & Ryser, P. *Physical Review B*, 71(6), 064201(2005). Tunneling-percolation origin of nonuniversality: Theory and experiments.
- [56] Gong, S., & Zhu, Z. H. (2014). On the mechanism of piezoresistivity of carbon nanotube polymer composites. *Polymer*, 55(16), 4136-4149.
- [57] *Nanoscale research letters*, 7(1), Hu, B., Hu, N., Li, Y., Akagi, K., Yuan, W., Watanabe, T., & Cai, Y. (2012). Multi-scale numerical simulations on piezoresistivity of CNT/polymer nanocomposites., 1-11, (2012).
- [58] Chung, D. D. L. (2020). A critical review of piezoresistivity and its application in electrical-resistance-based strain sensing. *Journal of Materials Science*, 55(32), 15367-15396.
- [59] Park, M., Kim, H., & Youngblood, J. P. (2008). Strain-dependent electrical resistance of multi-walled carbon nanotube/polymer composite films. *Nanotechnology*, 19(5), 055705.
- [60] Gao, J., Wang, H., Huang, X., Hu, M., Xue, H., & Li, R. K. (2018). Electrically conductive polymer nanofiber composite with an ultralow percolation threshold for chemical vapour sensing. *Composites Science and Technology*, 161, 135-142.
- [61] Qavamnia, S. S., & Nasouri, K. (2016). Facile fabrication of carbon nanotubes/polystyrene composite nanofibers for high-performance electromagnetic interference shielding. *Fibers and polymers*, 17(12), 1977-1984.
- [62] Katsnelson, M. I. (2007). Graphene: carbon in two dimensions. *Materials today*, 10(1-2), 20-27.
- [63] Popov, V. N. (2004). Carbon nanotubes: properties and application. *Materials Science and Engineering: R: Reports*, 43(3), 61-102.
- [64] <https://assignmentpoint.com/carbon-nanotubes/>
- [65] Chen, Y., Zhang, L., Zhang, Y., Gao, H., & Yan, H. (2018). Large-area perovskite solar cells—a review of recent progress and issues. *RSC advances*, 8(19), 10489-10508.

- [66] Laskar, M. A. R. (2017). Piezoelectricity: An energy source for future railway stations. *SEU journal of science and engineering*, 11(2).
- [67] Smith, M., & Kar-Narayan, S. (2022). Piezoelectric polymers: Theory, challenges and opportunities. *International Materials Reviews*, 67(1), 65-88.
- [68] Garino N., slides of the course “Materials and characterization for Micro and Nanotechnology”, Politecnico di Torino, electronic department, 2021.
- [69] Lionetto, F., Licciulli, A., Montagna, F., & Maffezzoli, A. Piezoceramici: guida introduttiva al loro utilizzo. *stress*, 1, 2.
- [70] Munawar, M. A., & Schubert, D. W. (2021). Highly Oriented Electrospun Conductive Nanofibers of Biodegradable Polymers-Revealing the Electrical Percolation Thresholds. *ACS Applied Polymer Materials*, 3(6), 2889-2901.
- [71] Yeo, L. Y., & Friend, J. R. (2006). Electrospinning carbon nanotube polymer composite nanofibers. *Journal of experimental nanoscience*, 1(2), 177-209.
- [72] Dror, Y., Salalha, W., Khalfin, R. L., Cohen, Y., Yarin, A. L., & Zussman, E. (2003). Carbon nanotubes embedded in oriented polymer nanofibers by electrospinning. *Langmuir*, 19(17), 7012-7020.
- [73] Azimi, B., Milazzo, M., Lazzeri, A., Berrettini, S., Uddin, M. J., Qin, Z., ... & Danti, S. (2020). Electrospinning piezoelectric fibers for biocompatible devices. *Advanced health-care materials*, 9(1), 1901287.
- [74] Kalimuldina, G., Turdakyn, N., Abay, I., Medeubayev, A., Nurpeissova, A., Adair, D., & Bakenov, Z. (2020). A review of piezoelectric PVDF film by electrospinning and its applications. *Sensors*, 20(18), 5214.
- [75] Sukumaran, S., Chatbouri, S., Rouxel, D., Tisserand, E., Thiebaud, F., & Ben Zineb, T. (2021). Recent advances in flexible PVDF based piezoelectric polymer devices for energy harvesting applications. *Journal of Intelligent Material Systems and Structures*, 32(7), 746-780.
- [76] *Progress in polymer science*, 39(4), Martins, P., Lopes, A. C., & Lanceros-Mendez, S. Electroactive phases of poly (vinylidene fluoride): Determination, processing and applications, 683-706, (2014).
- [77] Martins, P., Lopes, A. C., & Lanceros-Mendez, S. (2014). Electroactive phases of poly (vinylidene fluoride): Determination, processing and applications. *Progress in polymer science*, 39(4), 683-706.
- [78] Tanaka, Y., Nguyen, D. P., Fukuda, T., & Sano, A. (2015, June). Wearable skin vibration sensor using a PVDF film. In 2015 *World Haptics Conference (WHC)*, (pp. 146-151). IEEE.
- [79] He, Z., Rault, F., Lewandowski, M., Mohsenzadeh, E., & Salaün, F. (2021). Electrospun PVDF nanofibers for piezoelectric applications: A review of the influence of electrospinning parameters on the β phase and crystallinity enhancement. *Polymers*, 13(2), 174.
- [80] Haider, A., Haider, S., & Kang, I. K. (2018). A comprehensive review summarizing the effect of electrospinning parameters and potential applications of nanofibers in biomedical and biotechnology. *Arabian Journal of Chemistry*, 11(8), 1165-1188.
- [81] Ramakrishna, S., Fujihara, K., Teo, W. E., Yong, T., Ma, Z., & Ramaseshan, R. (2006). Electrospun nanofibers: solving global issues. *Materials today*, 9(3), 40-50.
- [82] Viter, R., Iatsunskyi, I., Fedorenko, V., Tumenas, S., Balevicius, Z., Ramanavicius, A., ... & Bechelany, M. (2016). Enhancement of electronic and optical properties

- of ZnO/Al₂O₃ nanolaminate coated electrospun nanofibers. *The Journal of Physical Chemistry C*, 120(9), 5124-5132.
- [83] Baji, A., Agarwal, K., & Oopath, S. V. (2020). Emerging developments in the use of electrospun fibers and membranes for protective clothing applications. *Polymers*, 12(2), 492.
- [84] Lannutti, J., Reneker, D., Ma, T., Tomasko, D., & Farson, D. (2007). Electrospinning for tissue engineering scaffolds. *Materials Science and Engineering: C*, 27(3), 504-509.
- [85] Tucker, N., Stanger, J. J., Staiger, M. P., Razzaq, H., & Hofman, K. (2012). The history of the science and technology of electrospinning from 1600 to 1995. *Journal of engineered fibers and fabrics*, 7(2_{suppl}), 155892501200702S10.
- [86] Reneker, D. H., & Fong, H. (2006). Polymeric nanofibers: introduction.
- [87] *Biotechnology advances*, 28(3), Bhardwaj, N., & Kundu, S. C. Electrospinning: a fascinating fiber fabrication technique., 325-347, (2010)
- [88] Deitzel, J. M., Kleinmeyer, J., Harris, D. E. A., & Tan, N. B. (2001). The effect of processing variables on the morphology of electrospun nanofibers and textiles. *Polymer*, 42(1), 261-272.
- [89] Karakaş, H. (2015). Electrospinning of nanofibers and their applications. *Istanbul Technical University, Textile Technologies and Design Faculty*.
- [90] Hasan, M. M., Alam, A. M., & Nayem, K. A. (2014). Application of electrospinning techniques for the production of tissue engineering scaffolds: a review. *European Scientific Journal*, 10(15).
- [91] Bhushani, J. A., & Anandharamakrishnan, C. (2014). Electrospinning and electro-spraying techniques: Potential food based applications. *Trends in Food Science & Technology*, 38(1), 21-33.
- [92] Subbiah, T., Bhat, G. S., Tock, R. W., Parameswaran, S., & Ramkumar, S. S. (2005). Electrospinning of nanofibers. *Journal of applied polymer science*, 96(2), 557-569.
- [93] *Polymer*, 40(16), Fong, H., Chun, I., & Reneker, D. H. Beaded nanofibers formed during electrospinning., 4585-4592, (1999).
- [94] Koski, A., Yim, K., & Shivkumar, S. J. M. L. (2004). Effect of molecular weight on fibrous PVA produced by electrospinning. *Materials Letters*, 58(3-4), 493-497.
- [95] McKee, M. G., Layman, J. M., Cashion, M. P., & Long, T. E. (2006). Phospholipid nonwoven electrospun membranes. *Science*, 311(5759), 353-355.
- [96] Haghi, A. K., & Akbari, M. (2007). Trends in electrospinning of natural nanofibers. *physica status solidi (a)*, 204(6), 1830-1834.
- [97] Şener, A. G., Altay, A. S., & Altay, F. (2011, December). Effect of voltage on morphology of electrospun nanofibers. In *2011 7th International Conference on Electrical and Electronics Engineering (ELECO)* (pp. I-324). IEEE.
- [98] Zander, N. E. (2013). Hierarchically structured electrospun fibers. *Polymers*, 5(1), 19-44.
- [99] He, Z., Rault, F., Lewandowski, M., Mohsenzadeh, E., & Salaün, F. (2021). Electrospun PVDF nanofibers for piezoelectric applications: A review of the influence of electrospinning parameters on the β phase and crystallinity enhancement. *Polymers*, 13(2), 174.
- [100] Yuan, X., Zhang, Y., Dong, C., & Sheng, J. (2004). Morphology of ultrafine polysulfone fibers prepared by electrospinning. *Polymer international*, 53(11), 1704-1710.

- [101] Szewczyk, P. K., & Stachewicz, U. (2020). The impact of relative humidity on electrospun polymer fibers: From structural changes to fiber morphology. *Advances in Colloid and Interface Science*, 286, 102315.
- [102] Huang, F., Wei, Q., Wang, J., Cai, Y., & Huang, Y. (2008). Effect of temperature on structure, morphology and crystallinity of PVDF nanofibers via electrospinning. *e-Polymers*, 8(1).
- [103] *Polymer*, 46(18), Kim, G. M., Michler, G. H., & Pötschke, P. Deformation processes of ultrahigh porous multiwalled carbon nanotubes/polycarbonate composite fibers prepared by electrospinning., 7346-7351, (2005).
- [104] Effect of electrospinning parameters and polymer concentrations on mechanical-to-electrical energy conversion of randomly-oriented electrospun poly (vinylidene fluoride) nanofiber mats., Shao, H., Fang, J., Wang, H., & Lin, T. , 5(19), 14345-14350, (2015), *RSC advances*.
- [105] *Polymer*, 214, Singh, R. K., Lye, S. W., & Miao, J. Holistic investigation of the electrospinning parameters for high percentage of β -phase in PVDF nanofibers. 123366, (2021).
- [106] *Polymer*, 228, Gade, H., Nikam, S., Chase, G. G., & Reneker, D. H., Effect of electrospinning conditions on β -phase and surface charge potential of PVDF fibers. 123902, (2021).
- [107] He, Z., Rault, F., Lewandowski, M., Mohsenzadeh, E., & Salaün, F. (2021). Electrospun PVDF nanofibers for piezoelectric applications: A review of the influence of electrospinning parameters on the β phase and crystallinity enhancement. *Polymers*, 13(2), 174.
- [108] *Polymer*, 49(10), Reneker, D. H., & Yarin, A. L. Electrospinning jets and polymer nanofibers., 2387-2425, (2008).
- [109] <https://www.nanocyl.com/product/nc7000/>
- [110] Giorgis F., slides of the course “Materials and characterization for Micro and Nanotechnology”, Politecnico di Torino, electronic department, 2021.
- [111] *Progress in biophysics and molecular biology*, 59(1), Arrondo, J. L. R., Muga, A., Castresana, J., & Goñi, F. M., Quantitative studies of the structure of proteins in solution by Fourier-transform infrared spectroscopy., 23-56, 1993.
- [112] McCullen, S. D., Stevens, D. R., Roberts, W. A., Ojha, S. S., Clarke, L. I., & Gorga, R. E. (2007). Morphological, electrical, and mechanical characterization of electrospun nanofiber mats containing multiwalled carbon nanotubes. *Macromolecules*, 40(4), 997-1003.
- [113] Mohammadpour, R., & Rafizadeh, M. (2014). Preparation, morphology and conductivity of polyacrylonitrile/multi-wall carbon nanotubes composite nanofibers. *Iranian Polymer Journal*, 23(9), 731-743.
- [114] Aqeel, S. M., Huang, Z., Walton, J., Baker, C., Falkner, D. L., Liu, Z., & Wang, Z. (2018). Polyvinylidene fluoride (PVDF)/polyacrylonitrile (PAN)/carbon nanotube nanocomposites for energy storage and conversion. *Advanced composites and hybrid materials*, 1(1), 185-192.
- [115] Mir, S. M., Jafari, S. H., Khonakdar, H. A., Krause, B., Pötschke, P., & Qazvini, N. T. (2016). A promising approach to low electrical percolation threshold in PMMA nanocomposites by using MWCNT-PEO predispersions. *Materials & Design*, 111, 253-262.

- [116] Choi, S. W., Kim, J. R., Ahn, Y. R., Jo, S. M., & Cairns, E. J. (2007). Characterization of electrospun PVDF fiber-based polymer electrolytes. *Chemistry of materials*, 19(1), 104-115.
- [117] Gee, S., Johnson, B., & Smith, A. L. (2018). Optimizing electrospinning parameters for piezoelectric PVDF nanofiber membranes. *Journal of membrane science*, 563, 804-812.
- [118] Bae, J., Baek, I., & Choi, H. (2017). Efficacy of piezoelectric electrospun nanofiber membrane for water treatment. *Chemical Engineering Journal*, 307, 670-678.
- [119] Jiyong, H., Yinda, Z., Hele, Z., Yuanyuan, G., & Xudong, Y. (2017). Mixed effect of main electrospinning parameters on the β -phase crystallinity of electrospun PVDF nanofibers. *Smart Materials and Structures*, 26(8), 085019.
- [120] Lei, T., Zhu, P., Cai, X., Yang, L., & Yang, F. (2015). Electrospinning of PVDF nanofibrous membranes with controllable crystalline phases. *Applied Physics A*, 120(1), 5-10.
- [121] Saha, S., Yauvana, V., Chakraborty, S., & Sanyal, D. (2019). Synthesis and characterization of polyvinylidene-fluoride (PVDF) nanofiber for application as piezoelectric force sensor. *Materials Today: Proceedings*, 18, 1450-1458.
- [122] Szewczyk, P. K., Gradys, A., Kim, S. K., Persano, L., Marzec, M., Kryshstal, A., ... & Stachewicz, U. (2020). Enhanced piezoelectricity of electrospun polyvinylidene fluoride fibers for energy harvesting. *ACS applied materials & interfaces*, 12(11), 13575-13583.
- [123] Cai, X., Lei, T., Sun, D., & Lin, L. (2017). A critical analysis of the α , β and γ phases in poly (vinylidene fluoride) using FTIR. *RSC advances*, 7(25), 15382-15389.
- [124] Bae, J., Baek, I., & Choi, H. (2017). Efficacy of piezoelectric electrospun nanofiber membrane for water treatment. *Chemical Engineering Journal*, 307, 670-678.
- [125] Singh, R. K., Lye, S. W., & Miao, J. (2020). Measurement of impact characteristics in a string using electrospun PVDF nanofibers strain sensors. *Sensors and Actuators A: Physical*, 303, 111841.
- [126] Fabriani, F., Chytanya, K. C., Giovanna, I., & Lanzara, G. (2018). Characterization of electrospun PVDF fibres for sensing and actuation. *Multidisciplinary Digital Publishing Institute Proceedings*, 2(8), 501.
- [127] Ahn, Y., Lim, J. Y., Hong, S. M., Lee, J., Ha, J., Choi, H. J., & Seo, Y. (2013). Enhanced piezoelectric properties of electrospun poly (vinylidene fluoride)/multiwalled carbon nanotube composites due to high β -phase formation in poly (vinylidene fluoride). *The Journal of Physical Chemistry C*, 117(22), 11791-11799.
- [128] Cauda, V., Stassi, S., Bejtka, K., & Canavese, G. (2013). Nanoconfinement: an effective way to enhance PVDF piezoelectric properties. *ACS applied materials & interfaces*, 5(13), 6430-6437.
- [129] Bui, T. T., Shin, M. K., Jee, S. Y., Long, D. X., Hong, J., & Kim, M. G. (2022). Ferroelectric PVDF nanofiber membrane for high-efficiency PM0.3 air filtration with low air flow resistance. *Colloids and Surfaces A: Physicochemical and Engineering Aspects*, 640, 128418.
- [130] Fan, Q., Qin, Z., Gao, S., Wu, Y., Pionteck, J., Mäder, E., & Zhu, M. (2012). The use of a carbon nanotube layer on a polyurethane multifilament substrate for monitoring strains as large as 400%. *Carbon*, 50(11), 4085-4092.

- [131] Chen, L., Chen, G. H., & Lu, L. (2007). Piezoresistive behavior study on finger-sensing silicone rubber/graphite nanosheet nanocomposites. *Advanced Functional Materials*, 17(6), 898-904.
- [132] Bae, J., Baek, I., & Choi, H. (2017). Efficacy of piezoelectric electrospun nanofiber membrane for water treatment. *Chemical Engineering Journal*, 307, 670-678.
- [133] Zhang, W., Herrera, C., Atluri, S. N., & Kassab, G. S. (2005). The effect of longitudinal pre-stretch and radial constraint on the stress distribution in the vessel wall: a new hypothesis. *Molecular & Cellular Biomechanics*, 2(1), 41.
- [134] Burton, A. C. (1951). On the physical equilibrium of small blood vessels. *American Journal of Physiology-Legacy Content*, 164(2), 319-329.

Acknowledgements

I would like to dedicate few lines to those who contributed to the realization of my thesis. First of all, I would like to thank my supervisor Prof. Marzia Quaglio and my co-supervisor Dr. Giulia Massaglia for the knowledge transmitted, for the indispensable advice, for always being available and for the patience they had towards me throughout the thesis work.

Vorrei dedicare qualche riga a tutti coloro che hanno contribuito alla realizzazione della mia tesi di laurea.

Vorrei innanzitutto ringraziare la mia relatrice Prof.ssa Marzia Quaglio e la mia corretrice Dott.ssa Giulia Massaglia per le conoscenze trasmesse, per gli indispensabili consigli, per essere state sempre disponibili e per la pazienza avuta nei miei confronti durante tutto il lavoro di tesi.

Ringrazio immensamente i miei genitori che mi hanno sempre sostenuta credendo in me più di chiunque altro. Il loro appoggio, la loro comprensione, i loro consigli e i loro sacrifici mi hanno permesso di arrivare fin qui ed è per questo che dedico a loro questo lavoro.

Un grazie speciale va a Patrick, per tutto il tempo che mi ha dedicato, per tutte le volte che ha saputo ascoltarmi in silenzio, per essermi sempre stato accanto, sostenendomi e spronandomi a fare sempre del mio meglio. Ringrazio anche tutta la sua famiglia, in particolar modo Edda e Flavio.

Ringrazio mio fratello Nicola e Bianka per esserci sempre, nonostante la distanza, riuscendo a sdrammatizzare i momenti di sconforto più di chiunque altro.

Ringrazio nonna per avermi sempre incoraggiata e nonno, che ho sempre sentito vicino.

Ringrazio tutti gli amici, anche quelli che nonostante la distanza, hanno saputo offrirmi dei momenti di svago indispensabili.

Infine, ringrazio me stessa, i miei sacrifici e la mia tenacia nel raggiungere questo traguardo.